



The Nanotech France 2022 International Conference

**June 15 to 17 2022
Conference Proceedings**

DOI:

<https://doi.org/10.26799/cp-nanotech-france-2022>

Synthesis and Repetitive Application of Nanocrystalline ZnO Based Floating Photocatalyst for the Detoxification of Water from Bacteria and Viruses Mixtures

Martynas Lelis¹, Simona Tuckute¹, Emilija Demikyte^{1,2}, Deimante Vasiliauske^{1,2}, Marius Urbonavicius¹, Sarunas Varnagiris¹, Sandra Sakalauskaite²

¹ Lithuanian Energy Institute, Breslaujos st. 3, Kaunas, Lithuania, rastine@lei.lt
² Vytautas Magnus University, K. Donelaičio st. 58, Kaunas, Lithuania, dek@gmf.vdu.lt

Abstract

Usually, the most efficient photocatalyst materials are synthesized as fine nanocrystalline powders and this rises significant handling and repetitive application issues. More recently, researchers started to immobilize photocatalyst (nano)materials on relatively large low density supports creating floating photocatalyst particles. Such approach allows to effectively retrieve and re-apply the used photocatalyst material. In current study we used reactive magnetron sputtering technique and deposited unconventional orange colour nanocrystalline ZnO based photocatalyst on floating high-density polyethylene (HDPE) grains. The structure of the synthesized photocatalyst was characterized by XRD, SEM, and XPS techniques. The repetitive measurements of Rhodamine B (RhB) dye bleaching by the ZnO based photocatalyst film under visible light irradiation showed high stability over ten cycles. Visible light induced photocatalytic efficiency of the floating photocatalyst grains (FPG) was also estimated by the repetitive treatment of water samples containing *Salmonella typhimurium* (strain SL1344) and *Micrococcus luteus* bacteria, as well as water samples containing PRD1 and T4 bacteriophages. These tests indicated complex interaction between the bacteria, viruses, photocatalyst and its HDPE support. For example, they revealed that FPGs lose most of its photocatalytic efficiency in just 3 cycles. To stabilize the ZnO based FPGs and enhance its photocatalytic efficiency under the visible light irradiation, before the depositing of ZnO films we pre-covered HDPE grains by Ni underlayer. The addition of Ni resulted in mixed results – Ni underlayer reduced the efficiency of *S. typhimurium* disinfection during the first cycle but increased the efficiency and detoxication stability over consecutive tests using the same set of FPGs.

Keywords: ZnO, floating photocatalysis, nanomaterials, magnetron sputtering, photocatalytic disinfection.

1. Introduction

Photocatalytic water treatment by UV or visible light irradiated TiO₂, ZnO, and some other semiconductor materials is recognized as a highly promising universal and environmentally friendly detoxification method [1]. It utilises semiconductor capability to absorb light and to use it for the generation of excited electrons (e^-) and holes (h^+) in conduction and valence bands respectively. In contact with H₂O and dissolved O₂, e^- and h^+ can produce reactive oxygen species (ROS), namely hydroxyl radicals (OH \cdot) and superoxide ions (O₂ $^{\cdot-}$). ROS have high oxidation potential and can easily mineralise various organic pollutants to harmless compounds like CO₂ and H₂O.

Photocatalytic ROS generation is heterogeneous process; therefore, enlargement of specific surface area of catalyst material is a straightforward way to improve its efficiency. Naturally, the most efficient photocatalysts are synthesized as fine nanocrystalline powders, but this material form rises significant issues of practical usability. For example, nanopowders can be inconvenient for handling and are hard to regain for repetitive applications. More recently, researchers started to immobilize photocatalyst (nano)materials on relatively large low density supports creating floating photocatalyst particles or grains [2]. Such approach allows to effectively retrieve the used photocatalyst material and to re-apply it for the treatment of new portion of contaminated water.

Up to now, TiO₂ based floating photocatalysts were synthesized and tested by relatively large number of researchers [3]–[8]. Some of these studies involved the repetitive tests which provided promising

results [3], [4], [6], [9]. For instance, Nair et al. demonstrated that TiO₂ nanosheet based nanocomposite floating photocatalyst can be repetitively used for dye degradation [3]. Whereas, Wu et al. demonstrated relatively high robustness of self-floating biomass charcoal supported flower-like plasmon silver/carbon, nitrogen co-doped defective TiO₂ [4]. On the other hand, the availability of reports on not TiO₂ based floating photocatalyst materials (for example ZnO) is much more limited. On top of that, there are virtually no reports of non TiO₂ based floating photocatalyst usage for the treatment of bacteria or viruses mixtures. However, such studies are important because live organisms are capable to react and adopt to the adverse environments.

Accordingly, in current study we used reactive magnetron sputtering technique and deposited unconventional orange colour nanocrystalline ZnO based photocatalyst on floating high-density polyethylene (HDPE) grains and estimated its suitability for the photocatalytic treatment of polluted water. Special attention was attributed to the analysis of floating photocatalyst stability during repetitive treatments of dyes and bacteria.

2. Methodology

In current study floating photocatalyst samples were obtained by ZnO film deposition on HDPE grains using reactive magnetron sputtering method. Nominal size of HDPE grains (obtained from GoodFellow) was 2-4 mm, density 0.95 g/cm³. The sputtering was conducted for 1 hour in Ar-O₂ gas atmosphere. Magnetron was equipped with Zn target (76 mm diameter, 99.99 % purity) and 150 W RF power source. Distance between sample and magnetron was 70 mm, deposition time - 60 min, approximate ZnO film thickness – 5 μm. Sputtering conditions were specifically optimised to obtain the non-typical orange colour ZnO films which were reported at [10]. The films were characterised by XRD (Bruker D8), SEM (Hitachi S-3400N) and XPS (PHI Versaprobe 5000).

Photocatalytic efficiency of the floating photocatalyst grains (FPG) was estimated by two methods. First, activity and stability of FPGs was tested by repetitive photocatalytic bleaching of Rhodamine B (RhB) solution (10 ml, 10 mg/L, 900 rpm magnetic string) under visible light irradiation (Thorlabs Solis 3C light source, 5700 K, 230 mW/cm²). Second, FPGs were used for the photocatalytic disinfection of water samples containing *Salmonella typhimurium* (strain SL1344) and *Micrococcus luteus* bacteria, as well as water samples containing PRD1 and T4 bacteriophages (viruses that infects bacteria). Detailed description of water treatment procedure as well as the detailed protocol for the growth of bacteria and bacteriophages is provided at [11].

3. Results and Discussion

After sputtering process optimisation, HDPE grains were covered up by continuous orange colour films (right insert of Fig. 1a). XRD analysis of the films revealed that films had only one crystal phase (Fig. 1a) indexed as hexagonal wurtzite ZnO. Similarly, to the results reported at [12], as-deposited films had strongly expressed (002) orientation, but additional peaks from the other crystal planes of ZnO were observed as well.

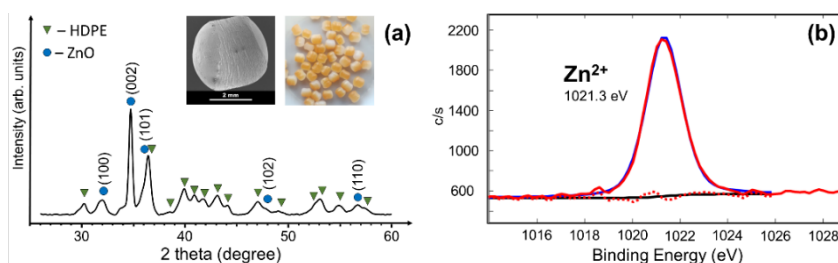


Fig. 1: XRD pattern (a) and Zn 2p_{3/2} core level electron spectra (b) of HDPE grains covered by ZnO films. Inserts of figure (a) shows SEM (left) and natural colour (right) images of the FPGs.

Elemental analysis by XPS showed slightly over-stoichiometric Zn:O ratio of 58:42. Small oxygen deficiency is typical for the magnetron sputtered oxides [13], besides minor oxygen deficit was introduced intentionally to obtain orange colour ZnO [10]. Considering Zn:O ratio, we expected that some zinc will have lower oxidation state. However, Zn 2p core level electron spectra indicated only

one chemical state of zinc which was attributed to Zn^{2+} (Fig. 1b). Considering all the circumstances, we assume that the lack of lower oxidative states on zinc is only the surface phenomena and is related to the interaction between the film and the atmosphere (i.e. adsorption of moisture, hydrocarbons and other adventitious contamination).

Data of the repetitive visible light assisted photocatalytic bleaching of RhB solution using ZnO based FPGs is present at Fig. 2. During the first use ZnO FPGs were capable to decrease RhB concentration by more than 99 % in 3 hours. During the consecutive photocatalytic treatment cycles the efficiency of ZnO FPGs remained relatively stable and after tenth cycle FPGs were still capable to reduce RhB concentration by approximately 96 %. It can be noticed, that after ten consecutive cycles there were practically no signs of photocatalyst film delamination from the HDPE grains and there were only some minor signs of film scuffing at the edges of the grains.

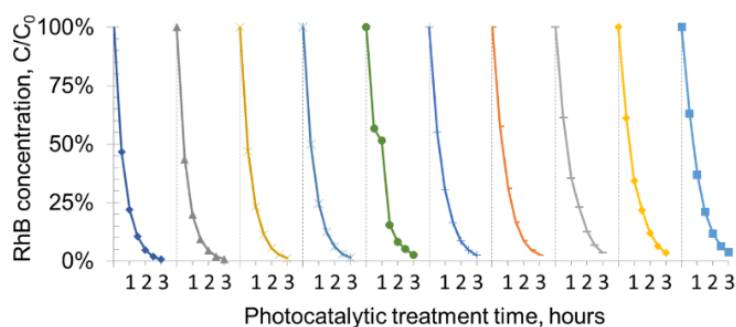


Fig. 2: Photocatalytic efficiency and stability of ZnO based FPGs over ten RhB bleaching cycles.

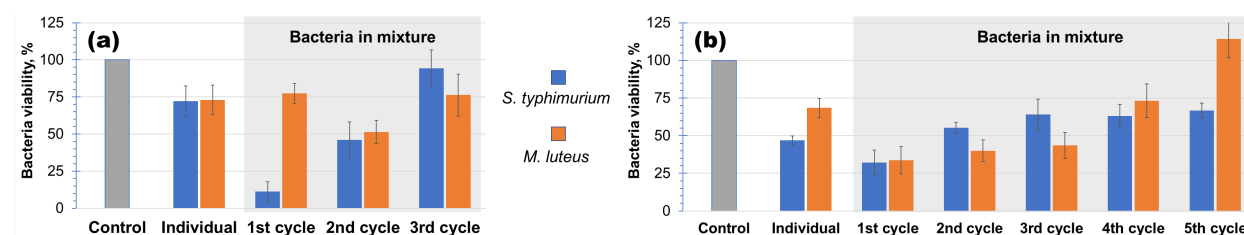


Fig. 3: Estimation of photocatalytic activity and cycle stability of ZnO FPGs: (a) without Ni, (b) with Ni.

Individual photocatalytic treatment of *S. typhimurium* and *M. luteus* bacteria suspension by 1 g of ZnO FPGs under visible light for 2.5 hours reduces bacteria viability by approximately 30 % (Fig. 3a) and indicates the actual photocatalytic disinfection capacity of ZnO FPGs. Then *S. typhimurium* and *M. luteus* bacteria cultures were mixed up together to form joint suspension and were treated repetitively under visible light with one set of ZnO FPGs (2 g). During cyclic disinfection tests bacteria viability reduction trends diverged significantly. Approximately 23 %, 49 % and 24 % of *M. Luteus* bacteria were inactivated during the first, second and third usage of the FPGs set. Meanwhile, inactivation efficiency of *S. typhimurium* bacteria was high during the first cycle (89 % viability reduction), but fell down strongly during second (54 % reduction) and third (6 % reduction) usage cycles.

Although the observed results were not trivial, they were reproducible (see error bars at Fig. 3a). Therefore, it is assumed that they reflect the non-linear outcome of the particularly complex interaction between bacteria, ROS, photocatalyst and FPGs substrate (i.e. HDPE) materials (non-linear results of photocatalytic bacteria treatment were also reported at [14]). First, it is clear that viability of individual bacteria should be affected by their competition for the same limited resources. Second, used bacteria are known to generate dissimilar response to the ROS [14]. Third, the system has a lot of components (two bacteria cultures, photocatalyst film, HDPE grains and multicomponent test medium), thus potentially there might be a lot of variations in isoelectric points especially when some parts of ZnO are scuffed off and HDPE surface is partially revealed. Other factors also might affect the efficiency of ROS generation and can change how ROS affect individual bacteria. In order to check the potential impact of HDPE substrate, prior to ZnO deposition we pre-covered HDPE grains by Ni. The addition of Ni resulted in mixed results (Fig. 3b), but in general it can be summarised that Ni underlayer slightly

increased the efficiency of FPGs and delayed its deteriorating. Assumingly, the improvement in efficiency was related to the better charge separation, meanwhile delayed deterioration of FPGs could be related to the decreased ROS access to the HDPE. Using FPGs for the photocatalytic inactivation of PRD1 and T4 bacteriophages revealed that ZnO FPGs were more effective on inactivation of PRD1 than T4 – infectivity reduction of phages in the mixture reached 20 % and 47 % respectively. The addition of Ni underlayer was not beneficial and inactivation of PRD1 and T4 phages reached only 2 % and 48 % respectively.

4. Conclusion

Floating photocatalyst samples were formed by ZnO film deposition on high density polyethylene grains. Tested samples had relatively high photocatalytic activity under visible light and were capable to maintain it over ten consecutive Rhodamine B solution bleaching cycles. On the other hand, during photocatalytic inactivation of bacteria photocatalyst lost most of its activity in just a few cycles. It was demonstrated, that in case of bacteria treatment, efficiency and stability of photocatalyst can improved by pre-covering polymer grains with Ni. However, for bacteriophages Ni underlayer was not beneficial. Altogether, conducted experiments indicated particularly complex interaction between bacteria/viruses, reactive oxygen species, photocatalyst and its polymeric grain substrate. Considering, that photocatalytic disinfection of biological contaminants is much more complex than mineralisation of some model molecules, we conclude that for the satisfactory practical results the selection of floating photocatalyst material and its substrate has to be optimised with specific biological contaminants in mind.

Acknowledgements

This research is funded by the European Social Fund according to the activity ‘Improvement of researchers’ qualification by implementing world-class R&D projects’ of Measure No. 09.3.3-LMT-K-712, project „Investigation of the application of TiO₂ and ZnO for the visible light assisted photocatalytical disinfection of the biologically contaminated water“(09.3.3-LMT-K-712-01-0175). Authors are thankful for R. Daugelavicius, N. Kuliesiene, R. Uscila and M. Aikas for their valuable input in the conducted study.

References

1. J. J. Rueda-Marquez et al., “A critical review on application of photocatalysis for toxicity reduction of real wastewaters,” *J. Clean. Prod.*, vol. 258, 2020.
2. A. Y. Shan et al., “Immobilisation of titanium dioxide onto supporting materials in heterogeneous photocatalysis: A review,” *Appl. Catal. A Gen.*, vol. 389, no. 1, pp. 1–8, 2010.
3. A. K. Nair et al., “Solar dye degradation using TiO₂ nanosheet based nanocomposite floating photocatalyst,” *Mater. Today Proc.*, vol. 46, pp. 2747–2751, 2021.
4. C. Wu et al., “Self-floating biomass charcoal supported flower-like plasmon silver/carbon, nitrogen co-doped defective TiO₂ as robust visible light photocatalysts,” *J. Clean. Prod.*, vol. 329, p. 129723, 2021.
5. Y. Shavisi et al., “Application of TiO₂/perlite photocatalysis for degradation of ammonia in wastewater,” *J. Ind. Eng. Chem.*, vol. 20, no. 1, pp. 278–283, 2014
6. M. Sboui et al., “TiO₂–PANI/Cork composite: A new floating photocatalyst for the treatment of organic pollutants under sunlight irradiation,” *J. Environ. Sci. (China)*, vol. 60, pp. 3–13, 2017.
7. M. J. Martín de Vidales et al., “3D printed floating photocatalysts for wastewater treatment,” *Catal. Today*, vol. 328, no. July 2018, pp. 157–163, 2019.
8. J. Zhang et al., “Floating photocatalysts based on loading Bi/N-doped TiO₂ on expanded graphite C/C (EGC) composites for the visible light degradation of diesel,” *RSC Adv.*, vol. 5, no. 88, pp. 71922–71931, 2015.
9. J. Wang et al., “A study on the preparation of floating photocatalyst supported by hollow TiO₂ and its performance,” *Appl. Surf. Sci.*, vol. 327, pp. 406–412, 2015.

10. K. Bockute et al., “Photoluminescence and structural defects of ZnO films deposited by reactive magnetron sputtering with unconventional Ar-O₂ gas mixture formation” in *Proceedings of the SurfCoat Korea2021*, 2–8.
11. M. Urbonavicius et al., “Visible-Light-Driven Photocatalytic Inactivation of Bacteria, Bacteriophages, and Their Mixtures Using ZnO-Coated HDPE Beads as Floating Photocatalyst,” *Materials*, vol. 15, no. 4. 2022.
12. S. Kunj and K. Sreenivas, “Residual stress and defect content in magnetron sputtered ZnO films grown on unheated glass substrates,” *Curr. Appl. Phys.*, vol. 16, no. 7, pp. 748–756, 2016.
13. M. Lelis et al., “Synthesis and analysis of metallic Zn phase rich ZnO oxide films for the photocatalytic water treatment technologies,” *Mater. Today Proc.*, vol. 33, no. 6, pp. 2484–2489, 2020.
14. S. Sakalauskaitė et al. “Influence of the Metabolic Activity of Microorganisms on Disinfection Efficiency of the Visible Light and P25 TiO₂ Photocatalyst.” *Catalysts*, 2021.

CuInS/ZnS Core-Shell Quantum Dots A Green Alternative to Cd and Pb Core Shell Quantum Dots

Kevin James Knebel, José Raúl Montes-Bojórquez, Arturo A. Ayón

University of Texas San Antonio, 1 UTSA Circle, San Antonio, TX 78249 USA, kevin.knebel@utsa.edu

Abstract

Herein, we explore the optoelectronic properties of CuInS/ZnS QDs synthesized at low temperature with polar ligands. We observed emission tunability of the core-shell quantum dots by varying the composition ratios in our syntheses. We have observed that there is an optimal compositional ratio that maximizes the photoluminescent quantum yield. The photoluminescence was enhanced by the addition of a ZnS shell. The optical bandgap of the core was studied by applying Jarosinski's and Pawlak's Inverse logarithmic derivative method (ILD) to the absorption spectrum, the results were compared to Tauc's method.

Keywords: Polar Quantum Dots, Core-Shell, ILD Method, Cd Pb Free Quantum Dots

1. Introduction

The tunability of optical and electrical properties of core-shell quantum dots (QDs) is highly desirable in photovoltaic devices, these nanostructures have been simulated and demonstrated in recent years to have excellent optoelectronic properties. Depending on material composition, the radius of the core and thickness of the shell, the charge carrier behavior can change from type I QD (i.e., electrons and holes are confined in the core), type II QD (i.e., electrons and holes are separated into core and shell regions), to quasi-type II QD (i.e., one type of charge carrier is localized in the core or shell while the other type of charge carrier is delocalized). In addition to charge carrier behavior, the optical emission can be tuned by controlling the radii of the core and shell. Currently, most of the studies reported have been limited to Cd and Pb based QDs [1,2,3,4]. However, these elements are known to be carcinogenic, limiting their applicability. Alternatively, Cu and In based QDs have been reported to be biocompatible [5]. This can establish greener practices in photovoltaic devices as well as open the applicability of core-shell QDs beyond photovoltaic systems to potential biomedical applications.

2. Experimental Conditions

2.1. Chemicals

Indium (III) chloride tetrahydrate ($\text{InCl}_3 \cdot 4\text{H}_2\text{O}$), copper (II) chloride ($\text{CuCl}_2 \cdot \text{H}_2\text{O}$), 3-mercaptopropionic acid (MPA), zinc acetate ($\text{Zn}(\text{OAc})_2$), sodium hydroxide (NaOH), sodium sulfide hydrate (Na_2S). Purchased from Sigma Aldridge

2.2. Synthesis

Two precursor solutions were prepared. One with 0.012mmol of CuCl_2 added to 20mL of deionized (DI) water. Then 4.59 mmol of MPA added to the solution promoting a chelating reaction. The pH of the precursor was then raised to pH 9. The In content of the second precursor was varied over a set of experiments to study the effects of Cu to In composition on photoluminescence. (0.050, 0.062, 0.074, 0.087, 0.099) mmol of InCl_3 added to 20 mL of DI water then 9.18 mmol of MPA was added to the precursor. The two solutions were added to one pot simultaneously and stirred for 3 minutes. 1mL of 0.8M Na_2S was added to the pot dropwise the pot was then heated to 90 °C for 30 minutes using a recirculatory oil bath. For the addition of a Zn Shell 2mL of 0.1M $\text{Zn}(\text{OAc})_2$ was added dropwise and left to react at 90 °C for 5 minutes. The pot was removed from the oil bath and allowed to cool to room temperature. Fig. 1 displays the synthesis process.

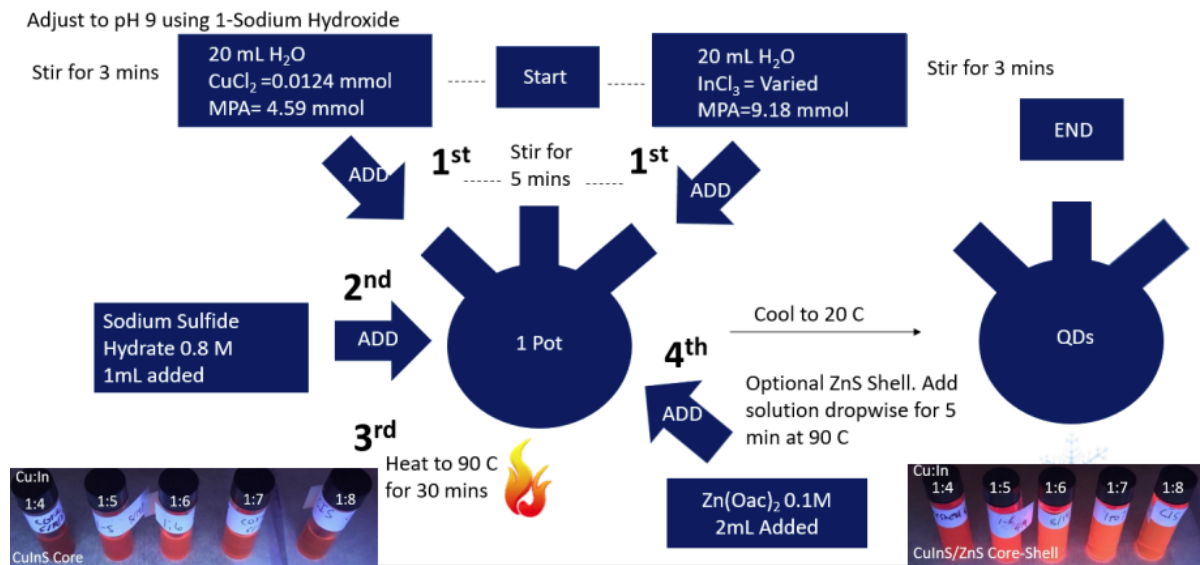


Fig. 1: Outlines the Synthesis of CuInS/ZnS Quantum dots. The photo on the lower left is without the ZnS shell and shows the photoluminescence synthesized at different Cu to In ratios. The Photo on the lower right is the quantum dots with the ZnS shell and also shows the Cu to In ratios.

3. Results and Discussion

The Emission spectrum was taken for each of the samples and can be seen in Fig.2. Since the 1:6 Cu to In ratio had the best emission properties the 1:6 sample for the core and core-shell were chosen for the Tauc's and Jarosinski's spectra analysis. The Jarosinski's method was used to model the transition behavior, and calculate the bandgap of the quantum dots. (The slope of Jarosinski plots gives information of the band transition. The intercept is the estimated band gap). The result was then compared to Tauc's method with the relevant transition behavior. Below is the derivation of the equation used in Jarosinski method from the famous equation used in Tauc's method. The results from the plots can be seen in Table 1 and Fig. 3

$$\alpha hv = a(hv - E_g)^m \quad (1)$$

$$\ln(\alpha hv) = m \ln a + m \ln(hv - E_g) \quad (2)$$

$$\frac{\partial \ln(\alpha hv)}{\partial \ln(hv)} = m \frac{1}{(hv - E_g)} \quad (3)$$

$$\frac{\Delta \ln(hv)}{\Delta(\alpha hv)} \approx \frac{1}{m} (hv - E_g) \quad (4)$$

Table 1: . Comparing results obtain in the Tauc's method to Jarosinski's method..

Quantum Dots	Jarosinski's m	Tauc's m	Jarosinski's Bandgap eV	Tauc's Bandgap eV	Method % Difference
Core	.7	.5	3.67	3.93	6.8

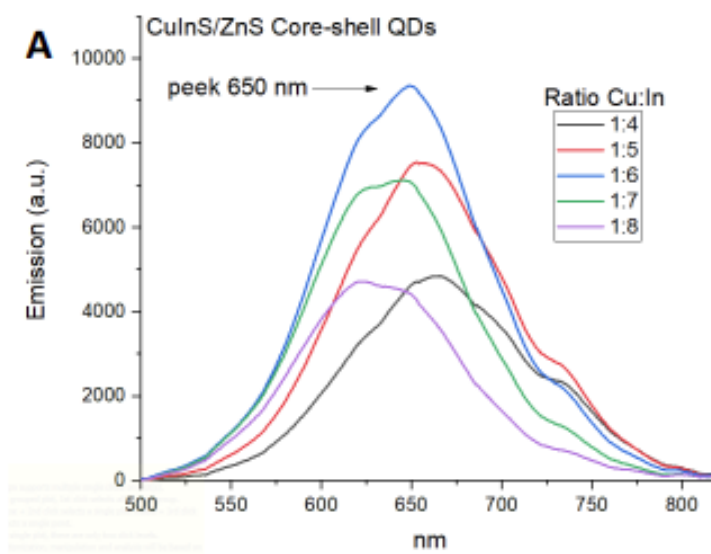


Fig. 3: A) Shows the emission of CuInS/ZnS QDs synthesized at different Cu:In ratios.

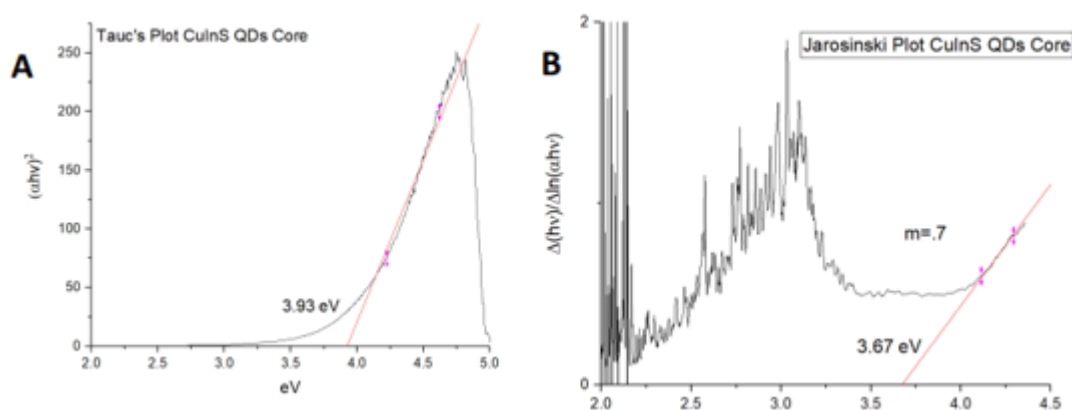


Fig. 3: A) Shows the Tauc's CuInS QDs core. B) Shows the Jarosinski's plots of CuInS QDs core.

4. Conclusion

The core composition study indicates a degree of optical tunability by controlling the Cu:In ratio. By increasing the amount of In we observed a relatively small blueshift in the emission spectra. Concurrently we observed that the optimum ratio for emission was a 1:6 Cu:In ratio. We anticipate that the ability to optimize the emission intensity of the core/shell nanoparticles discussed herein, will be successfully employed in the envisioned future work intended to improve the power conversion efficiency of photovoltaic structures.

Acknowledgements

We thank the UTSA Graduate School and the Department of Physics and Astronomy for the financial support provided for this project.

References

1. Nandan, Y., & Mehata, M. S. (2019). Wavefunction Engineering of Type-I/Type-II Excitons of CdSe/CdS Core-Shell Quantum Dots. *Scientific Reports*, 9(1), 2.
2. Zaiats, G., Yanover, D., Vaxenburg, R., Tilchin, J., Sashchiuk, A., & Lifshitz, E. (2014). PbSe-Based Colloidal Core/Shell Heterostructures for Optoelectronic Applications. *Materials*, 7(11), 7243.
3. Zhao, H., Fan, Z., Liang, H., Selopal, G. S., Gonfa, B. A., Jin, L., Soudi, A., Cui, D., Enrichi, F., Natile, M. M., Concina, I., Ma, D., Govorov, A. O., Rosei, F., & Vomiero, A. (2014). Controlling

photoinduced electron transfer from PbS@CdS core@shell quantum dots to metal oxide nanostructured thin films. *Nanoscale*, 6(12), 7004–7011.

4. Zhou, S., Dong, L., Popov, S., & Friberg, A. (2013). Radiative properties of carriers in CdSe-CdS core-shell heterostructured nanocrystals of various geometries. *Journal of the European Optical Society - Rapid Publications*, 8(0), 13042.
5. Liu, W., Zhang, Y., Zhao, J., Feng, Y., Wang, D., Zhang, T., Gao, W., Chu, H., Yin, J., Wang, Y., Zhao, J., & Yu, W. W. (2015). Photoluminescence of indium-rich copper indium sulfide quantum dots. *Journal of Luminescence*, 162, 191–196.
6. Ali, M., el Nady, J., Ebrahim, S., & Soliman, M. (2018). Structural and optical properties of upconversion CuInS/ZnS quantum dots. *Optical Materials*, 86, 545–549.

Au nanoparticles coated Au/Ag mirror as SERS active substrate for trace chemical detection

Vimarsh Awasthi, Vijayant Bhardwaj, Richa Goel, Satish Kumar Dubey

Centre for Sensors, Instrumentation and Cyber Physical System Engineering (SeNSE), Indian Institute of Technology Delhi, New Delhi-110016, India

Abstract

In this work, we have presented a design of sensitive and easy to fabricate SERS substrate constituting of chemically synthesized gold nanoparticles (Au NP) of varying sizes (~10-40nm); drop-casted on SiO₂ (coverslip, thickness~170 um) whose bottom surface is coated (using thermal evaporation) with a uniform, thin layer of Ag/Au (thickness~50nm). Size of nanoparticles have been investigated using transmission electron microscopy (TEM). Lumerical FDTD software have been used to analyse electric field profile over the proposed substrate. SERS measurements have been done to explore the detection capabilities of the substrate using rhodamine 6G (R6G) as a probe molecule. Au NP in combination with Au mirror (AuM) gave best results at 785 nm excitation. Proposed substrate detected up to 10⁻⁶M concentration of R6G using benchtop setup at our lab.

Keywords: Surface-enhanced Raman scattering (SERS), Au nanoparticles, Surface Plasmon Polariton (SPP), Spectroscopy, Chemical sensing, Energy harvesting, FDTD.

1. Introduction

Raman scattering/Raman effect is the inelastic scattering of photons from an atom or a molecule to provide unique molecular vibrational fingerprint of any molecule. Identification of an unknown analyte using SERS is determined on the basis of its Raman signature. SERS, a subset of Raman spectroscopy, is a powerful technique that uses the enhancement of the Raman signal of molecules situated in the vicinity of plasmonic nanostructures and offer information regarding the identity of the probe molecule [1]. It is a non-invasive, rapid and sensitive spectroscopic technique, with the capability down to single-molecule level detection [2]. SERS-based detection has evolved as one of the most promising approaches to detect analytes because of its high sensitivity, high specificity, high accuracy, and non-destructive testing capabilities [3]. The underlying mechanism of SERS is broadly classified into two effects- the electromagnetic effect and the chemical effect [4].

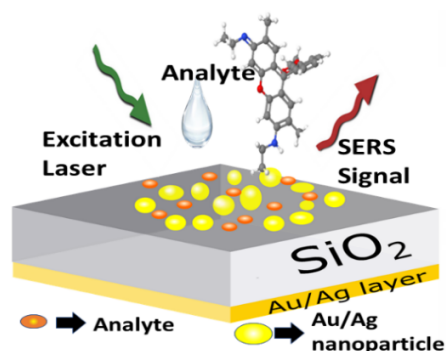


Fig. 1: Schematic of SERS substrate

In this study, Au Nanoparticles (NPs) are first chemically synthesized by the reduction of a water-soluble gold salt HAuCl₄ with a citrate ion (sodium salt of citric acid) [5]. Here, a citrate ion serves also as a reducing agent and anion stabilizer of particles. The as-prepared Au NPs (size=10-40nm) are then drop casted on a Au/Ag mirror (SiO₂ (coverslip, thickness~170 um) whose bottom surface is coated (using thermal evaporation) with a uniform, thin layer of Ag/Au (thickness~50nm)). The laser source with $\lambda=785\text{nm}$ is irradiated on the substrate on which the sample to be identified/analysed is drop-casted, here we have used rhodamine 6G (R6G) as probe molecule. The Au NPs gives rise to excitation of SPP, thereby ensuring electromagnetic enhancement. The thin Ag/Au layer at the bottom, produces a reflected

wave which upon interaction with NPs from below, produces further enhancement, thereby, increasing the overall light-matter interaction.

2. Experimental Section

2.1 Materials and Chemicals

Hydrogen tetrachloroaurate ($\text{HAuCl}_4 \cdot 3\text{H}_2\text{O}$), Sodium citrate ($\text{Na}_3\text{C}_6\text{H}_5\text{O}_7$), Sodium borohydride (NaBH_4), Deionised water (DI water), rhodamine 6G (R6G), Methanol, Ethanol, Acetone were procured from Sigma-Aldrich and were used as received. All the solutions were made with DI water.

2.2 Synthesis of gold nanoparticles

1.8 mL of 0.01M hydrogen tetrachloroaurate ($\text{HAuCl}_4 \cdot 3\text{H}_2\text{O}$) in DI water and 0.5 mL of 0.01M sodium citrate ($\text{Na}_3\text{C}_6\text{H}_5\text{O}_7$) in DI water were added to 40 mL of DI water. This solution was stirred. While stirring, 0.12 mL of freshly prepared 0.1M sodium borohydride (NaBH_4) was added. The solution colour changed from colourless to orange. After this, stirring was stopped and the solution was left undisturbed for few hours.

2.3 Transmission electron microscopy

The size of the gold nanoparticles was estimated using TEM (JEOL JEM-1400). For TEM measurements, carbon coated copper grid was washed with DI water. After drying, synthesised gold nanoparticles were drop casted over it and left to dry. Since the resolution of TEM is high, it is not necessary to purify gold nanoparticles through centrifugation.

2.4 Finite-difference time-domain simulations

Lumerical FDTD solution [6] software was used to analyse the electric field profile over the proposed substrate.

2.5 SERS measurements

Benchtop Raman setup was used to perform SERS measurements using excitation wavelength of 785 nm of 200mW power. ANDOR Kymera 328i-B2 spectrometer is used to record signal. 40x microscopic objective with numerical aperture of 0.65 is used for signal collection.

3. Results and discussion

Commercially available software, Lumerical FDTD solution which is based on Maxwell's partial differential equations has been used to analyse the electromagnetic fields enhancement in Ag/Au mirror based SERS substrate. Simulation results (Fig. 2) illustrate that enhancement increases when we use Au/Ag mirror. The blue to red colour bar represents the increasing intensity of the electric field. The formation of hotspots between Au nanoparticles can be distinctly observed. Theoretical enhancement factor (EF) is found to be $\approx 8.65 \times 10^5$ with Au mirror when illuminated with Gaussian source of 785nm, which is 4 times more without mirror.

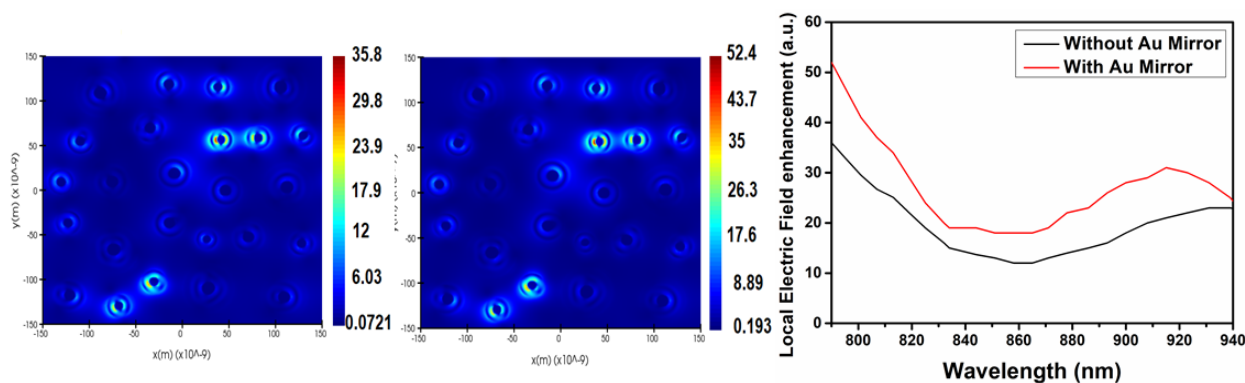


Fig. 2: FDTD results showing electric field profile comparison of with and without Au mirror.

Figure 3 shows TEM image of synthesised Au NPs. It can be inferred from the TEM image that size of nanoparticles is in the range of 10-40nm, which effectively broadens the resonance wavelength of the proposed SERS substrate and thus helps in detecting variety of analytes.

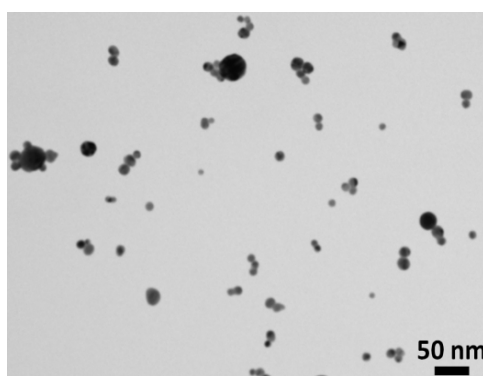


Fig. 3: TEM image of Au nanoparticles

Figure 4(a) shows the comparison of SERS spectra of R6G of 10^{-4} M concentration over Au nanoparticles coated Au/Ag mirror with pristine substrate. It can be inferred from Fig. 4(a) that dispersion of nanoparticles over Au/Ag mirror gives better Raman signal. It is observed that Au nanoparticles in combination with Au mirror give best enhancement in the SERS signal in comparison to Ag mirror. SERS spectra reveal that the presence of Au/Ag coating improves the overall enhancement and can be considered as an example of “energy harvesting”, where optical energy which otherwise would have escaped, after getting reflected is reinvested for improving enhancement further. Proposed SERS-active substrate detected R6G up to 10^{-6} M concentration using benchtop setup at our lab. Further study is underway to find its sensitivity capabilities using commercially available Raman spectrometers like Renishaw, WITec, etc.

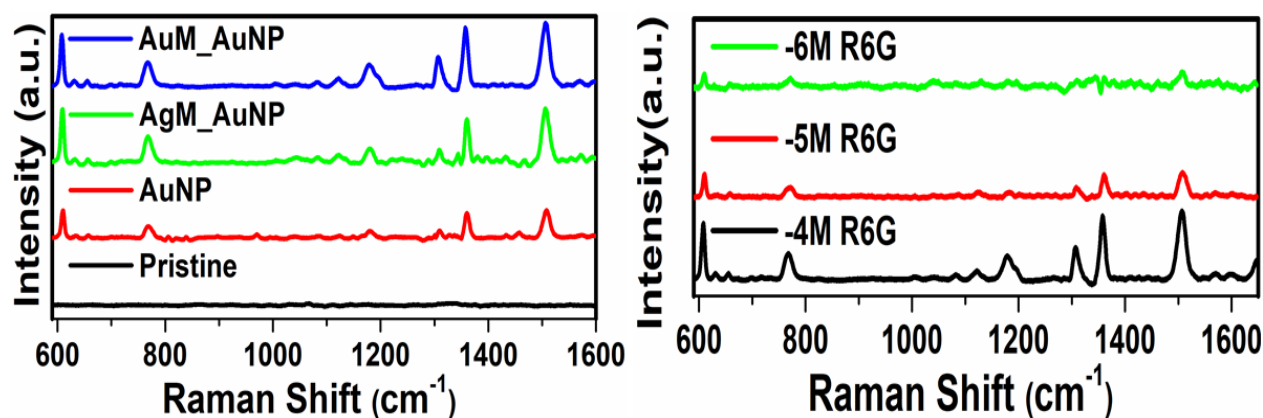


Fig. 4: SERS spectra of (a) 10^{-4} M R6G over different combinations of Au/Ag mirror and Au NPs (b) 10^{-4} M, 10^{-5} M, 10^{-6} M R6G over Au NP coated Au mirror at excitation wavelength of 785nm.

4. Conclusion

The authors have demonstrated that the presence of Au/Ag coating improves the overall SERS enhancement. The Au NPs gives rise to excitation of SPP, thereby ensuring electromagnetic enhancement. The thin Ag/Au layer at the bottom, produces a reflected wave which upon interaction with NPs from below, produces further enhancement, thereby, increasing the overall light-matter interaction. This concept can be used widely in developing SERS substrate using optically transparent material as base material for SERS active substrate, to amplify the SERS signal. It may find applications in diverse fields, including chemistry, food safety, drug detection, narco-analysis, explosive detection and medical diagnostics.

References

1. E. C. Le Ru and P. G. Etchegoin, *Principles of Surface Enhanced Raman Spectroscopy*. Amsterdam, Netherlands: Elsevier, 2009.
2. P.A. Mosier-Boss, “Review of SERS substrates for chemical sensing,” *Nanomaterials (Basel)*., vol. 7, pp. 142–172, 2017.
3. V. Awasthi, R. Goel, S. Agarwal, P. Rai and S. K. Dubey, “Optical nanoantenna for beamed and surface-enhanced Raman spectroscopy,” *J. Raman Spectrosc.*, vol. 51, no. 11, pp. 2121–2145, 2020.
4. R. Pilot, R. Signorini, C. Durante, L. Orian, M. Bhamidipati and L. Fabris, “A review on surface-enhanced Raman scattering,” *Biosensors (Basel)*., vol. 9, no. 57, 2019.
5. S. S. R. Dasary, A. K. Singh, D. Senapati, H. Yu and P. C. Ray, “Gold nanoparticle based label-free SERS probe for ultrasensitive and selective detection of trinitrotoluene,” *Journal of the American Chemical Society*., vol. 131, no. 38, pp. 13806-13812, 2009.
6. Nanophotonic FDTD Simulation Software - Lumerical FDTD.” <https://www.lumerical.com/tcadproducts/fdtd>

Ultrafast laser-based fabrication of Efficient Anti-reflective Silicon Nitride nano/microstructures for Optoelectronics applications

Pariksha Malik^{1,2}, Santanu Ghosh¹, G.V. Prakash², Pankaj Srivastava¹

¹ Nanotech Laboratory, Department of Physics, Indian Institute of Technology Delhi
New Delhi, India, exammalik1995@gmail.com

² Nanophotonics Laboratory, Department of Physics, Indian Institute of Technology Delhi
New Delhi, India, santanu1@physics.iitd.ac.in

Abstract

As an alternative to conventional lithography-based production, simple ultra-fast laser writing is investigated and shown for the fabrication of silicon nitride (SiN_x) microstructures. The propagation of femtosecond pulses is structurally characterised by quasi-a-periodic surface patterns, V-shaped craters, re-casted melt, and debris. These protocols generated unique microstructures with surface quality on par with conventional lithographic production methods. For a range of optoelectronics applications, including photovoltaic applications, where the ability to reduce light reflection is crucial, the recommended methodology should allow for exact control of desired feature sizes, enabling for large-scale and economical microstructure fabrication. The practical antireflection surfaces are necessary to fulfil the varied requirements in broadband efficiency, pliable fabrication, and production stability. We present and experimentally manifests a kind of chaotic, hierarchical micro-nano structure constructed on SiN_x surfaces that exhibits remarkable absorption capabilities spanning the broad spectrum from ultraviolet to near-infrared. The SiN_x surface's average specular reflectance is dramatically decreased by 65-60% in the wavelength range of 200–1200 nm. Such a broadband antireflection structure can be generated in any pattern required thanks to a contact-free, mask-less, straightforward ultrafast laser writing technique. Along with its antireflective quality, the hierarchical structure also offers outstanding self-cleaning abilities. It is a promising contender for real-world optoelectronics applications because of all of these advantages, including broadband efficacy, patterning adaptability, and structural durability.

Keywords: Silicon nitride, Ultrafast laser, Laser texturing, Nano/micro structuring, Laser-matter interaction, Solar cells, Optoelectronics applications.

1. Introduction

Numerous essential applications, including as photovoltaic collection and conversion, artificial blackbody, photodetectors, stray light shielding, infrared imaging, secrecy, along with space-borne optics, etc., vitally rely on the ability to minimise or considerably reduce reflectance in the broad spectrum [1,2]. In order for photovoltaic power generation to be a viable solution to the world's energy crisis, it is imperative to increase solar cell efficiency. One strategy is to increase the amount of sunshine that reaches the photo-conversion layer. Many methods have been devised to pattern Silicon Nitride (SiN_x), including photolithography with wet etching in acidic solutions [3,4]. Toxic chemicals, expensive machinery, and a few steps in the process are all required for this procedure [5]. A nonlithographic or direct patterning technique must be developed in order to create small structures with clearly defined edges on SiN_x thin film. Generically, the pulsed beam irradiates a moving surface to produce nano-, micro-, and/or macroscale structures with predetermined patterns. Depending on the geometry and physical mechanism underlying the process, which may be a pure thermal ablation process or a nonthermal process, these patterns may be referred to as self-assembled structures, pseudo periodic structures, or manufactured patterns.

Due to its benefit in regionalized heating and material expulsion, laser ablation—the ejection of materials from a substrate by direct absorption of laser energy can produce the essential mix of narrow and clean patterning. Teams of researchers investigated the effects of femtosecond laser pulses on a variety of materials, including silicon, aluminium, and indium tin oxide (ITO), in the presence of air, water, and sulphur hexafluoride (SF₆) [4-5]. The current study describes the creation of nanostructures on SiN_x over silicon substrates utilising femtosecond laser writing in an air medium, as seen in Figure 1. With a diameter of between 300 and 400 nm, these micro/nanostructures mimic structures. It has been found that the interaction of femtosecond pulse-induced plasma with a SiN_x/Si substrate leads to the formation of micro/nanostructures. At the SiN_x-air contact,

a plasma is created by the high light absorption in a thin SiNx/silicon layer. After the plasma has balanced with the air and SiNx surrounding it, a layer of molten silicon forms on the surface. These manufactured structures have also been examined using scanning electron microscopy (SEM), Raman spectroscopy, cross-section FESEM, and a UV-VIS spectrophotometer for optoelectronics uses like photovoltaic and surface enhanced Raman spectroscopy (SERS). Average specular reflectance of roughly 35–40% is achieved in the 200–1200 nm range, and an average absorptance of 65–60% is found between 0.2–1.2 μm . The material's ease of usage, patterning adaptability, boosting potential, structural dependability, and self-cleaning quality can satisfy the requirements for practical light-harvesting applications.

2. Experimental section

2.1. Deposition of the silicon nitride film

The substrate was a p-type Si wafer with a crystal orientation of (100), which was cleaned ultrasonically with propanol and DI water before being treated with a 20 percent concentration of HF acid solution in DI water to remove the silicon's native oxide layer. Using the low temperature PECVD (Plasma Enhanced Chemical Vapor Deposition) process (Samco, Model: PD-2S) with NH₃ and 4% SiH₄ in Argon gas as precursor gases, stoichiometric amorphous hydrogenated silicon nitride (a-SiNx:H) films were created for 30 minutes. The rf power (25W), deposition temperature (200°C), and deposition pressure (1mbar) remained consistent for all films during deposition.

2.2. Fabrication of the hyper-hierarchical structure

Over silicon nitride film, the micro/nanostructures were formed using a femtosecond amplifier laser system (800 nm, 120 fs, 1 kHz). For the micro/nano manufacturing process, an amplifier that creates a linearly polarised Gaussian beam with pulse energy of 4.0 mJ/pulse, pulse width of 120 fs, and a maximum repetition rate of 1 kHz with a central wavelength of 800 nm was used. A line-like pattern was created on the film surfaces by focusing and scanning the laser beam with an x-y galvo. The production of silicon nitride over silicon substrate was accelerated, and silicon nitride remained stable during the interaction of laser pulses with film, thanks to the galvo scanner's speed optimization, which was made to move at a speed of 0.1 mm/s. During the optimization process at greater speeds, abnormal patterns were seen. The focused spot had a diameter of around 10 μm and was identified by an intensity reduction to $1/e^2$ of its greatest value. The excitable structure was constructed using the following laser processing parameters: short pulse energy, rate of pulse repetition, scan speed, and line spacing, all at 75 mW, 1 kHz, 0.1 mm s⁻¹, and 100 μm respectively. The micro-structured silicon nitride substrate was created using the experimental process illustrated schematically in figure 2 and using a femtosecond fibre laser. As a texturing environment, ambient air was used during the studies. After laser processing, the samples were flushed with argon gas gun to remove ablated material from the surface.

2.3. Material characterization

An optical microscope (Leica Model:DM750) was first used to analyse the generated micro/nanostructures on the silicon nitride film surface, and the results were then confirmed using a scanning electron microscope (SEM) (Model: Zeiss EVO 50). A pattern gap layer has been added between the patterned layers network in the cross-section Field Emission SEM (Company Name: Jeol Japan; Model: JSM-7800F Prime). Utilizing Stylus Type Surface Profiler, it was possible to gauge the degree of the hierarchical structure or pattern (Model: Alfa Step IQ, KLA-T). The measurement parameters used in profilometry are, in order, 500 μm , 50 Hz, 10 sec, 550 μm per 32.8 pm, and 0.2 μm for the sensor range, resolution, scan length, sampling rate, and time, respectively.

2.4. Optical measurements

Using a Shimadzu UV-VIS-NIR (Model: UV-3600) Spectrophotometer, optical reflectance measurements were done on the antireflection structure created using a femtosecond laser. In addition, the specular reflectance for optoelectronics applications like solar cells at normal incidence was determined in the UV-VIS-NIR spectral region (200-1200nm) as a function of wavelength.

3. Results and Discussion

The main goal of the work is to build a particular class of hierarchical structures with larger size, width, and length extending to adequately larger micrometer dimensions while retaining the disordered and hierarchical

nanometer-scale constituent characteristics, as schematically illustrated in Fig. 1. This kind of hierarchical structures can offer more and a large number of traps along with prolonged paths for the incident light, in contrast to the stated disordered and chaotic nanostructures that can merely be useful for wideband antireflection in the UV-visible range. As a result, it is possible to greatly increase the likelihood that light will be absorbed, leading to an antireflection performance that is noticeably broadened and improved for both visible wavelength and much lower electromagnetic frequency ranges.

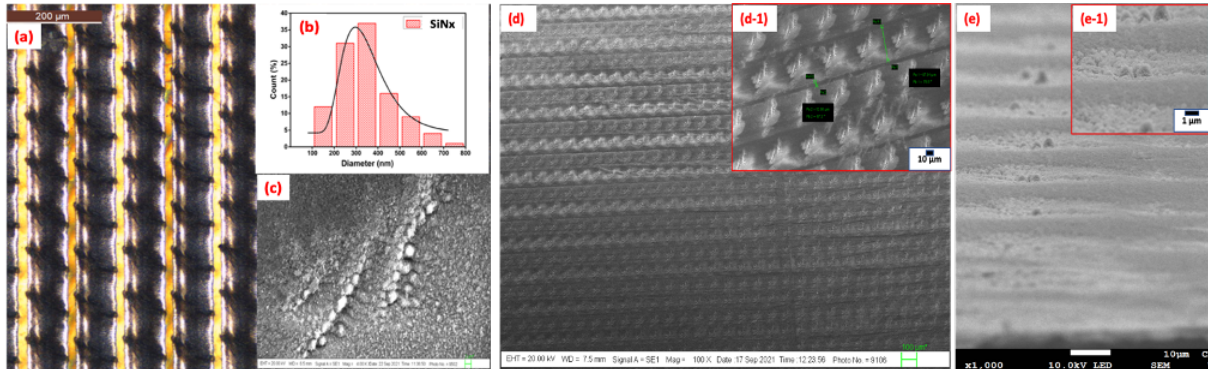


Fig. 1: (a) Figure illustrating the optical microscope photograph of femtosecond laser patterned SiNx has a refractive index of 1.9 on Si substrate. (b-c) The inset figure shows Nano/microstructures fabricated along with their particle size distribution histogram fitted with gaussian distributions indicating 300-400 nm diameter after laser texturing. (d)- (d-1) Top-view scanning electron microscope (SEM) photographs of the hierarchical nano/microstructures in various magnifications (e)–(e-1) Cross-sectional field emission scanning electron microscopy (X-FESEM) images of the hierarchical structure show debris fall at the surface of SiNx.

The Silicon nitride (SiNx_30min) thin film is preliminary characterized using null ellipsometry to determine the refractive index (~ 1.9) and thickness (~ 530 nm). The optical microscope images have been taken to see the laser writing on it which indicates that width of pattern and pattern gap are $20\mu\text{m}$ and $100\mu\text{m}$ respectively. The stylus profilometry has been done to determine the depth of the pattern which is approximately ~ 496 nm. To investigate the further micro-nano structures formation due to texturing, the high resolution scanning electron microscopy (SEM) has been done. The cross-sectional FESEM high-resolution photograph of the fabricated SiNx film is indicated in figure 1(e) which clearly shows 5° tilted top view along with the presence of a pattern gap layer in between patterned layers network. In case of texturing in air medium, some dislodged particle remained at the sample surface and affected the structural modification. The thicknesses of these layers are determined experimentally using SEM & Optical microscopy photographs. Fig1(b) depicted the maximum of nano/microstructures fabricated along with their particles size distribution histogram is having the 300-400 nm diameter which is fitted with gaussian distributions.

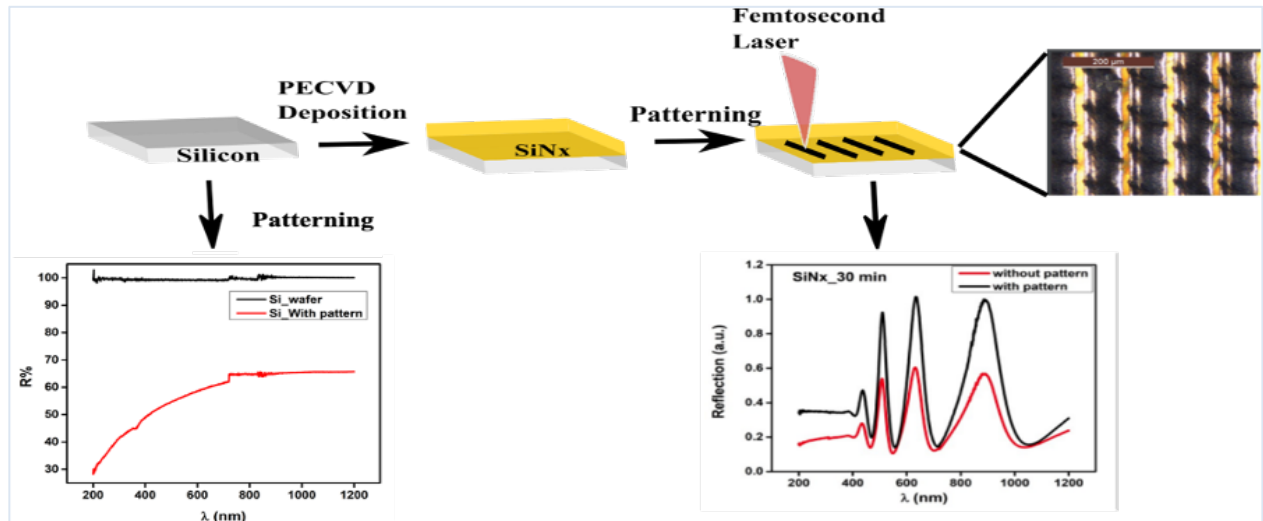


Fig. 2: (a). The schematic diagram of the experimental process has been followed during the fabrication of periodic structures associated with nano-micro structuring which clearly manifested that reflectance has been decreased for both Si and SiNx after laser writing as compared to bare Si and SiNx.

When it comes to absorbing light, hierarchies made of micrometric repetitive grooves covered with numerous nanometric features perform even below $1.2 \mu\text{m}$, but fall short in higher wavelength regions. [6,7]. Particularly, the individual nanometric and only one micrometric surface structures might often be effective in the visible and ultraviolet light bands, respectively for both Si substrate and SiNx film. The hyper-hierarchical micro-nano structure described in this article can gradually collect all incident light while reflecting almost small of it, with no discernible frequency dependency. Average specular reflectance of roughly 35–40% is achieved, and an average absorptance of 65–60% is found between $0.2\text{--}1.2 \mu\text{m}$ for patterned SiNx. Also, in the case of Si, reflectance is decreased by about 40% for 600nm wavelength. Given that the extremely disordered and randomly scattered surface features frequently exhibit homogeneous scatter, we can assume that the resultant broadband antireflection capabilities will be free from any incidence angle dependence.

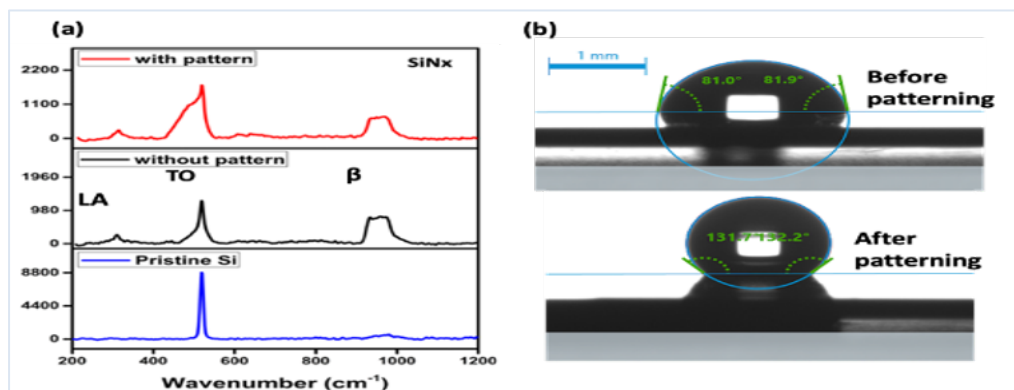


Fig. 3: (a). The Raman spectra of SiNx_30min near stoichiometric composition film showing vibration modes such as LA, TO along with the presence of β -phase with and without patterning. (b) Super hydrophobicity of the SiNx film before patterning (shown in top image) and after patterning broadband anti-reflective pattern surface demonstrating the absence of wetness. A photo image of an one water droplet on the surface of an anti-reflective structure exhibiting a contact angle of 132° as compared to non-patterned indicating a contact angle of 81° .

It is shown in the figure 3(a) that the Raman spectra has been measured using the excitation laser wavelength 532nm to study the various vibration modes. Here, the transverse optical TO (\sim at 430 cm^{-1}) mode of Si-Si vibrations in the crystalline phase, or the Si substrate, is responsible for the main peak, which is centred around 521 cm^{-1} . The longitudinal acoustic phonon mode (LA), which has a peak at about 330 cm^{-1} , is caused by either Si(100) or Si nanocrystals. Coordination defects caused by hydrogen incorporation in the SiNx stoichiometric

film, may also be the cause of these coordination defects. After femto-laser patterning, the peak at 430 cm^{-1} in the SiNx film has a dramatically increased intensity due to heat/chemical modifications, bonds breaking, and plasma ablation, which improves the aggregation of silicon nanocrystals and may also allow unreacted silicon atoms to form clusters.

It has been discovered that the distinctive hierarchical structure has additional characteristics in addition to its broadband antireflection capabilities, including a wide water contact angle. The water drops on the hierarchy maintain their spherical shape, as illustrated in Fig. 3b. There hasn't been any dripping or soaking of the surface or spread of the droplets of water of the building. A $4\text{ }\mu\text{L}$ water droplet's contact angle with SiNx before patterning and broadband antireflection surface after patterning was measured to be 81° and 132° respectively (Fig. 3b). SiNx films are known to lean toward hydrophilicity with a contact angle less than 90 degrees because of their substantial surface free energy. This proves unequivocally the advantages of the hierarchical structure for achieving super-hydrophobicity, with or without the need for any specific surfaces chemical alteration by any substances with minimal surface free energy. No water droplets may remain on the surface of a hierarchical structure, indicating that this structure also has an attractive self-cleaning function in addition to its broadband antireflection capabilities. Using that as a foundation, simple removing dust and repelling water could be achieved, eliminating the risks they provide to the efficacy of optical antireflection. Because of this, the hierarchical form is advantageous for optoelectronics applications such as photovoltaics used in abrasive working conditions.

4. Conclusion

In this study, we show that the broad-band wavelength absorption in the Si and SiNx layer over a silicon substrate is caused by forward scattering and internal reflections between periodic grooves as well as micro/nanostructures formed. After laser writing stoichiometric SiNx film, the laser pattern width, pattern gap, and pattern depth were all confirmed by optical microscopy and a stylus optical profiler. The size of maximum nano-structure particles ranges from 300–400 nm, while the size of maximum micro-structure particles is 2–2.5 μm , as shown by SEM and X-FESEM pictures of SiNx film. Raman spectroscopy was used to learn more about the β -Si₃N₄ phase as well as the LA, and TO vibration modes that can change with or without a pattern. In the range of 0.2–1.2 μm , patterned SiNx exhibits an average specular reflectance of around 35–40% and an average absorbance of 65–60%. Furthermore, reflectance at 600 nm wavelengths is reduced by nearly 40% in the case of Si. By increasing the density of crater vacancies and reducing the interspacing of ridges, it is possible to further improve the absorptivity of constructed structures. Additionally, its ultrabroadband antireflection structure's hyper-hierarchical characteristic gives it remarkable super hydrophobicity and self-cleaning properties. Using a femtoscale fibre laser, a workable strategy to improve light harvesting on a commercial c-Si solar cell was presented, providing a quicker and more affordable alternative to conventional fabrication methods.

Acknowledgements

Financial support from the CSIR in the form of a sponsored research project is acknowledged. PM acknowledges the UGC for JRF/SRF fellowship. The departmental facilities (DST-FIST) and central facilities of IIT Delhi, NRF and CRF (funded by Government of India, IIT Delhi, New Delhi, India) are acknowledged for providing fabrication and characterization facilities.

References

1. S. John, Why trap light, *Nat. Mater.* 11, pp. 997–999, 2012.
2. H.K. Raut, V.A. Ganesh, A.S. Nair, S. Ramakrishna, Anti-reflective coatings: a critical, in-depth review, *Energy Environ. Sci.* 4, pp. 3779–3804, 2011.
3. M.A. Kats, R. Blanchard, P. Genevet, F. Capasso, Nanometre optical coatings based on strong interference effects in highly absorbing media, *Nat. Mater.* 12, pp. 20–24, 2013.
4. Hoheisel M, Mitwalsky A and Mrotzek C, Microstructure and etching properties of sputtered indium—tin oxide (ITO), *Physica Status Solidi (a)* **123**, pp. 461–72, 1991.
5. Stratakis E, Zorba V, Barberoglou M, Fotakis C and Shafeev G A, Femtosecond laser writing of nanostructures on bulk Al via its ablation in air and liquids, *Applied Surface Science* 255, pp. 5346–50, 2009.

6. G.Tang, A.C. Hourd, A. Abdolvand, Nanosecond pulsed laser blackening of copper, *Appl. Phys. Lett.* 101, pp. 231902, 2012.
7. A.Y. Vorobyev, C. Guo, Direct femtosecond laser surface nano/micro structuring and its applications, *Laser Photonics Rev.* 7, pp. 385–407, 2013.
8. Vinod Parmar, G. Vijaya Prakash, and Dinesh Kalyan Sundaram, Fabrication of Anti-reflective Micro structured Silicon Surfaces Using Nanosecond Fibre Laser Texturing, *Light, Energy and the Environment (E2, PV, SOLAR, SSL)*, 2017.

Permeability assay and inflammatory marker quantification of lactoferrin functionalized lipid nanoparticles intended for brain delivery

Maria Inês Teixeira^{1,2,*}, Carla M. Lopes³, Henrique Reguengo⁴, José Carlos Oliveira⁴, Ana Margarida Silva⁵, Francisca Rodrigues⁵, Maria Helena Amaral^{1,2,*}, Paulo C. Costa^{1,2,*}

¹ UCIBIO – Applied Molecular Biosciences Unit, MedTech – Laboratory of Pharmaceutical Technology, Department of Drug Sciences, Faculty of Pharmacy, University of Porto, Rua de Jorge Viterbo Ferreira, 228, 4050-313, Porto, Portugal

² Associate Laboratory i4HB – Institute for Health and Bioeconomy, Faculty of Pharmacy, University of Porto, Rua de Jorge Viterbo Ferreira, 228, 4050-313, Porto, Portugal

³ FFP-I3ID – Instituto de Investigação, Inovação e Desenvolvimento, FP-BHS – Biomedical and Health Sciences Research Unit, Faculdade Ciências da Saúde, Universidade Fernando Pessoa, Rua Carlos da Maia, 296, 4200-150 Porto, Portugal

⁴ Clinical Chemistry, Department of Laboratory Pathology, Centro Hospitalar Universitário do Porto (CHUP), Largo Prof. Abel Salazar, 4099-313, Porto, Portugal

⁵ REQUIMTE/LAQV – Polytechnic of Porto, School of Engineering, Rua Dr. António Bernardino de Almeida, 4229-015, Porto, Portugal

*Corresponding authors: up201410537@edu.ff.up.pt; pccosta@ff.up.pt; hamaral@ff.up.pt

Abstract

Amyotrophic lateral sclerosis (ALS) is a neurodegenerative disease with a survival rate of 3 to 5 years from the onset of symptoms. ALS treatment is compromised by the existence of the blood-brain barrier (BBB), which restricts the access of promising biopharmaceuticals to the brain, including riluzole, a drug commonly used to treat ALS. To circumvent the BBB and improve the drug brain targeting, nanosystems such as lipid nanoparticles can be employed. In this work, the permeation of nanostructured lipid carriers (NLC) loaded with riluzole and functionalized with a specific ligand – lactoferrin – was assessed in an *in vitro* BBB model (hCMEC/D3 cell line). Moreover, the effect of the NLC on the production and secretion of the pro-inflammatory cytokine human interleukin 1 alpha (IL-1 α) by the cells was also quantified. The permeability studies across the hCMEC/D3 cell monolayers showed that free riluzole penetrated the BBB more than the riluzole-loaded NLC, which was also consistent with the results from the ELISA kit, with the free drug eliciting a higher IL-1 α production. Despite these findings, the developed nanocarriers possessed good biocompatibility and stability, and could, therefore, be considered suitable for brain applications.

Keywords: Blood-brain barrier (BBB), brain delivery, neurodegeneration, amyotrophic lateral sclerosis (ALS), functionalized lipid nanoparticles, nanostructured lipid carriers (NLC), riluzole, lactoferrin.

1. Introduction

Neurodegenerative diseases, such as Alzheimer's disease, Parkinson's disease, multiple sclerosis, or amyotrophic lateral sclerosis (ALS) are highly prevalent worldwide. They account for around 14% of all global illnesses, and it is estimated that 1.5 million individuals suffer from one of these ailments [1]. Among these, ALS is the most quickly progressing, with patients gradually losing the capacity to control muscular action, eventually leading to full paralysis in the late stages of the disease. This is caused by the degeneration of both upper and lower motor neurons in the brain and spinal cord, which results in denervation and progressive muscular atrophy [2]. Several factors, including genetic mutations (e.g., superoxide dismutase type 1 (SOD1), TDP-43 or C9ORF72 gene mutations), intracellular protein aggregation, mitochondrial dysfunction, free radicals, excitotoxicity, and inflammation, have all been linked to the development of ALS. Nevertheless, determining which of these processes are causative remains challenging [3]. Due to the complex nature of the disease, the presence of the blood-brain barrier (BBB)/blood-spinal cord barrier, as well as poor biostability/bioavailability and off-target effects, most of the ALS therapies have had little effectiveness. As a

result, only two disease-modifying drugs, riluzole and edaravone, are currently licensed for use, providing modest benefits in certain patients [4].

To address the significant socioeconomic impact of ALS, innovative therapeutic strategies are urgently required. In this context, nanoformulations might be an effective approach to overcome the BBB and allow the drug to reach its intended target, i.e., the brain. Nanocarriers can effectively encapsulate and protect the therapeutic agents, while also avoiding extensive systemic distribution [5]. Lipid nanocarriers, such as liposomes, solid lipid nanocarriers (SLN), nanostructured lipid carriers (NLC), or nanoemulsions, are particularly advantageous for central nervous system (CNS) delivery, since they are generally made of GRAS (generally recognized as safe) excipients, have high biocompatibility, low cytotoxicity, and can be conjugated with several ligands or coating materials to aid and increase transcytosis across the BBB [6]. We have previously developed lactoferrin functionalized NLC to facilitate riluzole transport to the CNS [7]. Lactoferrin was selected as a ligand because receptors for this glycoprotein have shown to be overexpressed on BBB endothelial cells in instances of neurodegeneration, promoting receptor-mediated transcytosis to the brain [8].

The aim of this study was to test the permeation of lactoferrin functionalized lipid nanoparticles in an hCMEC/D3 cell monolayer, which is one of the most reliable human BBB *in vitro* models. Moreover, an enzyme-linked immunosorbent assay (ELISA) kit was used to examine and quantify the effect of the nanocarriers on the release of the pro-inflammatory cytokine human interleukin 1 alpha (IL-1 α) by the cells.

2. Materials and methods

2.1. Materials

For nanoparticles preparation, Precirol[®] ATO5 (glyceryl distearate/glyceryl palmitostearate) was kindly provided by Gattefossé (Nanterre, France), and Kolliphor[®] P188 micro Geismar (Poloxamer 188), by BASF (Ludwigshafen am Rhein, Germany). Mygliol[®] 812 (triglycerides of capric/caprylic acids), Tween[®] 80 (polysorbate 80), and stearic acid were acquired from Acofarma (Madrid, Spain), and riluzole (purity > 98%), from Beantown Chemical (Hudson, NH, USA). For nanoparticles functionalization, N-hydroxysuccinimide (NHS), N-(3-Dimethylaminopropyl)-N'-ethylcarbodiimide hydrochloride (EDC), and recombinant human lactoferrin were purchased from Sigma-Aldrich (Steinheim, Germany).

For cell culture studies, immortalized human cerebral microvascular endothelial cells (hCMEC/D3 cell line) were purchased from Cedarlane (Hornby, ON, Canada). EndoGRO[™] basal medium and EndoGRO-MV Complete Culture Media Kit were obtained from Merck (Darmstadt, Germany). Hank's balanced salt solution (HBSS), collagen I rat protein and trypsin-EDTA were purchased from Gibco[™] (Thermo Fisher Scientific, Waltham, MA, USA). Human IL-1 α /IL-1F1 Quantikine[®] ELISA kit was obtained from R&D Systems (Minneapolis, MN, USA).

All the other reagents were of analytical grade and used as supplied. The purified water used in all experiments was as obtained from a Milli-Q[®] Direct 3 UV-R system (Millipore, Darmstadt, Germany).

2.2. Preparation of lipid nanoparticles and functionalization with lactoferrin

The nanoparticles were produced according to an optimized hot homogenization technique followed by ultrasonication, under the same conditions described in a previous work [7]. Afterwards, the NLC were functionalized with lactoferrin by carbodiimide chemistry. Briefly, 10 mL of riluzole-loaded NLC (NLC Riluzole) was incubated with 22.5 mL of a lactoferrin solution (1 mg/mL of lactoferrin in phosphate-buffered saline (PBS), pH 7.4) at room temperature for 4 h with gentle stirring, in the presence of EDC and NHS [7].

2.3. hCMEC/D3 cell culture

The hCMEC/D3 cell line is extensively used as a model of the human BBB due to its characteristics, such as being easily grown and reproducible, present tight junctions or specific transporters, closely reflecting the *in vivo* phenotype [9]. Immortalized human cerebral microvascular endothelial cells were grown in EndoGRO[™] basal medium supplemented with FBS (5%, v/v), rhEGF (5 ng/mL), L-glutamine (10 mM), ascorbic acid (50 μ g/mL), EndoGRO-LS supplement (0.2%, v/v), hydrocortisone hemisuccinate (1.0 μ g/mL), and heparin sulfate (0.75 U/mL). The cells were maintained in an incubator (Cell Culture[®] CO₂ incubator, ESCO GB Ltd., Barnsley,

England, UK) at 37 °C in a water-saturated atmosphere with 5% CO₂ and subcultured every 2–3 days using trypsin-EDTA to detach them from the flasks. The culture medium was replaced every other day.

2.3.1. Transwell permeability assay

hCMEC/D3 cells were seeded at a density of 2.5×10^4 cells per insert in transwell devices (6-well polyester inserts, effective area: 4.2 cm², pore size: 0.4 μm and pore density: $100 \pm 10 \times 10^6/\text{cm}^2$) pre-coated with 50 μg/mL collagen I rat protein in 0.02 M acetic acid [10]. The apical and basolateral chambers of the inserts were filled with supplemented EndoGRO™ basal medium, and cells were incubated until confluence (8 days), replacing the medium each 2 days. To ensure the integrity of the hCMEC/D3 monolayer, the transendothelial electrical resistance (TEER) was measured with an epithelial voltohmmeter (EVOM) (World Precision Instruments, Sarasota, FL, USA) every time the culture medium was changed, and additionally, throughout the permeability studies [10].

Permeability studies were performed after 8 days of seeding. The culture medium was previously replaced by Hank's balanced salt solution (HBSS), as isotonic buffer solution. The riluzole-loaded NLC and free riluzole samples with 10 μM concentration were incubated in the apical donor compartment for 24 h at 37 °C in 5% CO₂, and the total amount of riluzole in the basolateral acceptor compartment was quantified after 0, 0.5, 1, 1.5, 2, 2.5, 3, 3.5, 4, 8 and 24 h by High Performance Liquid Chromatography – Mass Spectrometry (HPLC-MS).

2.3.2. High Performance Liquid Chromatography – Mass Spectrometry (HPLC-MS)

The concentration of riluzole in the basolateral compartment of the transwell device was quantified by HPLC-MS, following a method that was developed in house. A reversed-phase C18 column (BDS Hypersil™ C18 column, 150 mm × 4.60 mm internal diameter, 5 μm particle size; Thermo Fisher Scientific, Waltham, MA, USA) was connected to an HPLC-MS system (LCMS-8050 model, Shimadzu®, Kyoto, Japan). Chromatographic separation was achieved by isocratic mode consisting of methanol/water pH 3 80:20 (v/v) as the mobile phase, eluted at a flow rate of 1 mL/min. Injections were made in triplicate ($n = 3$), with a sample volume of 10 μL. The oven and sampler temperature were set at 45 °C and 15 °C, respectively. A calibration curve was made by using independent standard solutions of riluzole in ethanol (0.375–2.4 μg/mL) and fitting the respective data to the least squares linear regression, which gave a correlation coefficient (R) of 0.9994.

2.4. Enzyme-linked immunosorbent assay (ELISA)

The secretion of IL-1α after 24 h of incubation with the NLC dispersions and free riluzole from the hCMEC/D3 cell model to the culture medium was quantified using the Human IL-1α/IL-1F1 Quantikine® immunoassay kit, according to the protocol provided by the manufacturer [11, 12].

Briefly, 200 μL of cell culture supernatant samples collected after 24 h of exposure during the transwell permeability assay, and 50 μL of assay diluent were added to anti-IL-1α monoclonal antibody-precoated microplate wells and incubated for 2 h at room temperature [12]. Afterwards, the horseradish peroxidase-conjugated secondary antibodies were added to the pre-washed test samples and the plate was incubated for 1 h at room temperature. Then, the substrate solution was added, and the plate was incubated for another 20 min. The chemical reaction was stopped by the adding of 50 μL of 2 N sulfuric acid. UV-visible spectrophotometric measurements were performed at 450 nm using a microplate reader (Synergy HT, Bio-Tek Instruments, VT, USA), with wavelength correction at 570 nm. A calibration curve was used to calculate the concentration (R = 0.991).

3. Results and Discussion

3.1. Permeability assay

The permeation profiles of riluzole-loaded NLC (functionalized and non-functionalized) and the free drug are shown in Figure 1.

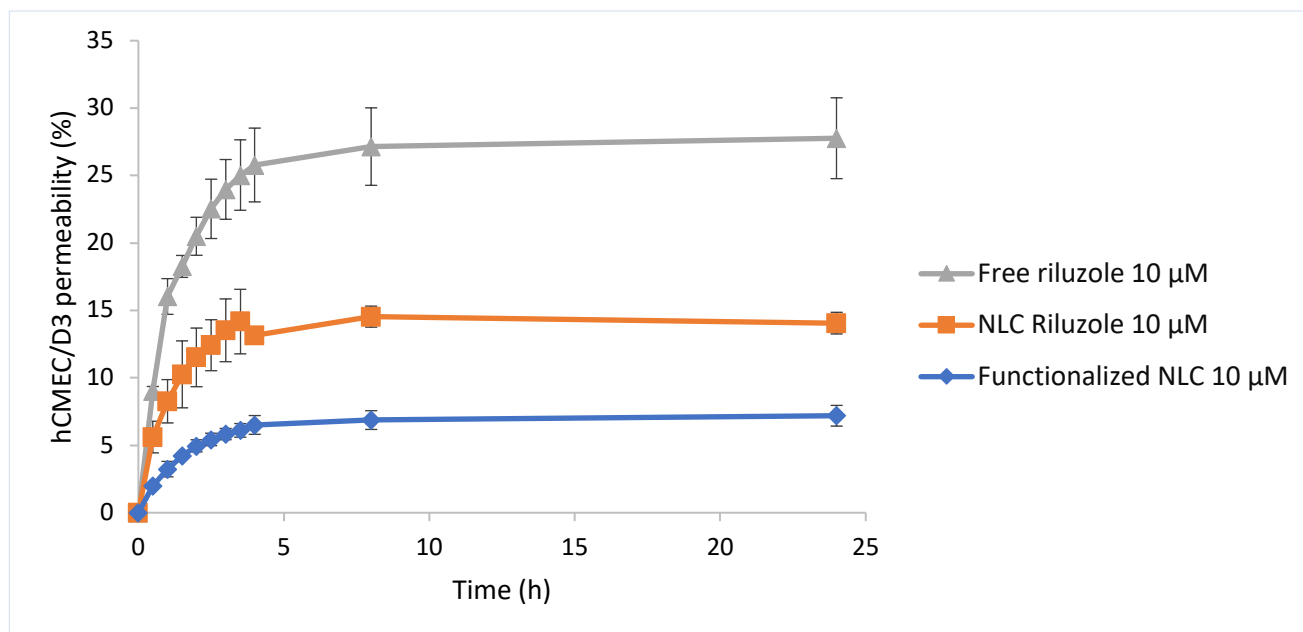


Fig. 1: Permeation profiles of the NLC and free riluzole (10 µM) through the hCMEC/D3 monolayer over 24 h. All values represent the mean ± standard deviation ($n = 2$).

At a first glance, it is possible to observe that free riluzole had a higher permeability than the NLC, for both non-functionalized and functionalized nanoparticles. BBB permeability is dependent upon the physicochemical characteristics of the molecule, such as its conformation, lipophilicity, or size [6]. Riluzole is a BCS (Biopharmaceutical Classification System) class II drug, being a lipophilic compound with a high affinity for the phospholipids that constitute the cellular membranes of the BBB [13]. Furthermore, free riluzole is molecularly dispersed, having comparatively smaller dimensions than the NLC, which had sizes between 208.5 and 221.9 nm [7]. Both these aspects could have contributed to the higher free drug permeation through the BBB.

On the other hand, the BBB permeation profile of the functionalized NLC was lower in comparison to NLC Riluzole. The functionalized NLC had a zeta potential of -16.41 ± 0.31 mV, while the NLC Riluzole achieved a value of 20.67 ± 2.11 mV [7]. The overall surface charge of BBB is highly negative, due to the phospholipids in the plasma membrane and the glycocalyx [14]. The negative surface charge of the BBB may have led to the repelling of the functionalized NLC, limiting their entrance into the brain, while facilitating the penetration in the case of the NLC Riluzole. Moreover, it has been shown that high concentrations of endogenous proteins (e.g., transferrin) can result in saturation of the binding sites on the BBB receptors, and thus, of uptake mechanisms [15, 16]. It is possible that the high amount of lactoferrin used to prepare the NLC induced receptor desensitization, leading to decreased responsiveness, and hindering receptor-mediated transcytosis of the lactoferrin functionalized NLC [15].

3.2. ELISA

After 24 h of incubation, free riluzole elicited IL-1 α secretion and release (2 pg/mL) in the hCMEC/D3 cell model, while for both NLC dispersions, no IL-1 α was detected. These results are in agreement with the data from the BBB permeation profiles, where the free drug had the highest penetration, and also with the literature, having been demonstrated that interleukin release is related to increased BBB permeability [17].

4. Conclusion

Surface-modified lipid nanoparticles are attractive systems for the treatment of neurodegenerative diseases, potentially enhancing drug delivery and uptake to the brain. Based on our previous work [7], in this study we sought to assess the permeation of lactoferrin functionalized NLC loaded with riluzole in an *in vitro* BBB model, as well as their effect on the secretion of IL-1 α by the cells.

Overall, the results showed that riluzole permeated the BBB more than both NLC (functionalized and non-functionalized), which was also consistent with the ELISA kit results, with the free drug eliciting a higher IL-1 α production. Despite these findings, the developed nanoparticles showed good biocompatibility and stability [7], allowing drug protection from adverse conditions of the physiological environment, and could therefore be considered a safe brain targeting drug delivery system.

Acknowledgements

This work was financed by national funds from FCT - Fundação para a Ciência e a Tecnologia, I.P., in the scope of the projects UIDP/04378/2020 and UIDB/04378/2020 of the Research Unit on Applied Molecular Biosciences - UCIBIO. Maria Inês Teixeira is thankful for the Ph.D. grant (2020.05060.BD) from the Fundação para a Ciência e a Tecnologia (FCT). Ana Margarida Silva is thankful for the Ph.D. grant (SFRH/BD/144994/2019) financed by POPH-QREN and subsidized by the European Science Foundation and Ministério da Ciência, Tecnologia e Ensino Superior. Francisca Rodrigues (CEECIND/01886/2020) is thankful for her contract financed by FCT/MCTES—CEEC Individual Program Contract and for projects UIDB/50006/2020 and UIDP/50006/2020 by the FCT/Ministério da Ciência, Tecnologia e Ensino Superior (MCTES) supported through national funds.

References

1. A. A. Sartaj, Z. Qamar, S. Md, N. A. Alhakamy, B. Sanjula and A. Javed, “An Insight to Brain Targeting Utilizing Polymeric Nanoparticles: Effective Treatment Modalities for Neurological Disorders and Brain Tumor,” *Frontiers in Bioengineering and Biotechnology*, vol. 10, 2022.
2. M. Stroehlein, “ALS: A progressive neurodegenerative disease,” *Nursing made Incredibly Easy*, vol. 16, 2018.
3. R. Mejjini, L. L. Flynn, I. L. Pitout, S. Fletcher, S. D. Wilton and P. A. Akkari, “ALS Genetics, Mechanisms, and Therapeutics: Where Are We Now?,” *Frontiers in Neuroscience*, vol. 13, 2019.
4. X. Xu, D. Shen, Y. Gao, Q. Zhou, Y. Ni, H. Meng, H. Shi, W. Le, S. Chen and S. Chen, “A perspective on therapies for amyotrophic lateral sclerosis: can disease progression be curbed?,” *Translational Neurodegeneration*, vol. 10, pp. 29, 2021.
5. G. Y. Wang, S. L. Rayner, R. Chung, B. Y. Shi and X. J. Liang, “Advances in nanotechnology-based strategies for the treatments of amyotrophic lateral sclerosis,” *Materials Today Bio*, vol. 6, pp. 100055, 2020.
6. M. I. Teixeira, C. M. Lopes, M. H. Amaral and P. C. Costa, “Current insights on lipid nanocarrier-assisted drug delivery in the treatment of neurodegenerative diseases,” *European Journal of Pharmaceutics and Biopharmaceutics*, vol. 149, pp. 192-217, 2020.
7. M. I. Teixeira, C. M. Lopes, H. Gonçalves, J. Catita, A. M. Silva, F. Rodrigues, M. H. Amaral and P. C. Costa, “Formulation, Characterization, and Cytotoxicity Evaluation of Lactoferrin Functionalized Lipid Nanoparticles for Riluzole Delivery to the Brain,” *Pharmaceutics*, vol. 14, pp. 185, 2022.
8. H. L. Gao, Z. Q. Pang, L. Fan, K. L. Hu, B. X. Wu and X. G. Jiang, “Effect of lactoferrin- and transferrin-conjugated polymersomes in brain targeting: in vitro and in vivo evaluations,” *Acta Pharmacol Sin*, vol. 31, pp. 237-43, 2010.
9. A. R. Neves, L. van der Putten, J. F. Queiroz, M. Pinheiro and S. Reis, “Transferrin-functionalized lipid nanoparticles for curcumin brain delivery,” *Journal of Biotechnology*, vol. 331, pp. 108-117, 2021.
10. B. Sánchez-Dengra, I. González-Álvarez, F. Sousa, M. Bermejo, M. González-Álvarez and B. Sarmento, “In vitro model for predicting the access and distribution of drugs in the brain using hCMEC/D3 cells,” *European Journal of Pharmaceutics and Biopharmaceutics*, vol. 163, pp. 120-126, 2021.
11. P. Anantaworasakul, W. Chaiyana, B. B. Michniak-Kohn, W. Rungsevijitprapa and C. Ampasavate, “Enhanced Transdermal Delivery of Concentrated Capsaicin from Chili Extract-Loaded Lipid Nanoparticles with Reduced Skin Irritation,” *Pharmaceutics*, vol. 12, 2020.
12. U. Zlabiene, J. Baranauskaite, D. M. Kopustinskiene and J. Bernatoniene, “In Vitro and Clinical Safety Assessment of the Multiple W/O/W Emulsion Based on the Active Ingredients from Rosmarinus officinalis L., Avena sativa L. and Linum usitatissimum L,” *Pharmaceutics*, vol. 13, 2021.

13. B. Yadav, S. Balasubramanian, R. B. Chavan, R. Thipparaboina, V. G. M. Naidu and N. R. Shastri, “Hepatoprotective Cocrystals and Salts of Riluzole: Prediction, Synthesis, Solid State Characterization, and Evaluation,” *Crystal Growth & Design*, vol. 18, pp. 1047-1061, 2018.
14. A. R. Santa-Maria, F. R. Walter, S. Valkai, A. R. Brás, M. Mészáros, A. Kincses, A. Klepe, D. Gaspar, M. Castanho, L. Zimányi, A. Dér and M. A. Deli, “Lidocaine turns the surface charge of biological membranes more positive and changes the permeability of blood-brain barrier culture models,” *Biochim Biophys Acta Biomembr*, vol. 1861, pp. 1579-1591, 2019.
15. R. G. R. Pinheiro, A. Granja, J. A. Loureiro, M. C. Pereira, M. Pinheiro, A. R. Neves and S. Reis, “Quercetin lipid nanoparticles functionalized with transferrin for Alzheimer's disease,” *European Journal of Pharmaceutical Sciences*, vol. 148, pp. 105314, 2020.
16. J. A. Loureiro, B. Gomes, M. A. Coelho, M. do Carmo Pereira and S. Rocha, “Immunoliposomes doubly targeted to transferrin receptor and to α -synuclein,” *Future Sci OA*, vol. 1, pp. Fso71, 2015.
17. Y. Wang, S. Jin, Y. Sonobe, Y. Cheng, H. Horiuchi, B. Parajuli, J. Kawanokuchi, T. Mizuno, H. Takeuchi and A. Suzumura, “Interleukin-1 β induces blood-brain barrier disruption by downregulating Sonic hedgehog in astrocytes,” *PLoS One*, vol. 9, pp. e110024, 2014.

Tiered Approach Strategy for Occupational Risk Assessment and Management of Lightweight Metals Reinforced with Nanomaterials using Direct Energy Deposition Process

João Laranjeira¹, Cristina Matos¹, Ana Rita Alberto¹, Carla F. Martins¹, Kilian F. Neves², M. Fernanda N. N. Carvalho², Manuel Lai³, Alessandro Asaro³, Daniele Paravidino³

¹ISQ – Instituto de Soldadura e Qualidade
Rua Eng. Valente de Oliveira 19, 2740-254 Oeiras, Portugal, jplaranjeira@isq.pt, mcmatos@isq.pt,
arsoares@isq.pt, cfmartins@isq.pt

²IST – Departamento de Engenharia Química, Instituto Superior Técnico, Universidade de Lisboa
Av. Rovisco Pais 1, 1049-001 Lisboa, Portugal, kfneves@isq.pt, fcarvalho@tecnico.ulisboa.pt

³IRIS s.r.l., Via Papa Giovanni Paolo II, 26, 10043 Orbassano TO, Italy, manuel.lai@irissrl.eu,
alessandro.asaro@irissrl.eu, daniele.paravidino@irissrl.eu

Abstract

The potential occupational exposure risk emerging from the pilot scale production of lightweight metals of Ti-6Al-4V reinforced with 3.8wt% nTiC through the Direct Energy Deposition (DED) process was assessed by following a Tiered approach strategy. After hazard identification of the nanomaterial (NM) and the exposure assessment of the manufacturing process, several control banding tools were applied for an initial risk assessment (Tier 1). The workers exposure to airborne NMs was estimated through an *in-situ* monitorization campaign (Tier 2). Based on the results, additional risk control measures were proposed to reduce the potential inhalation of NMs by workers.

Keywords: exposure assessment, occupational risk assessment, risk management, tiered approach, nanomaterials.

1. Introduction

Nanomaterials (NMs) have been used in a wide number of industries due to nano-scale enhanced material properties. Nevertheless, NMs can pose several hazards to human health due to their specific physicochemical properties (dimensions and shape) that enable them to cross biological barriers without losing their integrity reaching tissues and organs of the human body inaccessible to materials of largest dimensions [1]. The risk posed by the NMs depend on the intrinsic NMs hazards, and risk on the exposure potential, mainly through inhalation which can occur during any stage of materials life cycle. Skin contact and ingestion are also possible routes of exposure, although less common [1]. As the health effects associated with the use of NMs are not yet clearly understood and scarce data exists concerning occupational exposure and occupational exposure limits (OELs) [2], it is necessary to use practices such as the hierarchy of risk controls for NMs, able to decrease the risk through hazard/toxicity control and/or exposure control (material and non-material design approaches, respectively) [3]. In order to optimize the risk assessment and management process of occupational exposure to airborne NMs, a Tiered approach was developed by several international bodies (OECD, CEN, ECHA) as a step-by-step flexible strategy easy to implement and cost-effective, where the degree of complexity increases with each step [1, 4, 5]. Therefore, the level of uncertainty decreases with the increasing number of tiers providing the support for the decision-making process of suitable control measures.

In this study, the Tiered approach strategy was applied (namely Tiers 1 and 2) to assess and manage potential occupational exposure risk associated with a pilot scale production of lightweight metals (Ti-6Al-4V) reinforced with ceramic NMs (3.8wt% nTiC) through the Direct Energy Deposition (DED) process. As an additive manufacturing technique, the Direct Energy Deposition (DED) process uses a focused energy source, such as a laser to melt the material, while it is simultaneously deposited by a nozzle [6]. The lightweight metal reinforced with ceramic NM (Ti-6Al-4V-3.8wt% nTiC) here reported is intended to be used to produce components for transportation, defence and consumer goods industries, under H2020 project LightMe project (814552). Finally, this study aims at contributing to find useful strategies for occupational exposure risk assessment and management of NMs, evidencing that further research is necessary, considering the wide variety of NMs and manufacturing processes available, to ultimately overcome the lack of data on OELs.

2. Methodology

The Direct Energy Deposition (DED) process under analysis in this study uses a nano-additive powder composed by Ti-6Al-4V-3.8wt% nTiC, of density of 4.5 g/cm^3 which was provided by the LightMe project partner. The nano-additive powder is introduced into the process through the powder feeder system, which is connected to the DED instrument through a closed system (Fig. 1a). The DED process takes place inside an inflatable glovebox, which is filled with Argon gas to ensure the quality of the process. The glovebox is inside an enclosed room provided with a safety system that requires the door to be closed and the operator has an authorization permit. Then the produced part is removed, and the operator uses an ATEX-protected vacuum cleaner to recover the un-melted powders inside the glovebox, as only 25% of the powder leaving the nozzle is melted. After opening the ATEX-protected vacuum cleaner inside the enclosed room, the filter is removed and transported to the sieving workstation, where it is discharged into the sieving equipment. After performing the sieving process inside a closed container, the nano-additive powder is storage for future use. Fig. 1a and b shows the scheme of the DED process and related tasks and the pilot scale setting, respectively. This process involves two workers simultaneously in the same activity and is typically performed with a frequency of 4-5 days/week and a duration of 1-30 min/day. The production *per* year is estimated in 1056 kg. Workers use filter masks P3 (FFP3), latex gloves and lab coat during the process under study.

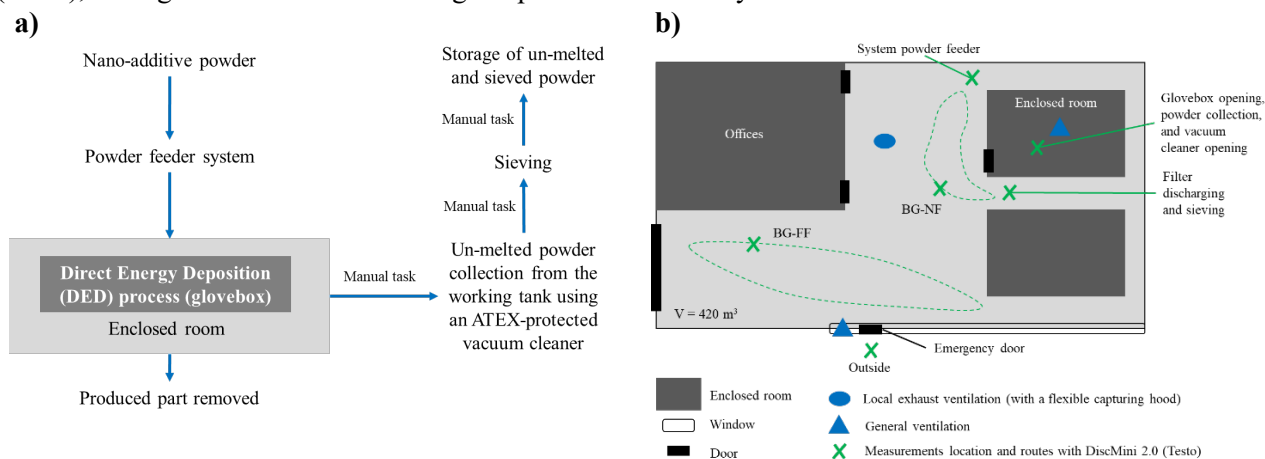


Fig. 1: (a) Scheme of the Direct Energy Deposition (DED) process and associated tasks, and (b) Pilot plant setting of LightMe partner.

The occupational risk assessment due to the exposure to NMs at the DED process and related tasks showed at Fig. 1a was performed in three steps, *i.e.*, qualitative hazard identification, exposure assessment, and risk characterization, rather than in the typical four steps, since the dose-response assessment was not performed [2]. A Tiered approach strategy was applied through an initial risk assessment in Tier 1, followed by the estimation for the potential exposure of the workers to nano-additive powder in Tier 2.

In Tier 1, the initial risk assessment of the process described in Fig. 1a was performed through qualitative hazard identification, exposure assessment, and risk characterization using Control Banding (CB) tools.

Qualitative hazards identification was based on available data on the characteristics of the NMs and nano-products (toxicology, and physicochemical properties [7]) using data sources such as safety data sheets, ECHA portal (Infocard and Brief Profile), PubChem database and literature review. Although safety data sheets should include this type of information, there is limited knowledge about the toxicity of some NMs [7] and consequently, safety data sheets are generally incomplete showing a lack of possible nano-specific health and safety issues [8]. Indeed, the information provided in safety data sheets is typically for the bulk form [8].

Exposure assessment of workers to airborne NMs required the establishment of exposure scenarios, which required a study of the possible sources of NM emissions, the material's morphology, and the characteristics of manufacturing process [7] which include the amount of NM handled, frequency and duration of the activities, the energy introduced by specific processes, and also the safety procedures already in use.

A number of free web-based tools, such as Control Banding (CB) Nanotool v2.0, NanoSafer v1.1 β , and Stoffenmanager Nano v1.0, were used for the initial risk assessment of the nano-additive powders processed through DED (Fig. 1a). These CB tools require input data concerning physicochemical properties and toxicology of materials, manufacturing process, workplace and existing local control measures (the number of input parameters differ between tools [9]). As a semi-quantitative output, a two-dimensional risk matrix is obtained to estimate the levels of precaution required to control their risk, based on hazard and exposure potential to NMs inhalation [9] of the case study (the number of control bands differs between tools [9]). While the CB Nanotool v2.0 and the NanoSafer v1.1 β follow a score-based approach for both hazard and exposure, the Stoffenmanager Nano v1.0 follows a decision tree approach for hazard and a score-based approach concerning exposure [10]. Therefore, the risk assessment in the three tools differs in the fact that the Stoffenmanager Nano v1.0 enables to select more diverse control measures (both material and non-material design measures), implement them directly on the tool; and then re-evaluate the process and material based on risk [10]; while the other two tools give more general control measures (limited to non-material design measures). OECD [11] did a sensitivity analysis on several CB tools and observed that the CB Nanotool v2.0 did not allow the identification of sensitivity between the individual input parameters of this tool. OECD [12] analysed 3 case studies of consumer exposure to NM powders and concluded that the Stoffenmanager Nano v1.0 obtained a good association rank between predicted values and measured values across products tested in the case studies.

Although CB tools are recommended to be used in Tier 1 of the Tiered approach [1, 4], as a part of the overall risk control strategy to overcome the lack of information and uncertainties related to both NM hazards and exposure, their use is not yet widespread across industries. This may result from the relatively limited evaluation and validation undertaken with CB tools [10].

For Tier 2, exposure measurements took place in the pilot plant of a LightMe partner in Torino (Italy) during 1 day in January 2022 to evaluate the exposure of the workers to the nano-additive powder of Ti-6Al-4V-3.8wt% nTiC, used in the production of a cube with 50 x 20 x 5mm. The monitorization was performed using a portable DiscMini 2.0 from Testo (Miniature Diffusion Size Classifier) to gather quantitative data on the possible releases and emissions of NMs from the DED process and associated tasks (Fig. 1a) following a multi-metric approach, based on the measurement of total particle number concentration and mean particle diameter with a modal diameter in the range of 20-300 nm with 1s time resolution [13].

The relationship between the potential emission sources related with the DED process, the associated tasks, and the background (NMs emission from other sources than the target process) was evaluated through a combined approach using temporal and spatial analysis [1]. Background (BG) monitorization was performed before the process begun at a point close that of the process (near field, NF, \approx 3m) and also far from the work area (far field, FF, \approx 10 m), both inside the building. After activities stopped, a measurement was also performed outside of the building, near the emergency door. A time base of \approx 15 min for BG measurements was followed [1], while measurements during the activities were made for at least 5 min. Fig. 1b highlights the location of the activities, the measurement routes for the background (BG) near and far fields (NF and FF, respectively), and the ventilation systems. Both doors and windows were closed during the monitorization campaign. Temperature, relative humidity, and air flow in the local exhaust ventilation (LEV) were measured in the pilot plant during the monitorization campaign using an anemometer Testo 410-1. In order to avoid any possible contamination no other activities were performed during this monitorization campaign.

The potential exposure of the workers to NMs in terms of total particle number concentration is considered as significant according to the approach recommended by [5] when data fits Eq. (1).

$$\text{Mean concentration during DED process and related tasks} > \text{BG} + 3 * \sigma_{\text{BG}} \quad (1)$$

BG is the mean temporal background concentration (pre-activities) and σ_{BG} is the standard deviation for the background concentration.

Finally, the risk identified in the herein case study can be managed through the recommendation of additional risk control measures, based on the outcome analysis resulting from the application of the three CB tools (Tier

1), the estimation of the workers exposure to airborne NMs (Tier 2), and following the hierarchy of risk controls for NMs [3].

3. Results and discussion

3.1. Initial risk assessment (Tier 1 of the Tiered approach)

Bulk nTiC and the nano-additive Ti-6Al-4V-3.8wt% nTiC are both classified as flammable solid hazard (H228) (Table 1). The information is scarce in terms of morphology, particle size for bulk nTiC, health effects, and exposure limit values (Table 1). Thus, a complete physicochemical and toxicological analysis of the nano-additive powder is required, since it is an innovative nano-product.

Table 1: Hazard identification and some physicochemical properties of bulk NM (nTiC) and nano-additive powder (Ti-6Al-4V-3.8wt% nTiC).

Material	Formula / Ingredients	CAS N°	Appearance	Morphology	Average particle size (nm)	Surface treatment	Hazard	Hazard Pict	Solubility	SVHC	IARC	PBT vPvB	TLV/ STEL (mg/m ³)
Titanium Carbide	TiC	12070-08-5	Gray powder	ND	ND	None	H228: Flammable solid		Insoluble	No	ND	No	TLV(ACGIH) - 10mg/m ³
Titanium / Titanium Carbide	Ti-6Al-4V-3.8 wt% nTiC	Mixture	Powder	ND	35-55	None	H228: Flammable solid		Insoluble	ND	ND	ND	ND

ND - Not Determined

Persistent bioaccumulative and toxic (PBT) substances are therefore harmful chemicals that persist overtime (do not break down easily in the environment) and are especially hazardous for human health and ecosystems

SVHC - Substances of Very High Concern

IARC (International Agency for Research on Cancer) Classification

Group 1 Carcinogenic to humans 120 agents

Group 2A Probably carcinogenic to humans

Group 2B Possibly carcinogenic to humans

Group 3 Not classifiable as to its carcinogenicity to humans

ACGIH classification

Group A1: confirmed human carcinogen

Group A2: suspected human carcinogen

Group A3: confirmed animal carcinogen with unknown relevance to humans

STOT (Specific target organ toxicity) SE (single exposure) RE (repeated exposure)

STEL - Short Time Exposure Limit

The exposure assessment of the two workers involved simultaneously in the DED process and on the related tasks shown in Fig. 1a evidenced that, as an exposure scenario, release and emission of nano-additive powder can occur in all the manual tasks that involve the handling of the powder, such as introducing the nano-additive powder into the powder feeder system or the discharge of the vacuum cleaner filter into the sieving equipment (small to medium energy introduced). Moreover, the opening of the glovebox can also potentially produce airborne NMs. The release source in both DED and sieving activities are contained. The exposure scenario considers a general ventilation system with a hood over the glovebox, and a local exhaust ventilation (LEV) \approx 3m away from the workstations of the powder feeder system and the vacuum cleaner filter discharging. Despite the potential exposure of the workers to inhalation and skin contact to airborne NMs, they use personal protective equipment's, such as respiratory protection, gloves and lab coat.

The application of CB tools for the initial risk assessment (Tier 1) of this case study evidenced that handling activities with the nano-additive powder should be performed inside a glovebox or under a fume hood or a LEV. These tools demonstrated a good agreement of the additional control measures recommended, as in the CB Nanotool v2.0 a risk level of RL2 was obtained, which corresponds to fume hoods or LEV; in the NanoSafer v1.1 β a risk level of very low toxicity and low exposure potential (RL1) was obtained, suggesting the use a fume hood or a LEV; and finally in the Stoffenmanager Nano v1.0, the exposure band 2, which resulted in a risk priority of III (low) due to their combination with an hazard band B, can be reduced to 1 by performing NM handling activities inside a glovebox. The lack of detailed information about the toxicity/health hazard effects of the nano-additive powder used may have affected the risk level/priority obtained, due to the precautionary principle followed by the CB tools [11].

3.2. Exposure measurements (Tier 2 of the Tiered approach)

Worker exposure was estimated based on exposure measurements performed in the pilot plant of the LightMe partner (Tier 2). During the monitorization campaign, the temperature measured was $12 \pm 0.8^\circ\text{C}$, relative humidity was $34.3 \pm 1.2\%$, and the flow rate of the LEV was measured in 1.3 m/s, which according to the Health and Safety Authority [14] is classified as high.

NMs were detected during the background (BG) measurements in the near and far fields (pre-activities) and during the DED process and related tasks (Fig. 2 a and b, respectively), as at least 50% of the particles measured demonstrated a size lower than 100 nm [15]. In the background measurements, the NMs detected do not correspond to the manufactured NMs used during the activities, while in the measurements that were undertaken

during the DED process and related tasks, there is some evidence that the NMs detected correspond to the manufactured NMs used during the activities. To confirm the origin of the NMs it would be necessary to do sample collection for identification and characterization of the NM physico-chemical properties (Tier 3 of the Tiered approach) [1, 4, 5].

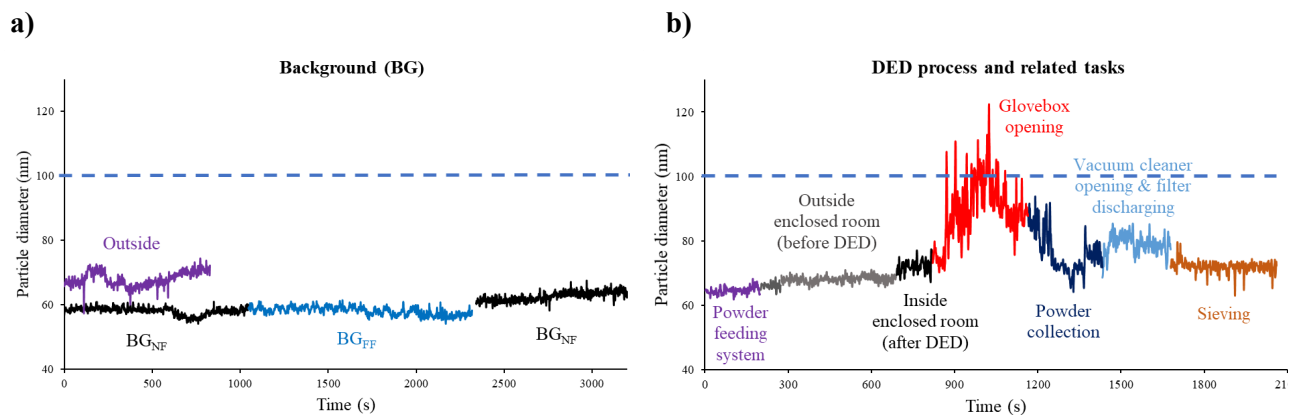


Fig. 2: NMs size: (a) Background measurements in the near and far fields (NF and FF, respectively), and outside of the building, and (b) Measurements during the DED process and related tasks.

The potential of workers exposure during all the activities (except sieving) is considered significant (Fig. 3) based on Eq. (1). The opening of the glovebox seems to be one of the activities that contributes to a significant increase of the NMs concentration (Fig. 3). This might be an indication of a higher pressure inside the glovebox at the instant that it is opened. As recommendation, a pressure gauge should be placed in the glovebox to indicate whether the pressure inside the glovebox is equal to the atmospheric pressure.

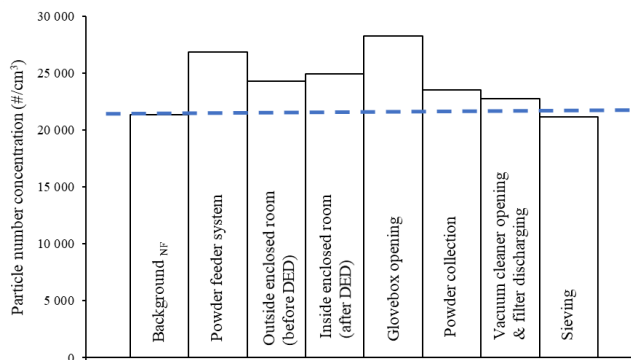


Fig. 3: NMs mean concentration during the DED process and related tasks, and the sum of the mean temporal background and 3 times their standard deviation.

During the powder collection using the ATEX-protected vacuum cleaner, the NMs concentration is lower than that resulting of comparatively with the glovebox opening activity (Fig. 3), however, the potential worker exposure is still classified as significant, based on Eq. (1). The opening and filter discharging of the vacuum cleaner is also classified as significant for worker exposure potential (Fig. 3). Therefore, these activities are recommended to be performed inside a ventilated hood or inside the enclosed room. Moreover, as the enclosed room is equipped with a general ventilation system placed over the glovebox (Fig. 1b), a LEV with a flexible capturing hood could be installed and placed over the glovebox and switched on particularly when opening the glovebox.

4. Conclusion

The implementation of the Tiered approach in the study of this case demonstrated to be a structured and time-effective strategy to assess and manage the occupational exposure risk to airborne NMs in the DED process

and related tasks analysed. Qualitative hazard identification, exposure assessment, and Control Banding tools were used for a preliminary risk assessment (Tier 1), followed by an exposure measurements campaign in the pilot plant (Tier 2). Several recommendations are proposed to be implemented in the DED process and related tasks, such as perform the handling of NMs inside a ventilated hood or inside the enclosed room. A local exhaust ventilation (LEV) with a flexible capturing hood is required which should be placed over the glovebox and switched on particularly when opening it. Additionally, a pressure gauge should be installed in the glovebox to control pressure before opening it, and consequently reduce the potential release of NMs into the working environment. After the implementation of these recommendations, it is advisable to confirm their efficiency by performing another monitorization campaign (Tier 2).

The three control banding tools used demonstrated a good agreement in terms of the additional risk control measures. However, the Stoffenmanager Nano v1.0 seems to cover a wider scope of possibilities and be a more complete tool for occupational risk management. Stoffenmanager Nano v1.0 has the additional advantage to be possible to be used in combination with Licara NanoScan tool, which has a life cycle perspective for assessing the benefits and risks of NMs.

Acknowledgements

This study was developed under the H2020 project LightMe (814552).

References

1. ISO/TR 12885, “Nanotechnologies – Health and safety practices in occupational settings,” ISO/TC 229 Nanotechnologies, 2018.
2. OECD, “Important issues on risk assessment of manufactured nanomaterials,” JT03489003, 2022.
3. P. Schulte, C. Geraci, R. Zumwalde, M. Hoover, and E. Kuempel, “Occupational risk management of engineered nanoparticles,” *Journal of Occupational and Environmental Hygiene*, vol. 5, no. 4, pp. 239-249, 2008.
4. OECD, “Harmonized tiered approach to measure and assess the potential exposure to airborne emissions of engineered nano-objects and their agglomerates and aggregates at workplaces,” JT03378848, 2015.
5. EN 17058, “Workplace exposure – Assessment of exposure by inhalation of nano-objects and their aggregates and agglomerates,” CEN, 2018.
6. M. Molitch-Hou, “Chapter 1: Overview of additive manufacturing process” in *Additive Manufacturing: Materials, Processes, Quantifications and Applications*, J. Xhang and Y. Jung, Ed. Oxford: Elsevier, 2018, pp. 1-38.
7. ISO/TS 12901-1, “Nanotechnologies – Occupational risk management applied to engineered nanomaterials – Part 1: Principles and approaches,” International Organization for Standardization, 2012.
8. A. Falk, C. Schimpel, A. Haase, B. Hazebrouck, C. López, A. Prina-Mello, K. Savolainen, A. Sips, J. Ipina, I. Lynch, C. Charitidies, and Germ, V. (2016). Research roadmap for nanosafety. Part III: Closer to the market (CTTM) [Online]. Available: http://eprints.internano.org/2356/1/CTTM_NSC_Roadmap_final_for_NSC.pdf
9. D. Hristozov, S. Gottardo, E. Semenzin, A. Oomen, P. Bos, W. Peijnenburg, M.v. Tongeren, B. Nowack, N. Hunt, A. Brunerlli, J.J. Scott-Fordsmand, L. Tran, and A. Marcomini, “Frameworks and tools for risk assessment of manufactured nanomaterials,” *Environ. Int.*, vol. 95, pp. 36-53, 2016.
10. K. Dunn, A. Eastlake, M. Story, and E. Kuempel, “Control banding tools for engineered nanoparticles: What the practitioner needs to know,” *Annals of Work Exposures and Health*, vol. 62, no. 3, pp. 362–388, 2018.
11. OECD, “Evaluation of tools and models for assessing occupational and consumer exposure to manufactured nanomaterials – Part I: Compilation of tools/models and analysis for further evaluation,” JT03486023, 2021.
12. OECD, “Evaluation of Tools and Models for Assessing Occupational and Consumer Exposure to Manufactured Nanomaterials – Part III: Performance testing results of tools/models for consumer exposure,” JT03486028, 2021.
13. M. Fierz, C. Houle, P. Steigmeier, and H. Burtscher “Design, calibration, and field performance of a miniature diffusion size classifier,” *Aerosol Science and Technology*, vol. 45, pp. 1-10, 2011.

14. Health and Safety Authority (2014). Local Exhaust Ventilation (LEV) Guidance. [Online]. Available: [hsa.ie/eng/publications_and_forms/publications/occupational_health/local_exhaust_ventilation_lev_guidance.pdf](https://www.hsa.ie/eng/publications_and_forms/publications/occupational_health/local_exhaust_ventilation_lev_guidance.pdf)
15. Commission Recommendation 2011/696/EU of 18 October 2011 on the definition of nanomaterial (OJL 275, 20.10.2011).

The influence of the nanostructured architecture on the optical, electrical and thermal properties of TiN coatings

Ioana Borsan¹, C. Lopes², M.S. Rodrigues², F. Macedo², Camelia Gabor¹, Mihai-Alin Pop¹, Daniel Munteanu¹, Filipe Vaz²

¹Dept. of Material Science, Transylvania University
Brasov, Romania, ioana.borsan@unitbv.ro

²Centre of Physics, Minho University
Braga, Portugal, claudialopes@fisica.uminho.pt

Abstract

In this paper, the influence of the evolution of microstructural and surface features was analysed as a function of the changes in the growing features, namely as a result of the change of the deposition angle. For this, titanium Nitride (TiN) thin films of the same thickness ($2.0 \pm 0.2 \mu\text{m}$) were prepared with different architectures to evaluate the influence of the microstructure geometry on the optical, electrical and thermal response of the films. Two different sets of samples were prepared, the first by varying the flux angle of the sputtered particles ($\alpha = 40^\circ, 60^\circ$ and 80°) and the second by designing 2 periods of zigzag thin films architected using the angles of the first set. A conventional TiN thin film growing in an incidence normal to the substrate was also prepared for comparative purposes. The results left no room for ambiguity about the influence of the growth features on the physical properties of the TiN thin films. The films became darker (low L^* value), less conductive (higher electrical resistivity) and lost the ability to conduct and/or diffuse heat thermal energy (decreased thermal diffusivity) as the inclination of the TiN growth columns increased and rougher surfaces, highly-porous and less-dense microstructures were produced. This work claims the importance of designing materials at the nanoscale, able to meet the most demanding technical, scientific and industrial requirements.

Keywords: Thin Films; GLAD, microstructure; topography; electrical, optical and thermal properties.

1. Introduction

In conventional Physical Vapor Deposition (PVD) techniques, the majority of the prepared films use normal incidence, leading to well-known columnar microstructures, growing normal to the substrate, characterized by very thin and vertically aligned structures, with high compactness. The set of properties obtained is commonly known as having some physical, chemical, mechanical and tribological constraints, namely in terms of surface resistance and chemical integrity, brittleness, ductility and adhesion, together with reduced possibilities in terms of electrical and optical response flexibility [1]. To further extend the coated surface responses, the GLancing Angle Deposition (GLAD) technique has been successfully used to modify the microstructural features of thin films, and indirectly their physical, chemical, mechanical and tribological responses, maintaining the materials' functional properties [2]. Keeping the substrates in motion, the GLAD technique relies on the deposition from a given sputtered particle flux on an oblique angle, allowing to obtain nano-engineering advanced thin film's features with three-dimensionally architected microstructures. By GLAD, the deposition flux arrives with an oblique angle at the substrate surface, an additional variable is introduced in the growth process, which has a significant influence on the development of the film's microstructure and compactness/porosity.

Taking this into account, TiN thin films with microstructures controlled on a nanometric scale have been fabricated using the GLAD approach, revealing a significant change in the overall responses as a function of the particular deposition conditions, namely the change of growing films incidence angles and the architectures designed.

2. Materials and Methods

In the present study, inclined and zigzag-like structures were produced by varying the position of the substrate holder relative to the target. The depositions were performed in a Ar+N₂ plasma, using a homemade magnetron sputtering deposition system. See [2,3] for further details about the deposition equipment,

deposition parameters as well as surface plasma pre-treatment carried out on the substrates before the deposition. The morphological features of the thin films were probed by ultra-high-resolution field-emission Scanning Electron Microscope (SEM). The surface topography/morphology, namely the roughness of the TiN thin films was studied by atomic force microscopy (AFM) using a high-resolution Nano-Observer AFM microscope (Concept Scientific Instruments), in resonant mode with a $5 \times 5 \mu\text{m}^2$ scan size, a resolution of $1024 \times 1024 \text{ px}^2$ and 1 line/s scan speed. The characterization of the film's colour was computed using a commercial MINOLTA CM-2600d portable spectrophotometer (wavelength range 400 to 700 nm), using diffused D65 illumination at a 10° viewing angle. The electrical resistivity of the films was measured at room temperature, using the four-point probe method in a van der Pauw configuration. Modulated IR radiometry (MIRR) has been applied to determine the thermal transport parameters of the thin films [4] affected by the particular morphological features, induced by the architectures of the growing process.

3. Results and discussion

For this work, two series of samples were prepared. For the first one, the inclined set, the substrates were placed at 40° , 60° and 80° relatively to the target, as depicted in Fig. 1a). All samples were prepared with the same deposition parameters (Ar flow of 25 sccm and N_2 flow of 3 sccm). The thickness range of all the samples prepared was about $2.0 \pm 0.2 \mu\text{m}$.

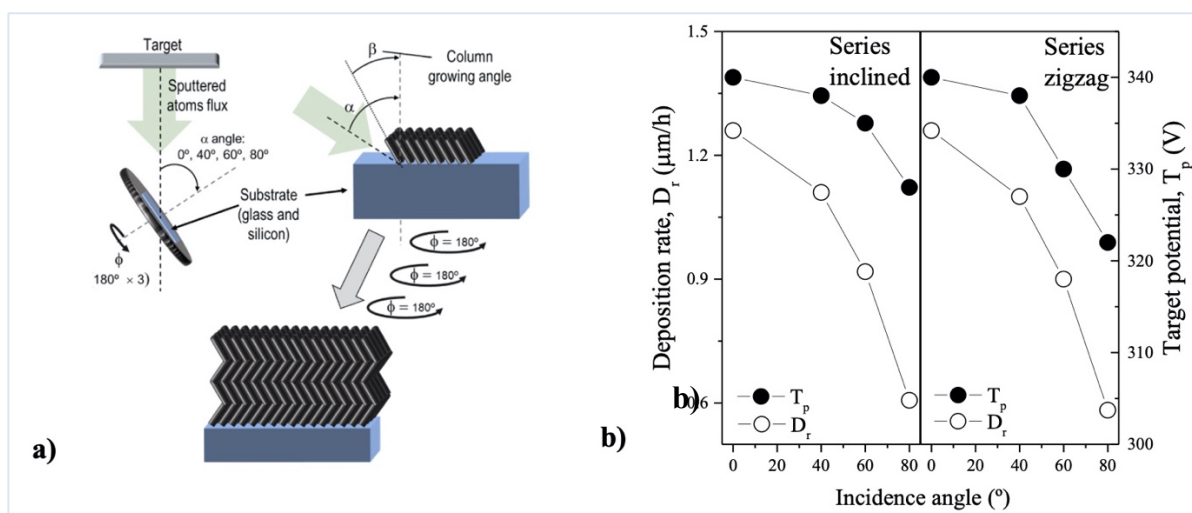


Fig. 1: a) Geometry of the deposition system used in the preparation of the TiN architected thin films; b) Discharge parameters obtained for the prepared samples, namely the target potential (T_p) and the deposition rate (D_r).

In the second set, the zigzag set, the samples were prepared with the same thickness and deposition angles (40° , 60° and 80°) as the previous. For comparison purposes, a sample prepared in conventional mode (0°) was also prepared.

As illustrated in Fig. 1b, there is a significant reduction in the deposition rate for the samples prepared in both series for 60° and 80° . Interestingly, also the correspondent deposition parameter (target potential) reveals such a decreasing trend, which correlates quite well with the reduced flux of sputtered atoms from the target. The inclination of the substrate holder and the consequent decrease of the sample's density (porosity) is certainly the main factor to take into account for this behaviour, as actually observed in the evolution of the microstructural features depicted in Fig. 2. The shadowing effect, together with a less packing of impinging species is also to be taken into account for such a deposition rate reduction. Fig. 2 shows the evolution of the microstructural features of the 2 series of samples.

As illustrated by these figures, the increase of the incidence angle gives rise to interesting features in the deposited samples, namely in what concerns the specific columnar growth. Important to note is the definition of the inclined and zigzag columnar growth itself, which, understandably, becomes more evident.

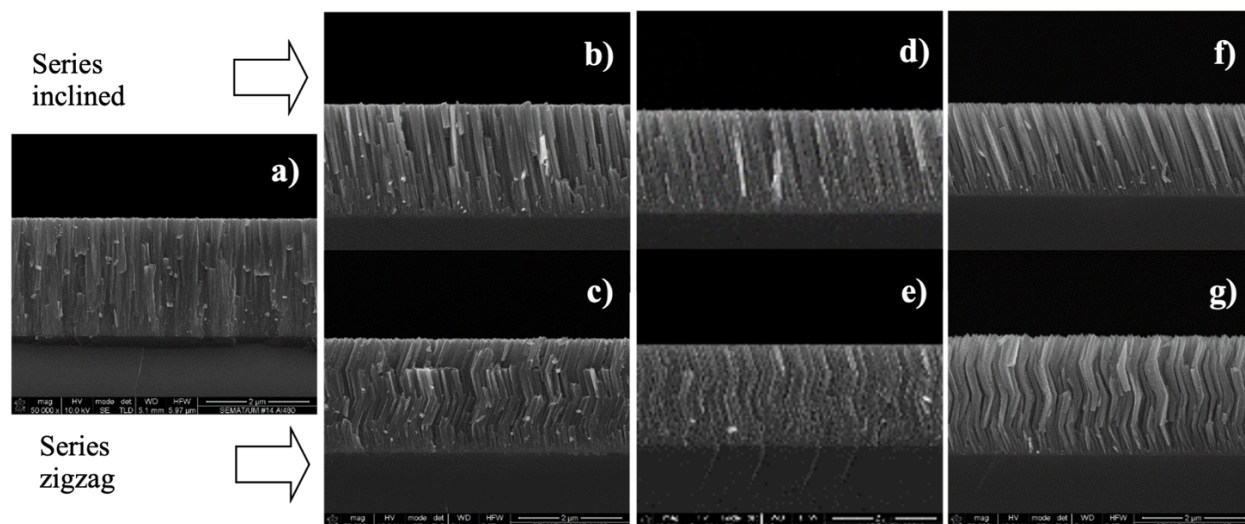


Fig. 2: Cross-section SEM images of the two series of samples: a) reference sample prepared by conventional mode (normal incidence); b) and c) incidence angle of 40° (see Fig. 1b); d) and e) incidence angle of 60°; f) and g) incidence angle of 80°.

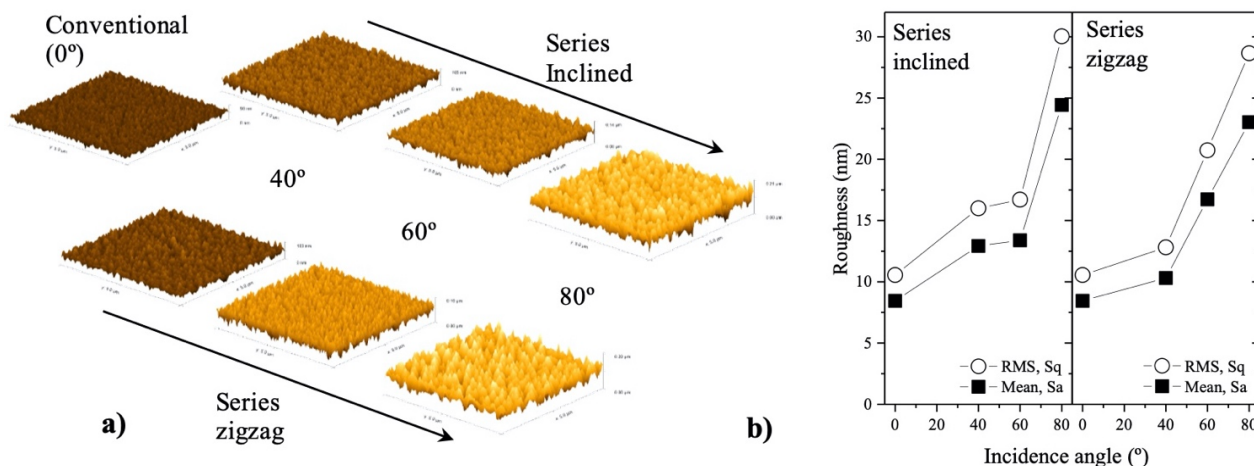


Fig. 3: a) AFM scans of the two series of samples; b) evolution of the surface roughness values in the two series.

The columnar growth's inclination (Fig. 2) and the reduction of the deposition rate (Fig. 1b), resulted in a significant change in the coatings surface characteristics, as evidenced by the AFM scan depicted in Fig. 3, which illustrates the evolution of the surface features for the 2 series of samples prepared.

Again, a significant change in the film's topography is observed, which results in an also significant change in the surface roughness, Fig. 3b). As a consequence of the more porous surfaces and less dense structures (Fig. 2), there is a significant increase in the surface roughness in both series, with values that approximately double for the 60° samples and triple for the 80° ones. Taking into account that all the samples were prepared with the same deposition parameters (flows, thickness, target current), the set of results is presented in Figs. 1 through 3 reveal that it is possible to tailor the microstructure and the surface characteristics of a given coating system just by acting on the type of columnar growth. The tailoring of the surface roughness and the type of columnar growth is extremely important for most technical and industrial applications, namely in the biomedical field for cellular growth enhancement/adhesion, chemical and physical sensing, and mechanical and tribological industrial applications, among several others. Fig. 4 shows the influence of the growing features on the evolution of three of the main physical properties, that were accessed for both sets of thin films.

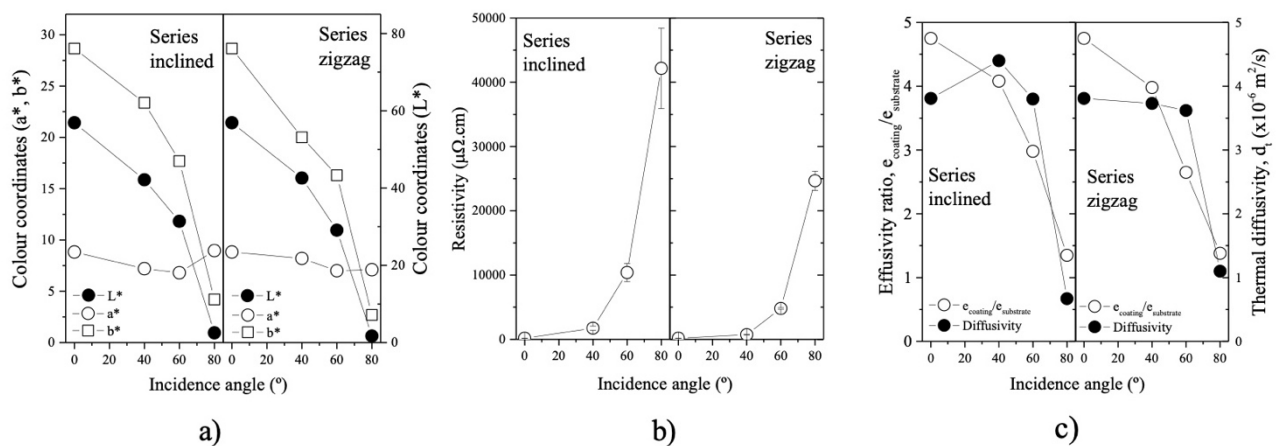


Fig. 4: a) evolution of the colour coordinates; b) resistivity values and; c) thermal properties; of the two series of samples.

As illustrated by the physical properties, there are important changes in the colour coordinates, revealing the significant influence of both microstructural and the correspondent surface features on the evolution of material properties. Particularly noticeable is the evolution of the resistivity, which increases by a factor of more than 100 times when compared to the sample prepared in the conventional mode. The evolution of the thermal properties shows a clear decrease for both configurations, as the incidence angle increases. One can state that the thermal diffusivity as well as thermal effusivity $(k\rho C)^{1/2}$, being k the thermal conductivity and ρC the volumetric heat capacity, are sensitive to the incident deposition angle which changes the capacity of the films to conduct and diffuse heat. For samples prepared at 80° , the results are not conclusive, since the curves obtained clearly deviate from the expected behaviour characteristic of this kind of films [4]. In fact, being the thermal diffusivity a ratio between heat conducted and heat stored by the same material, a decrease in diffusivity (with the increase of the columnar inclination) means that heat is mostly absorbed by the material and a small amount of heat will be conducted further. This could be explained by the increase in the surface roughness and in porosity of the more inclined structures.

Further study is needed to check the existence of any type of threshold above with the thermal diffusion processes in the sample are limited due to the incident deposition angle.

4. Conclusion

The work shows the possibility to tailor the microstructural and surface features of TiN coatings by changing the sputtered flux deposition. The tailoring of these characteristics has been revealed to be an important feature to induce significant changes in the properties of the film, namely optical, electrical and thermal ones.

Acknowledgements

This work was supported by the European Regional Development Fund (ERDF), through the Operational Programme for Competitiveness and Internationalization (COMPETE 2020), under Portugal 2020 in the framework of the NanoStim (POCI-01-0247-FEDER-045908) and NanoID (NORTE-01-0247-FEDER-046985) Projects.

References

1. N. Woo et al., Appl. Phys. A 100 (2010)281–285.
2. A. Ferreira et al., Sensor Actuat. A: Phys. 220 (2014) 204–212.
3. M.S. Rodrigues et al., Appl. Sci. 2021, 11(12), 5388.
4. F Macedo et al., J. Phys. D: Appl. Phys. 45 (2012) 105301.

Bio-Inspired Materials for the Energy Challenge of the Century

Toshiki Tajima ^{1,2,*}, Thierry Massard ^{1,3,4}

¹TAE Technologies, Orange County, USA

²University of California at Irvine UCI, Irvine, USA

³Stanford University, Stanford, USA

⁴Think Composites, France

*corresponding author

Abstract

This work proposes to design and produce a bio-inspired material for the first wall of a transmutation reactor (Transmutator). It will use carbon-based materials since neutrons and hard radiations do not affect the state of carbon materials. The material should be thin enough so all neutrons and gamma rays will go through the material without damaging its structure. Candidate are fibers or mats of Carbon Nanotubes (CNT) or Graphene layers (GL).

An important function to be added to the material is the cooling of the wall. The molten salt FLiBe is at 640°C. The wall could be cooled by a fluid going through the CNT fibers or the Graphene layers by capillarity.

Capillarity effects inside a CNT material has been studied by several teams but none has proved that a flow of CO₂ could be created through the wall by only capillarity process. The analogy of trees pumping the water from the soil to the leaves is invocated here.

In order to create samples of wall materials, 3D nano-printing of CNT embedded into a nano porous media will be performed. The capillarity parameters of the samples will be measured then the samples will undergo series of test in molten salt and under high neutronic flux to insure their durability in service. The final architecture will be then design following the technical requirements of the reactor.

Keywords: Carbon, carbon nano-tubes (CNT), radiation, bio-inspiration, capillary pressure, Carbon cycle

1. Introduction

We are facing the contemporary challenges of the impacts of human activities such as the climate change induced by the increase of CO₂ emission since the Industrial Revolution. The nuclear approaches is a way to remedy this situation, both the fission-based and fusion-based. One of the challenges of fission nuclear path is its radioactive spent nuclear waste that can accumulate for more than the civilizational epoch.[1]

This work is a contribution to the design and realization of carbon-bases bio-inspired material for the wall of a Molten Salt Reactor (MSR) (FLiBe) generally called SMR (Small and Medium Reactor). The goal of the reactor is to eliminate the long-life nuclear elements from the nuclear waste that is the minor actinides. Neutronic transmutation of the spent fuel will reduce the amount of trans-uranium elements in the molten salt.

Radiations in a transmutation reactor can be used to reduce anthropogenic CO₂ gases and thus contribute to close the cycle of carbon in an opportune manner.

2. Bio-inspired Wall

One of the characteristics of the nuclear energies such as fusion (or fission, or the above transmutator) is its highly concentrated power and associated intense radiation (or “temperature”, or “energy” as characterized by MeV, instead of eV or less for the fossil energy or other green energy). Thus while we propitiate and control this high level of energy becomes available in nuclear approaches (fusion or fission at the level characterized by MeV), such high energy becomes a unique tool to treat and bring in additional capabilities such as the concentrated energy conversion route. This means that on one hand, we have to have a first wall that can withstand severe physical and chemical conditions unlike any other than nuclear. On the other hand, we can take advantage of such high level of energy to harness its capabilities in a variety of forms, including chemical energy conversion in addition to heat and electric energy conversion. There are several known chemical paths of energy conversion in the chemical potential from CO₂, such as Haber and Sabatier processes from heat, or more direct photovoltaic processes. Because of the starting point of nuclear energy being at MeV with energies

carried by neutrons, high energy gamma photons and X-rays, low energy photons (optical, infrared, and voltage separation), heat, etc., we have many more paths to navigate ourselves to convert the generated energy into chemical, electrical energies including the conversion of CO₂ via these paths. Perhaps, we can learn from trees that do so, so that we can realize “artificial tree” in the utilization of nuclear energy. This is a path we also learned to create “artificial intelligence” learning from our brains, via bio-inspiration.

2.1. Carbon-based materials

We discuss in particular the case of the first wall of a fusion reactor as a rendition of the “artificial tree” here. A tall sequoia tree can pump water (and other nutrients) high up through the trunk many 10s of meters. This is because the nanofibers and nanotubes of tree veins sustain the capillary effects of the surface tension that pull the water. Inspiration borrowed from a tree goes further. As mentioned in Table 1, carbon based materials are by far better in many aspects of physical and chemical damages by the severe conditions of nuclear reactor, [2], [3]. Our “artificial tree” fibers may be made up of Carbon NanoTubes (CNT). Carbon is hard to transmute by nuclear processes that can be severe on the first wall of fusion reactors or transmutators.

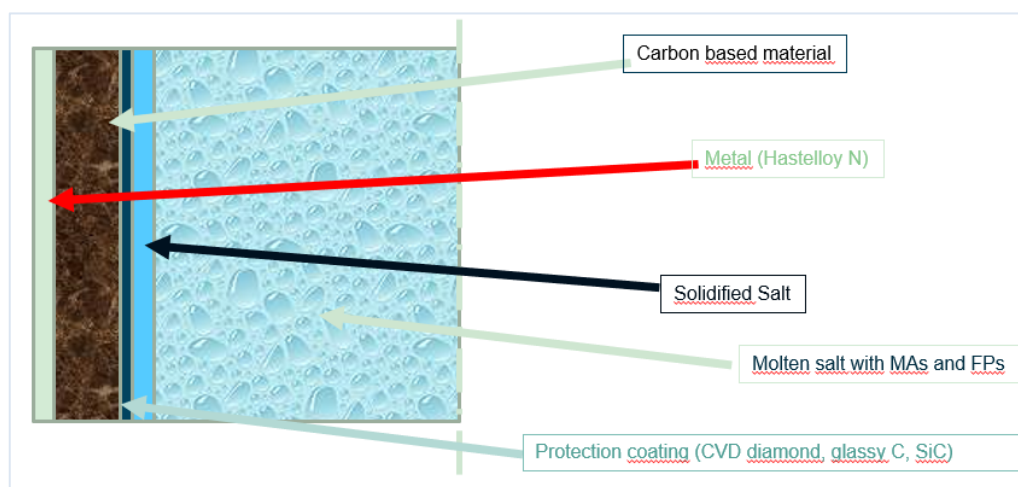


Fig. 1: Preliminary concept for the first wall of the Transmutor

CNT has higher thermal and electric conductivities beyond the best metals. Their tensile strength is also stronger than metals, though they are easy to bend. Their thickness of the tube can be as thin as Angstrom (single layer of benzene carbon layer, i.e. graphene layer) [4].

Combining the extraordinary tensile strength with easy bending of CNT (or grapheme), we could enhance the overall structural strength by combining these materials with framing struts that are harder to bend. Corrosion of the first wall by molten salt can be mitigated using graphene coating. High surface and deposition rate can be achieved using graphene dispersed in water [5]. Carbon Waters in Bordeaux [Chesneau, private comm, 2021], for example, masters the technology of these functionalized graphene layers for corrosion protection.

In a similar manner, we also propose to use carbon nanotubes fabric for a fusion reactor first wall [6].

Materials	Neutron damage [dpa/yr]	Neutron activation [Bq/cm ³]	Corrosion	Physical properties
Stainless Steel 304	1	2.0124 10 ¹¹	53 μm/yr	Hardness =140 kg/mm ² Melting point=1400 C
Inconel 601	0.9	5.2081 10 ¹⁰	> 34 μm/yr	77 kg/mm ² 1400 C
Hastelloy-N	1.2	1.6824 10 ¹¹	8 μm/yr Corr. attacks Cr	60 kg/mm ² 1320 C
Carbon composites	0.12 Maintained structural integrity up to 32 dpa	1.1959 10 ⁹	Extremely low – nm/yr?	2600 kg/mm ² 2700 C
Graphite (reactor grade graphite)	0.0013	1.6358 10 ⁹	No attack by salt 2.5 years of operation	Low < 40 kg/mm ² 3600 C
Diamond	Very low (for detectors) No data for wall, but should be even better!	Only fast neutrons, in reaction $n+^{12}\text{C}\rightarrow\alpha+\text{?Be}$	Extremely chemical inert	see diamond slide

Dimond :chemical stability, low neutron activation and low neutron damage: **Graphite** : many good properties

Table 1: Comparison of materials’ physical and chemical properties in harsh radiative environment of reactors. We compare first three metallic candidates with the latter three carbon-based ones. (refs.)

2.2. Capillary design as part of the cooling of the reactor

Energy producing reactors such as fusion reactor, fission reactors, and transmutators need to have a series of walls to confine the high energy and radiation producing central chamber(s). These walls, in part, can act as a cooling system of the reactor. Traditionally, walls are cooled through pipes with coolant circulated by a pumping system. This pumping system extracts heat and transports it outside of the central region. When the pumping system malfunctions (e.g., due to the lack of electricity), the heat removal stalls. Accordingly, what is realized by the effects of our capillaries is an improved wall design to remove heat without the need of an external power source.

2.3. From nanoscale to final scale

The concept of the wall has to be designed and manufactured at nanoscale since to our knowledge there is no macroscale manufacturing technique for this material.

The method envisaged is to use 3D printing technology at nanoscale. A polymeric thermoplastic binder including the nanotubes will be printed on the carbon/carbon structural material. The extrusion technique will align the NCT in the required direction for the cooling flow [Figure 2]. After completion of the printing the parts will be pyrolysis to remove the binder and form a porous and light Carbon foam. The last layer of Graphene will be deposited as a final protection against corrosion.

In a first step, tiles will be manufactured to assess the feasibility of every step of the manufacturing process. Then a complete characterization campaign will check the chemical compatibility with molten salt, the behaviour under radiations and the mechanical properties of the tile. The capillarity pressure of the nano-tube network will be measured on separate samples.

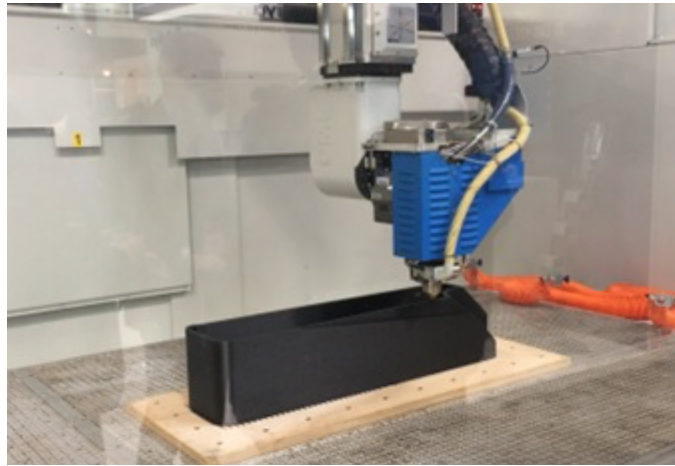


Figure 2 – 3D printing of carbon-composite compound (court. of CMS)

3. Conclusion

The transmutation reactor using molten salt technology is capable of transforming large quantities of minor actinides from the spent fuel and thus able to solve the tough problem of long term burial of nuclear wastes. The technology is at hand. We have shown that the technology for the first wall which is the critical part of the reactor can be proposed. The use of CNT as part of the first wall allow to create a cooling flow by capillarity. It can be used also for the radiolysis of endogenic CO₂ and thus contribute to reduce the global warming.

Acknowledgements

The authors wish to thank TAE technologies for their kind support.

References

1. B. Klaus and P. Horn, *Robot Vision*. Cambridge, MA: MIT Press, 1986
2. Pascal Yvon, David Patrick 2016. *Structural Materials for Generation IV Nuclear Reactors*. Woodhead Publishing.
3. Cress, Cory D, Christopher M Schauerman, Brian J Landi, Scott R Messenger, Ryne P Raffaele, and Robert J Walters. 2010. “Radiation Effects in Single-Walled Carbon Nanotube Papers.” *Journal of Applied Physics* 107 (1): 14316.
4. Shokrieh, M M, and R Rafiee. 2010. “A Review of the Mechanical Properties of Isolated Carbon Nanotubes and Carbon Nanotube Composites.” *Mechanics of Composite Materials* 46 (2): 155–72.
5. Pénicaud, Alain. 2017. “Conductive Graphene Coatings synthesized from graphenide solutions.” *Carbon*, vol 121 – 217-225
6. T. Tajima, A. Necas, T. Massard, and S. Gales, *East meets West again now to Tackle the Global Energy Crises*, to be published in *Uspekhi* (2022).

Electro-Flexure Response of Multi-Functional Natural Fiber Hybrid Composites

Christopher Meninno¹, Vijaya Chalivendra¹, and Yong Kim^{2*}

¹ University of Massachusetts Dartmouth, Department of Mechanical Engineering, Dartmouth, USA

² University of Massachusetts Dartmouth, Department of Bioengineering, Dartmouth, USA

Abstract:

An experimental study was conducted to investigate the electro-flexure response of conductive natural fiber hybrid laminate composites. The composites were composed of laminates of jute and flax fibers, and the composites were subjected to flexural loading for the electrical and bending response. Multi-walled carbon nanotubes were shear mixed and ultrasonicated into the epoxy matrix. Short carbon fibers were reinforced in-between the laminates using "wet flocking" technique. To measure the electrical response under flexural loading, a four-point circumferential probe method was used. A parametric study was conducted to investigate flexural performance and damage sensing by varying carbon fiber lengths (150 and 350 μm) and the carbon fiber densities (500, 1 000, 1 500, and 2000 fibers/ mm^2). The addition of carbon fibers decreased the flexural strength for most of the cases, however increased the flexural strain at break for all composites of carbon fiber length of 150 μm . During the nonlinear deformation, the composites of carbon fiber length of 150 μm demonstrated a linear increase in resistance; however, that of carbon fiber length of 350 μm showed increasing slope of resistance. Overall, the composites of carbon fiber length of 350 μm showed lower resistance change at break compared to that of carbon fiber length of 150 μm .

Keywords: Hybrid natural fiber composite, electro-flocking, multi-functional, damage detection, flexural strength

1. Introduction

Natural fiber composites (NFCs) have gained attention due to the advantages the NFCs have over traditional materials. The most notable advantages were ease of production, reduced cost of materials, and sustainability. They are beneficial to reduce pollutant emissions, greenhouse gas emissions, and overall reducing the carbon footprint in production.[1] NFCs also offer benefits such as higher durability, lighter weight, as well as fire and corrosion resistance.[2] They offer a reduction in density compared to glass fibers but maintain comparable specific properties. The mechanical properties are enhanced by incorporating fillers and fibers to accommodate for high strength needs. [3] A drawback of NFCs is the water absorption of these cellulose contained natural fibers. Chemical treatments are applied to the natural fibers to reduce their water absorptivity, namely alkaine and silane treatments.

A recent study examined the electro-bending behavior of curved jute/epoxy resin laminated composites reinforced with MWCNTs and short carbon fibers. Using a pre-crack in a curved specimen, the major crack did not propagate; instead, lateral cracks formed around the crack tip in the tension zone which led to fracture in the composite. The carbon fibers productively diverted the main crack's growth. [4]

2. Experimental

2.1. Materials

Woven linen flax fabrics (Joann Fabrics, North Dartmouth, MA); Woven jute fabrics (Stuart C. Hurlbert & Co. Inc, Framingham, MA) used without any modification for hybrid laminated composites. For the matrix resin system, Epothin 2 epoxy resin (bisphenol-A epoxy resin) and Epothin 2 epoxy hardener from Buehler, Lake Bluff, IL The ratio of resin to hardener is 100:45 parts by weight. MWCNTs (Cheap Tubes Inc., Cambridgeport, VT) with a length of 1-12 μm , a diameter of 13-18nm, and a purity greater than 95% were used along with carbon flock fibers to create an electrical network in the composites. Two weight percentages of CNTs were introduced into the epoxy of the composite matrix, those being 0.1% for composites with CF reinforcement and 0.3% for composites without carbon fibers. PAN-based

carbon fibers were used for z-axis reinforcement between the jute and linen laminates. Short 150 ± 50 μm length carbon fibers (Asbury Graphite Mills, Inc., NJ), and longer 350 ± 100 μm length carbon fibers (E&L Enterprises Inc., LA.) Both carbon fibers had a mass density of 1.8g/cc with 99% carbon content. Highly conductive silver paint from SPI Supplies, West Chester, PA was used to paint a four circumferential probe system onto the composites. (ASTM D3846) for electro-flexural resistance measurement.

2.2. Composite Fabrication

Fabrics and CNT mixture: The jute and flax fabrics were cut into 229 x 178mm² sheets to provide adequate space to fabricate the desired size of the composites. Then, the jute and flax fabrics underwent a fiber treatment to achieve hydrophobic effect for preventing moisture absorption to have a longer service life of the composites. To accomplish this, the fabrics were given an alkali treatment, followed by a silane treatment. The process and its effectiveness have been well documented in the recent work. After these treatments, the fabrics were stored in sealed zip-lock bags to ensure they were not exposed to moisture and other outside factors that may have affected the fabrics.

Since agglomeration is a major issue when CNTs are introduced into epoxy, a homogeneous dispersion is achieved by combining shear mixing and ultrasonication. The desired amount of CNTs is added to epoxy into mixing container and hand mixed for initial dispersion. The mixing container was placed in an ice bath to maintain a low temperature to avoid decomposition of the epoxy resin. Then, the mixture was shear mixed using a shear mixer (IKA RW 16 basic overhead stirrer) at 600 r/min and ultrasonicated (Cole Parmer CP 750) using a pulse mode of 4 s on and 10s off. The shear mixer provided macro dispersion of the CNTs, while the ultrasonicator provided microdispersion of the CNTs. Once the mixture was mixed for 1h, the mixture is degassed in a vacuum chamber to remove trapped air bubbles.

Electro-flocking and Laminar Composites: Once the mixture was fully degassed, one-fourth of the mixture was poured into a separate mixing container. It was weighed, and hardener was added using the 100:45 ratio of resin to hardener by weight. This portion of the epoxy was used in the University of Massachusetts Dartmouth's patented "wet flocking" process. This process is shown in Figure 1. The CNTs embedded epoxy mix was used to coat the laminates which were taped onto a metal plate. This metal electrode plate was placed in a flocking chamber with the laminates facing down. On the bottom plate, the carbon fibers were evenly spread through sifting. After these two plates were positioned properly, a high voltage difference (30-80 kV) was induced between the conductive plates. Due to the contact charging of the carbon fibers, they align perpendicular to the epoxy-coated laminates and rise to the laminates where they remained embedded in the epoxy. This process is completed for four of the five laminates to provide z-axis carbon fiber reinforcement between all laminates. Nearly 40% of the carbon fibers were aligned vertically on the laminates as a result. Standard vacuum infusion process was employed using two layers of flax fabric and three layers of jute fabric stacked. The remaining CNTs embedded epoxy mix was infused into the mold. The mold was left for 24h to cure at room temperature.

The specification of prepared laminar composites are shown in Table 1.

Electro-Flexural Testing: Flexural testing and electrical response of three point bending carried out according to ASTM D790-17. The flexural loading (3 point-bending) is employed on an Instron® universal testing machine with a load cell capacity of 50 kN. Displacement rate varies from 2.0 mm/min to 2.5mm/min. Real-time tests are captured using a MicroCapture® Pro digital micro scope. Bluebill® software for the Instron® testing machine is used to capture the load and displacement data. The four circumferential probe system was used to measure specimen electrical resistance under load. The outer ring probes were used to supply a constant current source through the specimen. This DC current was supplied by a Keithley 6620 current source. The inner ring probes were used to measure the voltage across the zone of interest (in the center where damage occurs) in the composite. Electrometer (Keithley 6514) and connect to each probe for two volt- age measurements. A Keithley 2000 multimeter was used to measure the differential voltage between the elec-trometer measurements. LabVIEW was used to

record and capture the voltage data. Before testing the samples, insulating tape was applied to the loading noses to ensure no current leakage into the loading fixture. The initial resistance of composites was calculated using Ohm's law.

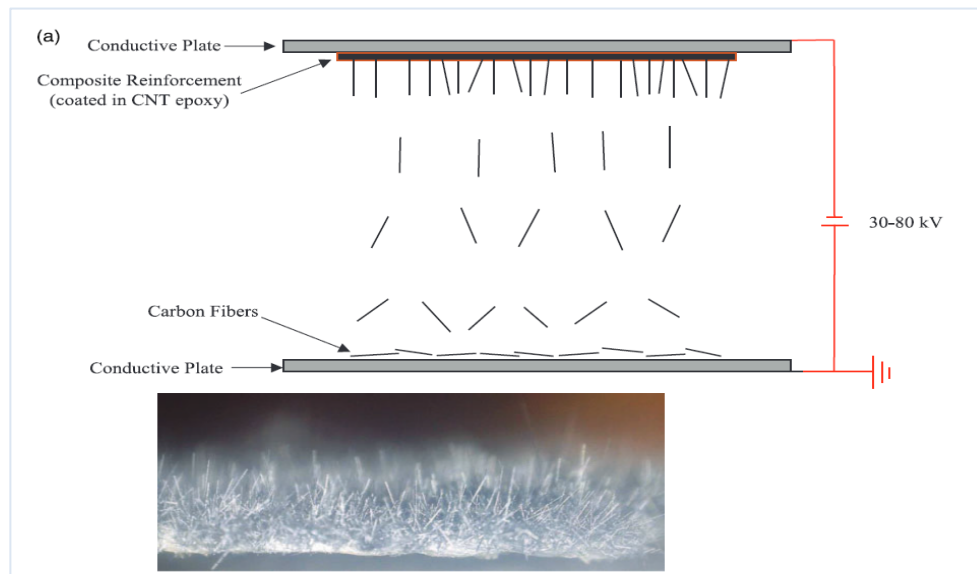


Figure I. (a) The schematic representing the electro-flocking process and (b) an optical photograph of floccled linen fabric with 350 μm carbon fibers with a density of 1000 fibers/ mm^2 .

Table I. The experimental parameters, composite names, thickness values, and weight percentages of each composite constituent.

Carbon fiber length (μm)	Carbon fiber density (fibers/ mm^2)	Composite name	Thickness (mm)	% Weight of jute fabric	% Weight of flax fabric	% Weight of carbon fibers
0	0	FS-0-0	4.40 ± 0.07	24.278 ± 0.498	8.605 ± 0.177	—
150	500	FS-150-05	4.36 ± 0.05	26.356 ± 0.381	9.341 ± 0.135	0.165 ± 0.002
	1000	FS-150-10	4.36 ± 0.05	26.031 ± 0.274	9.226 ± 0.097	0.325 ± 0.003
	1500	FS-150-15	4.43 ± 0.05	25.016 ± 0.422	8.866 ± 0.164	0.469 ± 0.008
	2000	FS-150-20	4.53 ± 0.07	22.372 ± 0.156	7.930 ± 0.058	0.559 ± 0.004
350	500	FS-350-05	4.63 ± 0.01	24.191 ± 0.213	8.574 ± 0.083	0.350 ± 0.003
	1000	FS-350-10	5.13 ± 0.05	22.981 ± 0.220	8.145 ± 0.078	0.665 ± 0.006
	1500	FS-350-15	6.25 ± 0.02	20.641 ± 0.401	7.316 ± 0.142	0.896 ± 0.017
	2000	FS-350-20	6.16 ± 0.06	18.712 ± 0.205	6.632 ± 0.073	1.083 ± 0.012

3. Results and Discussion

Flexural force-displacement diagrams: Figure 2 shows the summary of the Flexural force-displacement diagrams. It can be observed that: Upon reaching the peak load the load dropped instantaneously for all composite types (catastrophic failure); The initial slope of force displacement diagrams of all composite types was similar to that of FS-0-0 (without carbon fibers); For the FS-150-XX series, only FS-150-20 resulted in a higher slope value for most of the force-displacement curve compared FS-0-0. As for the FS-350-XX series, every composite type resulted in higher slope values than FS-0-0. The shorter carbon fibers were not as effective at stiffening the composites as the longer carbon fibers were. The maximum carbon fiber density, 2000 fibers/ mm^2 , is required to increase stiffness of the composite for the 150 μm carbon fiber reinforcement. This is because the shorter carbon fibers do not take up as much space as the 350 μm carbon fibers, requiring a higher carbon fiber density to obtain the same results as the FS-350-XX composites. Every composite type aside from FS-350--05 resulted in an increase in displacement at break in comparison with FS-0-0. This is because the addition of carbon fibers effectively blocks crack growth in the composite and deflects the damage to allow for greater displacements before break.

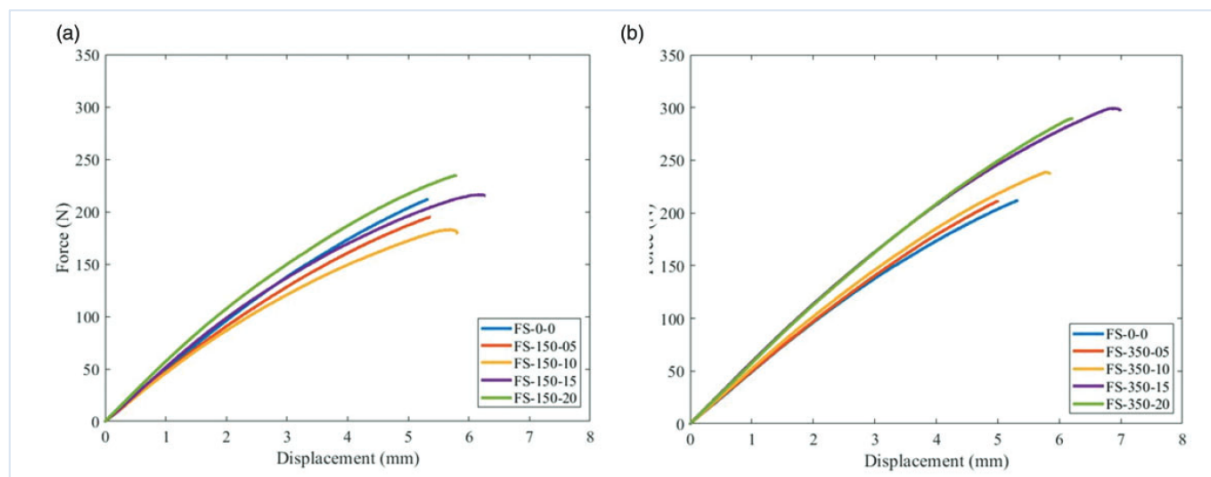


Figure 2. The characteristic force-displacement curves for: (a) FS-150-XX series and (b) FS-350-XX series

Initial resistance of composite series (no loading): The composite with no carbon fiber reinforcement (FS-0--0) shows the highest resistance (6×10^{10} Ohm) in Figure 3.

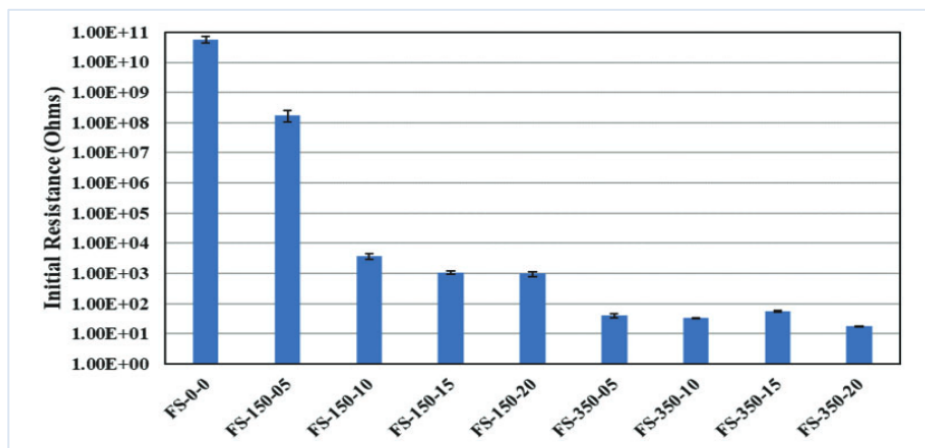


Figure 3. The initial resistance of all composite specimen types.

It can be observed from Fig 3 that: The series with 150 μ m carbon fiber reinforcement (FS-150-XX) decreased in initial resistance with increasing carbon fiber density. The FS-150--05 had an initial resistance that is about 320 times lower than FS-0--0. This is because the addition of carbon fiber reinforcement created a better electrical network within the composite. The carbon fibers interacted with surrounding CNTs in the matrix resin to create electrical connections. FS-150-10 had an initial resistance that was around 47,000 times lower than FS-150--05. This effect also resulted in a decreased resistance for FS-150-15 and FS-150-20. The FS-350-XX series had substantially lower initial resistance values than the FS-150-XX series. FS-350-10 had an initial resistance that is about 110 times lower than FS-150-10.

FS-150-XX Electrical Response under Flexural Loading:

Figure 4 shows the Electrical resistance change in FS-150XX. It can be observed that: Zone-I is represented by the onset of changing electrical network within the composites. The resistance in this zone increased with a steadily increasing slope. As a result of the bending, the tension below the neutral surface separated CNTs from carbon fibers and from each other, which removed electrical connections between them. In the compression zone above the neutral surface, the CNTs and carbon fibers moved closer, creating more electrical connections above the neutral surface. The connections below the

neutral surface were being removed faster than those being created above it. This resulted in a net positive change in resistance. This continued until the end of zone-1.

Zone-II begins when microcracks began forming due to the carbon fibers creating stress concentrations and debonding from the matrix resin. This results in a mostly linear increase in resistance. The micro cracks contributed to the removal of electrical connections among carbon fibers and CNTs by cracking the matrix between them. This became the dominant form of resistance change, which caused the change in resistance to be large and steady. The removal of connections continued until a large crack propagated in the outer jute layer of the composite. Due to the addition of carbon fibers and the low density of the jute fabric, there was a large fraction of epoxy in the composite which caused the composite to be brittle. As soon as the crack propagated in the outer layer of jute, it quickly broke the composite. The overall change in resistance decreased from FS-150-05 to FS-150-10. This is because with increasing carbon fiber density, the addition of carbon fibers created more electrical connections within the composite, improving its electrical network. This reduced the composites initial resistance and required more connections to be removed from the network to create a similar.

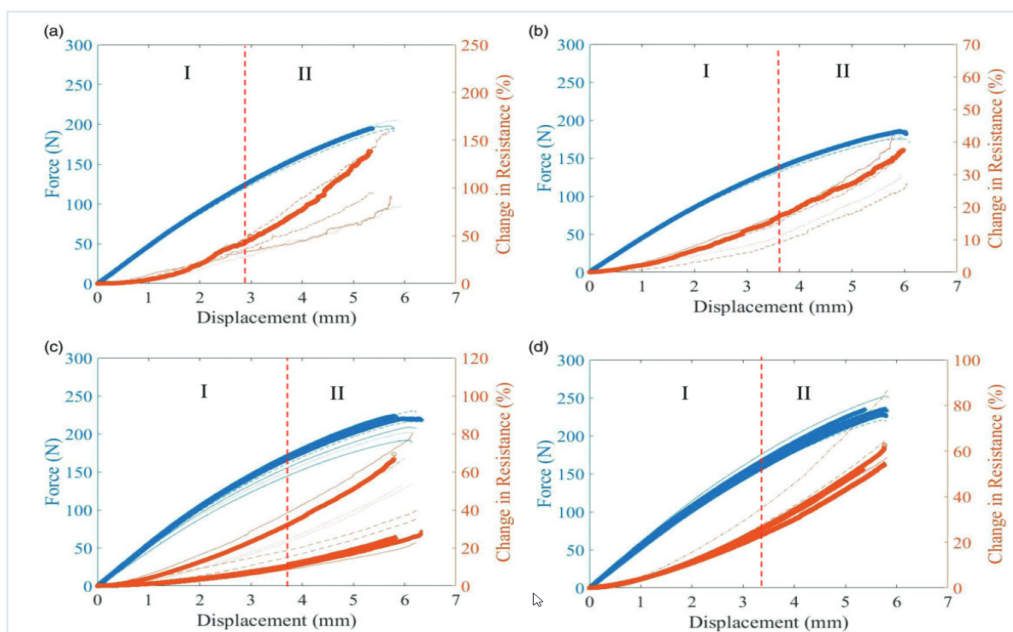


Figure 4. The flexural /electrical response of: (a) FS-150-05, (b) FS-150-10, (c) FS-150-15, and (d) FS-150-20.

Flexural Electrical Response of FS-350-XX series:

Figure 5 shows electrical resistance changes of FS350-XX under flexure loading. It can be observed that: For Zone-I, the electrical response varied based on the carbon fiber density of the composites. For FS-350-05, this zone was linearly increasing. This was due to the lowest carbon fiber density having the weakest electrical network. When connections were removed during elastic deformation, it was consistent because there were not as many connections as higher carbon fiber densities.

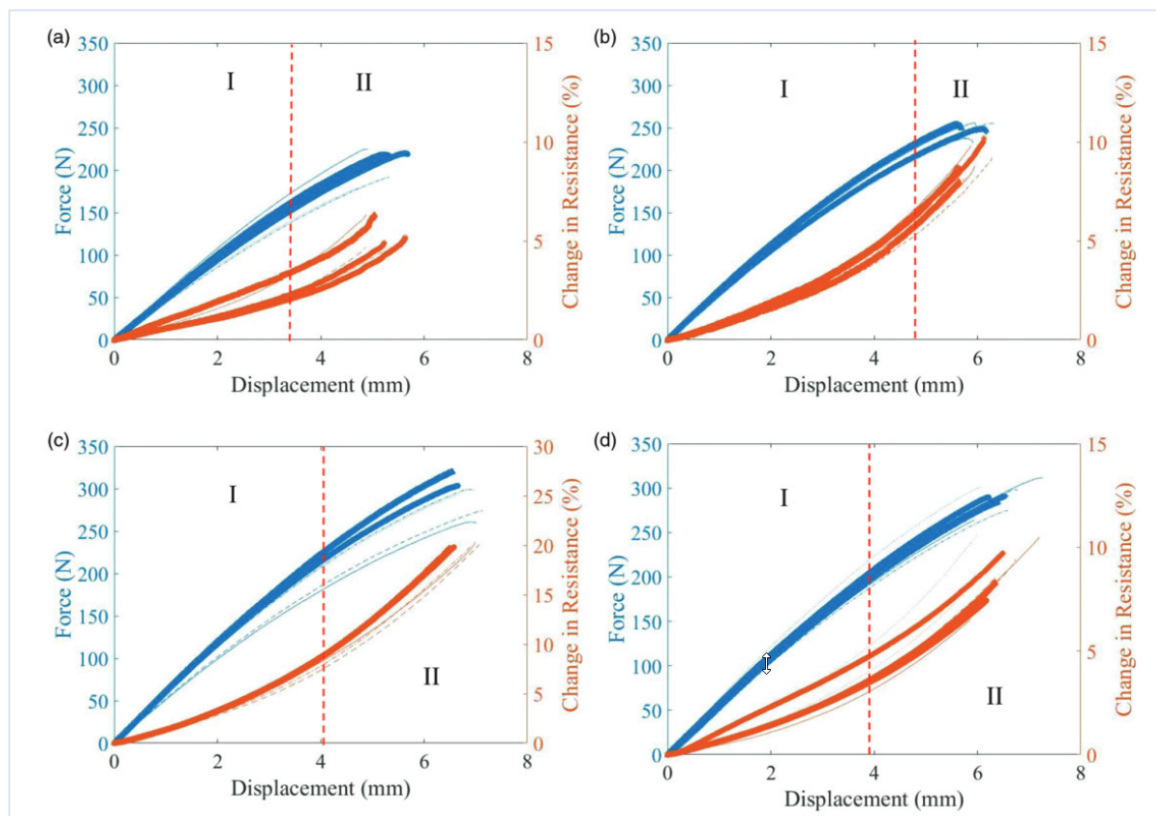


Figure 5. The flexural and electrical response of: (a) FS-350-05, (b) FS-350-10, (c) FS-350-15, and (d) FS-350-20.

This gradual removal of connections in an already weak electrical network created a linear change in resistance. For FS-350-10, FS-350-15, and FS-350-20, Zone-I was widening with an increasing slope, like Zone-I in the FS-150-XX series. This was because of the increased amount of carbon fibers. With more carbon fibers, more electrical connections were created among carbon fibers and CNTs, and the longer carbon fibers created even more electrical connections because the 350 μ m long carbon fibers penetrated better into the laminates. The longer carbon fibers created more electrical connections among CNTs and make it more difficult to remove the connections. Zone-2 continues with a trend similar to zone-I, this being an increasing slope of resistance. The longer fibers had larger surface areas, creating larger zones of weak bonding and stress concentration. Thus, when the microcracks began to form, there were more and larger cracks than in the FS-150-XX series. This effect removed more electrical contacts. The percent change in resistance was overall lower in the FS-350-XX series compared to that of the FS-150-XX series. For example, FS-150--05 and FS-350--05 had significant differences in electrical responses. At the onset of microcracks, the percent change in resistance of FS-150--05 was 15 times greater than FS-350--05.

4. Conclusions

The addition of carbon fibers reduced flexural strength in most cases, aside from FS-150-20 and FS-350-15. The fibers did not bond well with the epoxy, which caused stress concentrations throughout the composite, resulting in a weakened composite.

Adding carbon fibers to composites increased the flexural strain at break for all samples in the FS-150-XX series and decreased for all samples in the FS-350-XX series. However, all composite with carbon fiber reinforcement aside from FS-350-05 resulted in greater displacement at break. This is due to the fibers blocking microcrack growth to allow for greater deflection of the composite before it fails. The addition of carbon fibers also increased the thickness of the composite causing a decrease in flexural strain.

Carbon fiber reinforcement greatly reduced the initial electrical resistance of the composites in comparison to FS-0-0. The FS-350-XX series resulted in lower initial resistances than the FS-150-XX series due to the longer carbon fibers penetrating better into the composite laminates, having more electrical connections and creating a thorough electrical network.

Each composite exhibited two zones of electrical response, with Zone-I referring to elastic deformation and Zone-II corresponding to onset and growth of microcracks. The beginning of microcrack growth resulted in a linear slope in change of resistance for the FS-150-XX series, whereas it increased the slope of change in resistance for the FS-350-XX series.

For the FS-150-XX series, increasing carbon fiber density resulted in decreasing ΔR values for increasing carbon fiber densities. The decrease is contributed to increasing carbon fiber density creating better electrical networks. When the electrical network of a composite is improved, it requires more connections to be broken to create the same change in resistance as other composites.

The FS-350-XX series results in similar ΔR values due to the initial resistances of the composites being so close. This is contributed to the longer carbon fiber creating a better electrical network. The 1500 carbon fiber density experienced the largest ΔR due to the inconsistency of carbon fiber.

Acknowledgement

The author(s) sincerely express their gratitude to the students and staff members in UMass Dartmouth Composites Materials Lab. This study was supported by the National Science Foundation (NSF) of the United States of America under grant number CMMI-1563040.

References

1. Joshi SV, Drzal LT, Mohanty AK, et al. Are natural fiber composites environmentally superior to glass fiber reinforced composites? *Compos Part A: Appl Sci Manuf* 2004; 35: 371-376.
2. Ticoalu A, Aravinthan T and Cardona F. A review of current development in natural fiber composites for structural and infrastructure applications. In: Southern region engineering conference, Toowoomba, Australia, 11-12 November 2010.
3. Saheb DN and Jog JP. Natural fiber polymer composites: a review. *Adv Polym Technol* 1999; 18: 351-363.
4. Yang S, Meninno C, Chalivendra V, et al. Electro-bending behavior of curved natural fiber laminated composites. *Compos Struct* 2020; 238: 1-8.

Synthesis of PLGA, PCL and its Nano-Fabrication for the Tissue Engineering Application by using Electrospinning and Melt Pining Technique

Savita H Bansode^{1,*}, Prakash A Mahanwar²

¹ Ph.D. Scholar, Department of Polymer & Surface Engineering, Institute of Chemical Technology, Mumbai, Maharashtra, India – 400019 ; savita.ictmumbai@gmail.com

² Professor, Department of Polymer & Surface Engineering, Institute of Chemical Technology, Mumbai, Maharashtra, India – 400019 ; pa.mahanawar@ictmumbai.edu.in

* Correspondence: savita.ictmumbai@gmail.com; 9921763333, INDIA.

Abstract

Poly(lactic glycolic acid) PLGA and PCL is most important polymer in biomedical applications the degradation of kinetics modified by co-polymerization ratio of monomer. In this interest Biodegradable and biocompatible polymers are use in controlled drug delivery systems, in the form of implants devices for skin bone, and dental repairs, Microwave irradiation on as a heating source for polymerization reactions is a rapidly growing branch in polymer science current research shows both the microwave and heating synthesis is efficient alternative which takes less time for polymerization. With microwave synthesis polycondensation, free and controlled radical polymerization, and ring opening polymerization (ROP) can be done. The characterization of Polycaprolactone was done by Fourier Transform Infrared Spectrophotometer (FT-IR), scanning electron microscopy (SEM), the polymer interactions were checked by Differential scanning calorimetric (DSC) and the XRD analysis was carried out to determine structural changes PLGA/PCL nanofabrication done by electrospinning Technique for biomedical applications. PLGA synthesis done by convectional method, with study of various parameter such as time, temperature, monomer and catalyst ration. Input monomers and the reaction products are analyzed here. Important characteristics, melting temperature, glass transition temperature, thermal stability, chemical composition and the ratio of the monomers in the synthesized and copolymer, were obtained from these analyses. These results helped to infer the absence of residual monomers in the synthesized copolymers PCL done by microwave assisted method.. The PLGA micro particles are one of the most successful new drug delivery systems (DDS) in labs and clinics. Because of good biocompatibility and biodegradability, they can be used in various areas, such as long-term release systems and the tissue engineering.

Keywords: Biocompatible, Biodegradable, Electrospinning, Melt spinning, Polymerization, Synthesis, PLGA PCL, Nanofabrication.

1. Introduction

Tissue engineering, is the field which applies knowledge of life science and the principles of engineering towards the developing, maintaining or improving damaged tissue functions of human being(1). Tissue engineering can act as a substitute for the extracellular matrix (ECM) and provide a substrate for cellular adhesion and organization (2, 3). Thus, tissue engineering scaffolds should have a strong resemblance to the natural ECM, which is comprised of nanometer-diameter protein fibers, due to lack of donor and immune repulsion between receptors and donor, development is done in tissue engineering field (4, 5). In the tissue engineering, scaffold synthesis by using bio-degradable electrospun nanofiber and then implanted in defective part of the patient (6, 7). The scaffold plays most important role in tissue engineering. Cell grows on scaffold; it acts as supportive membrane for cell growth. (8, 9). There are different methods for nanofabrication: Self-assembly, phase separation, electrospinning and melt blowing. Electrospinning is one of the best method for polymer nanofabrication has been studied in details (10, 11). In addition to this, an ideal scaffold should possess the following characteristics: i) biocompatible and biodegradable, ii) highly porous structure, iii) suitable mechanical strength and iv) a proper surface topography.

99,10) Three types of fibrous polymeric materials are mainly used for this purpose viz. naturally occurring polymers, synthetic biodegradable, and synthetic non-biodegradable polymers. (12, 13)The tissues or organs that can be repaired with the help of scaffolds include skin, cartilage, bone, nerve, ligaments, muscles, kidney, liver, heart, pancreas, esophagus, etc. [14,15].

2. Electrospinning

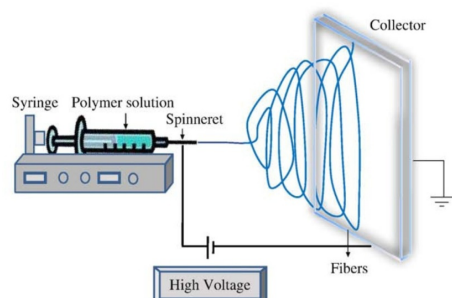


Figure 1: Electrospinning Setup

The electrospinning device consists of three main components: i) syringe pump, ii) collector and iii) high voltage supply. A schematic representation of the process is presented in Figure 1. The method comprises of following steps: i) the polymer of which the nanofibers have to be produced is dissolved in solvents; ii) the solution of the dissolved polymer is inserted into a syringe; iii) the tip of the syringe needle is connected to a high-voltage power supply; and iv) fibers are collected on the appropriate collector. Because of the particular design mentioned above and represented in Figure 1, the solution acquires a charge when it is ejected through the needle tip (Taylor cone), which causes it to gravitate toward the collector (15, 16, 17). The collector is grounded, or fixed in place, and acts as the template for the fibers to attach. Figure 1: Schematic representation of electrospinning In this method, the formation of nanofibers depends on several parameters (18,19) such as solution properties, (20,21) controlled variables, (22,23) and ambient parameters (24,25). Solution properties affecting the process consist of viscosity, conductivity, surface tension, polymer molecular weight, dipole moment, and dielectric constant. Controlled variables include the flow rate of the solution, electric potential, gap between tip and collector, geometry of collector, and diameter of pipette orifice (26,27). Ambient parameters include solution temperature, humidity, etc. The effect of these parameters on the electrospun fiber. (28, 29)

3. Melt spinning

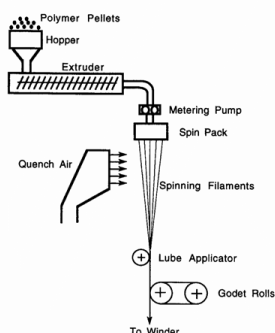


Figure 2: Melt spinning Setup

Melt spinning has a simple setup where fibres from a molten polymer can directly be drawn continuously, avoiding the use of solvents. The fibres, however, cannot be made in a nano-scale using melt spinning and the technique is not suitable to those polymers e.g., PCL which are susceptible to degrade under melt spinning conditions. (28, 29)

The temperature of spinning and the rpm of take-up roll were kept constant at 110 °C and 900 rpm, respectively. The fibres were air cooled before they wind up on the take-up roll.

Melt electrospinning is an alternative to solution electrospinning, however, melt electrospinning has typically resulted in fibres with diameters of tens of microns.

Melt electrospinning requires cooling of the polymeric jet, while solution electrospinning relies on evaporation of the solvent to produce fibres (30).

4. Materials and methods

4.1. PLGA Synthesis

4.1.1. Materials

Lactic acid 90% pure was purchased from Loba chemie, used as monomer. 97% pure Glycolic acid was purchased from Sigma Aldrich, as monomer. Stannous Octoate 99% pure was purchased from Sigma Aldrich and used as initiator and catalyst (it acts as both). Stearyl alcohol and Lauryl alcohol (reagent grade) from SD Fine Chemicals Pvt. Ltd used as co-catalyst. Silicon oil used in thermocouple pocket.

4.1.2. Apparatus:

Heating mantle, Overhead stirrer, stirring rod with Teflon blade, Vacuum setup, Nitrogen balloon, oil tube, thermometer, Temperature sensor, Thermocouple, thermometer pocket, four necked round bottom flask, nitrogen (gas) purging tube, Weigh machine, beakers, conical flask, pipette, water condenser, separating funnel, vacuum adaptor, stand, clamp, rubber bulk, join and bends, connector, stopper, Nitrogen balloon stand (ring clamp), fiber resistance fabric, Petri dish, Funnel, Spatulas, Glass stirring rod, Buchner funnel, wood blocks, rubber tube, etc., **Fig.1: PLGA synthesis setup**

4.2. Procedure:

The experimental set up is as shown in Figure-3 with nitrogen purging provision. The rate of agitation maintained during reaction was 500 RPM the contents were heated slowly up to 130°C and then vacuum was applied so as to avoid removal of monomer along with water of reaction during oligomerisation. The vacuum used was through cold trap. After complete setup is ready lactic acid added in the reactor and heated for 15 min till 60°C then add glycolic acid. Lactic acid added before glycolic acid because glycolic acid has higher reactivity compare to lactic acid. After complete addition of required quantity of glycolic acid the contents were heated at 60°C for 1 hour and after oligomerisation required quantity of stannous octoate and Stearyl alcohol/ lauryl alcohol (co-initiator) was added. After complete addition of initiator, co-initiator contents were heated to 130°C and maintained at 130°C for 1 hour and then vacuum is applied. The progress of reaction is monitored by determining acid value. Final acid value and saponification value of product was determined and reaction stopped when acid value of the reaction product reached below 10 mg of KOH/gm of sample.

PLGA purification

4.2.1. Vacuum drying: Synthesized product PLGA was dissolved in chloroform/ acetone, and dried in vacuum at 46°C and 55°C. After it keep for cooling.

4.2.2. by using Desiccator: The product PLGA was cooled down and then dissolved in chloroform and subsequently precipitated into diethyl ether. The precipitated mixture was collected in petri dish and dried in desiccator using vacuum. Vacuum applied by vacuum pump.

4.2.3. Büchner funnel: The polymer PLGA was purified by first dissolving in chloroform followed by precipitating in methanol under the action of mechanical stirring. And the precipitate dry using Büchner funnel in which vacuum is applied to the arm.

4.3. Melt Spinning

4.3.1 Apparatus: Melt spinning instrument, PLGA

4.3.2. Procedure: PLGA was dried in oven for 40 min. to remove moisture from polymer. About 200 grams of material PLGA used for fabrication process. Material was added to the spinneret in molten form. Optimized RPM (1200-1500) and Temperature (100-140°C) according to requirements. Polymer material is added through hopper, material was melted in single screw extruder where heating plates are attached. Material will pass to the spinneret which attached with high-speed rotatory motor. PLGA melted in barrel then it passes through the nozzle to spinneret which rotate at high RPM. **Figure. 2:** Centrifugal melt spinning setup and Figure 3 Spinneret setup with heater and spinneret respectively.

Characterization of PLGA and fibers:

Fourier Transform Infrared (FTIR): The infrared absorption spectra were collected at 20°C from 4000 - 650 cm^{-1} . The spectra were recorded on a Bruker spectrometer operating in the ATR (Attenuated Total Reflectance) mode.

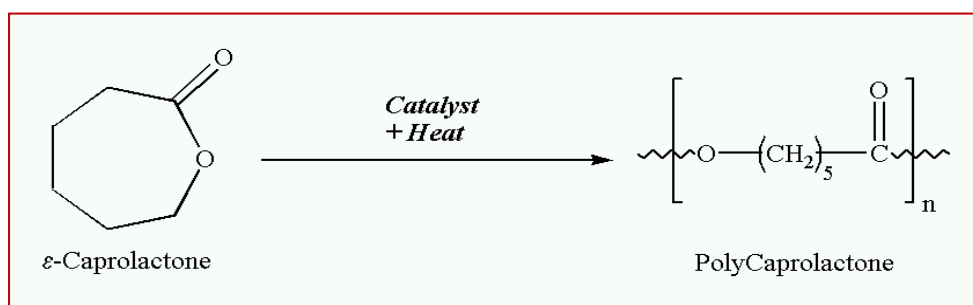
Nuclear Magnetic Resonance (NMR): NMR samples have been prepared by dissolving the copolymers in CDCl_3 from Aldrich containing TMS at 0.05%. ^1H spectra were obtained at 400 MHz. Measurement has been performed at 300 K on a Bruker spectrometer. TMS was used as internal reference.

Differential Scanning Calorimetry (DSC): The DSC equipment used, TQ instruments DCS Q100, was programmed to first heat the samples from room temperature -10°C to 200°C at a rate of 10°C/min. An unsealed aluminum sample vessel was used with nitrogen as the carrier gas at a flow rate of 20 mL/min. The mass of the analyzed sample varied from 5 to 10 mg. The DSC curve was the reference for determining the glass transition temperature (T_g) and phase transition temperature (T_m).

Thermogravimetry (TGA): TG analysis was carried out to measure change in mass with increase in temperature, thermal stability, and maximum degradation temperature for the samples. The test was conducted at a heating rate of 10°C/min from 20°C to 500°C in an unsealed sample vessel under nitrogen atmosphere with a flow rate of 20 mL/min. The equipment used was a PerkinElmer Pyris 1. The mass of the analyzed samples varied between 5 and 10mg.

Optical microscopy: Fiber diameter determined by using Olympus BX41 microscope with lens power of 20x and 50x.

5. PCL Synthesis



Microwave method is used for the synthesis of Poly (ϵ -caprolactone). ϵ -caprolactone (Sigma Aldrich, India) was used as a monomer and stannous octoate (Sigma Aldrich, India) was used as a catalyst. Microwave synthesis of Poly (ϵ -caprolactone) was done by adding calculated amount of catalyst to 5 mL monomer solution in Tetrahydrofuran as a solvent (THF, Sigma Aldrich, India).

5.1. Procedure:

At a fixed catalyst loading of 0.01 g, the effect of wattage and temperature were studied on the synthesis of Polycaprolactone (PCL) with a reaction time of 15 min. The results of the above experiments are shown in following figure. It was observed that by increasing the temperature the % yield of PCL increases till a particular temperature and the further increase in the temperature results in decreased yield. With 100 W and 150 C, the % yield of synthesis was observed to be 80%. Further increase in the reaction temperature from 150 till 190 C increased the yield from 80% to 86%. However, further

increase in the temperature from 190 C to 230 C decreased the yield from 86% to 78%. It is also observed that the effect of temperature on the synthesis remained same for any wattage value. It is observed the increasing wattage from 100 - 300 W improved the synthesis and higher yield values were obtained with a corresponding increase in wattage. However, at higher wattage values such as 400 W, the % yield reduced significantly. Therefore, from the above studies temperature of 190 C and wattage of 300 W are considered as optimum reaction conditions. For a fixed wattage of 300 W and at a reaction temperature of 190 C, the effect of reaction time in the range of 5 min - 20 min was studied on the synthesis. It was observed when the solution was kept for 5 min and 10 min reaction time, there was no product formed. At 15 min the % yield was observed to be 90 %. When the reaction time was further increased to 20 min, % yield was 98%. Figure 2 having The effect of various parameters on the synthesis of Polycaprolactone was studied. Following are the range of parameters selected for the study.

6. Result and Discussion

Table 1 PLGA polymer fiber morphology Optimized parameter of PLGA

Monomer ratio (60:40) mol/mol	Lactic acid = 7.5 g Glycolic acid = 1.9 g
Sn (Oct)₂ (1.00%) wt.%	0.087 gm
Lauryl alcohol (0.8%) wt.%	0.052 gm
Time	25 h
Temperature	130°C
Acid value of lactic acid	561.00 mg of KOH/ g of sample
Acid value of glycolic acid	728.81 mg of KOH/ g of sample
Acid value at start	563.50 mg of KOH/ g of sample
Acid value after 25 H	96 mg of KOH/ g of sample
Yield	89%

Table 1: Different parameters of Polycaprolactone was studied. Following are the range of parameters selected for the study.

Serial No.	Temperature	Wattage (W)	Catalyst concentration (g)
1	120	300	0.01
2	150	300	0.01
3	190	300	0.01
4	200	300	0.01

Table 2: Effect of reaction temperature and wattage

Serial No.	Reaction time (min)	Wattage (W)	Catalyst concentration (g)
1	5	300	0.01
2	10	300	0.01
3	15	300	0.01
4	20	300	0.01

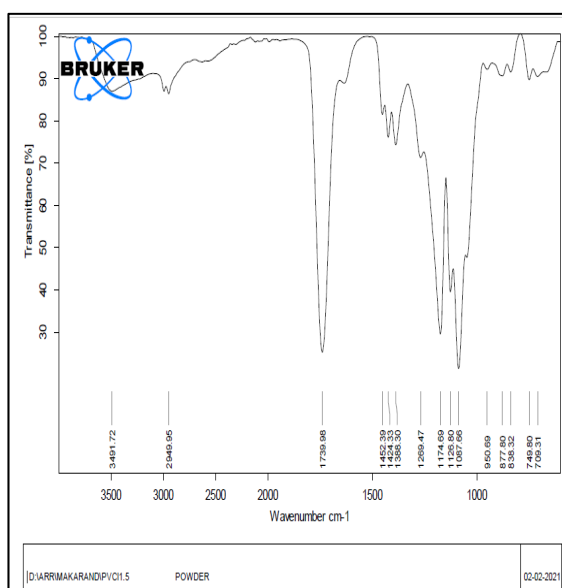


Figure.3: FTIR spectra for PLGA 60:40

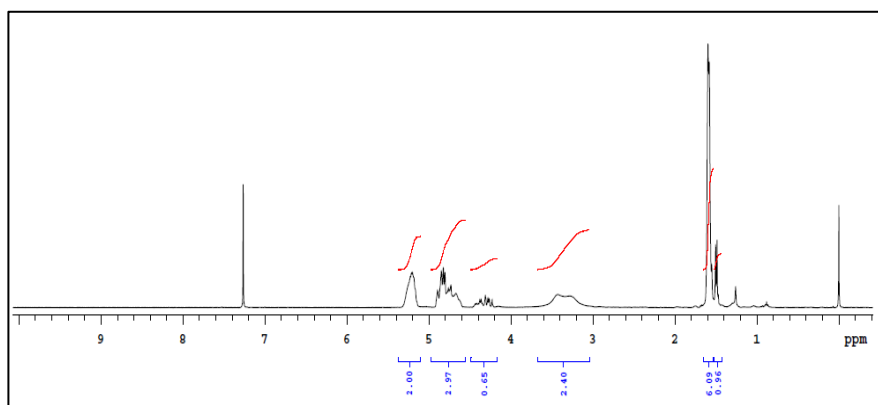


Figure 4: ^1H NMR spectrum of PLGA 60:40

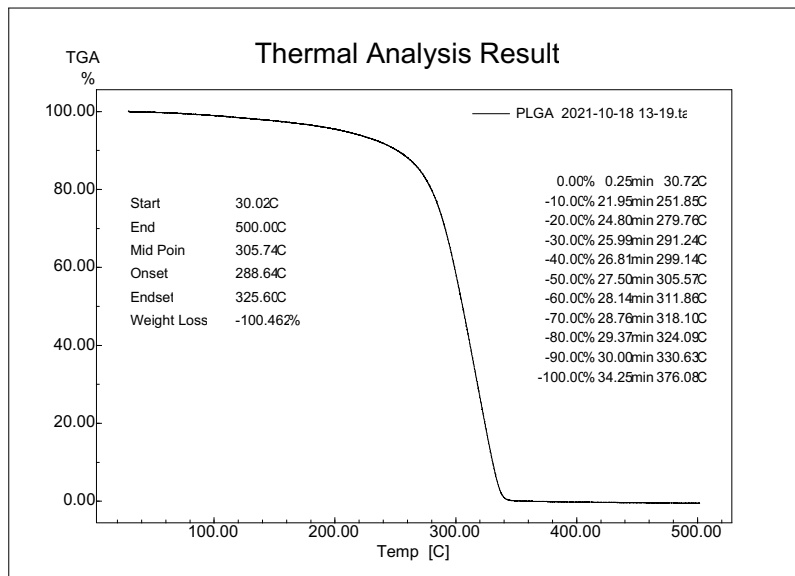


Figure.5: TGA curve of PLGA 60:40 heating from 30 to 500°C.

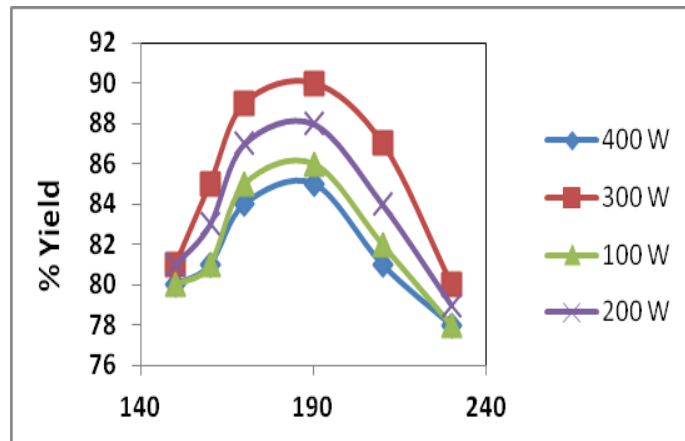


Figure 6: Effect of reaction time for PLGA:

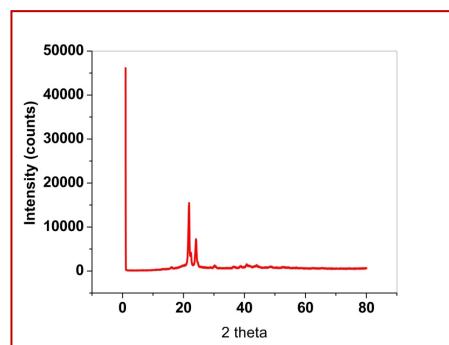


Figure 7: X-Ray diffraction (XRD) Of PCL

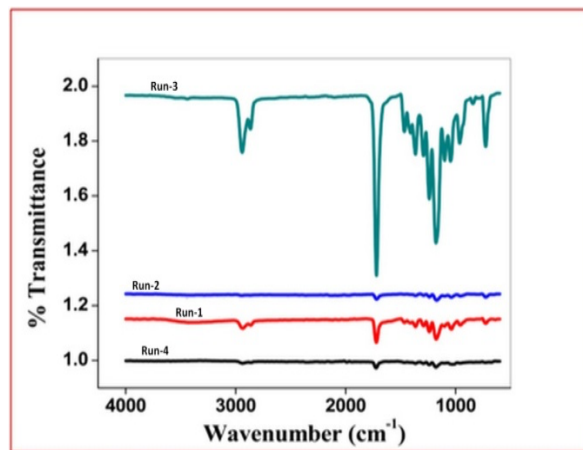


Figure 8 : Fourier Transform Infrared Spectrometry Of PCL

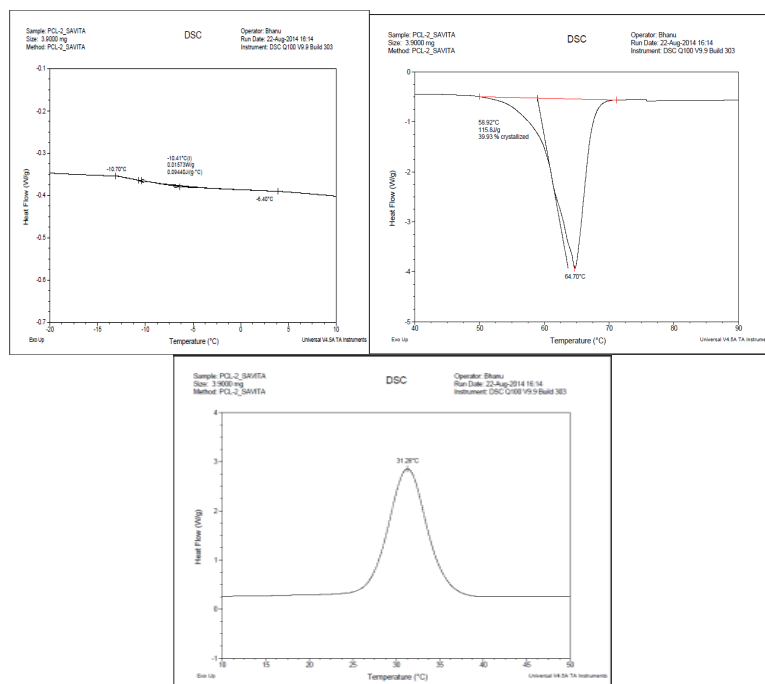


Figure 9: (a, b, c): Differential scanning calorimetry

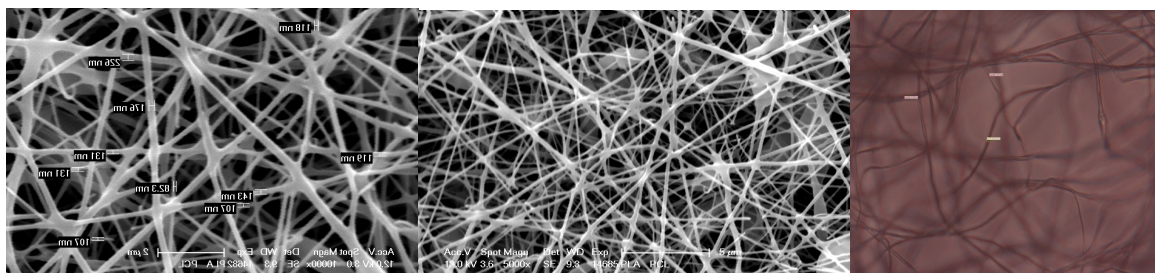


Figure 10: a, b, c: PCL Scanning Electron Microscopy (SEM), Confocal image of Nano Fibers

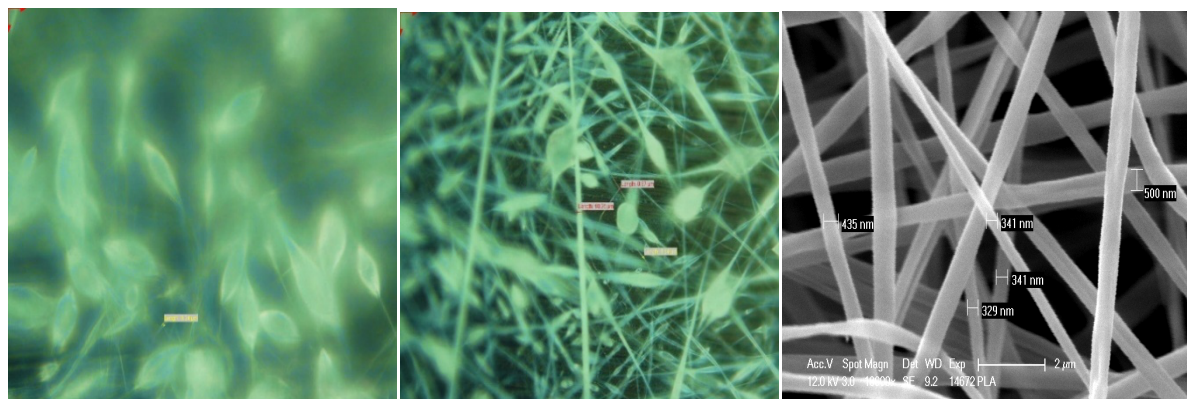


Figure 11: PLGA nanofibers by using electrospinning technique for 5, 10, 15, 20% confocal images and scanning electrospinning microscopy images.

7. Conclusion

PLGA polymers good in delivery carriers for controlled administration of drugs, peptides and proteins due to their biocompatibility and biodegradability. In general, longer-term release requirement. Also, for very long-term release (more than six months), semi-crystalline polymer with a high degree of crystallinity can be considered. Furthermore, multiple studies demonstrate that PLGA can easily be formulated into the drug carrying devices at all scales. Electrospinning is a very simple, versatile and economic technique with many of the advantage for the fabrication of scaffolds for biomedical applications. Electrospinning has shown itself as a promising technology for the production of nanofibers which finds a great potential for its application in the biomedical field in tissue engineering.

Acknowledgments

I am very thankful to UGC financially supported and Institute of chemical Technology and CIRCIOT for providing Facility.

References

1. Nandana Bhardwaj, Subhas C. Kundu, Electrospinning: A fascinating fiber fabrication technique, *Biomaterial Journal*, 2020.
2. R. Langer and J. P. Vacanti, "Tissue engineering," *Science*, 1993.
3. Brahathee swaran Dhandayuthapani, Yasuhiko Yoshida, Toru Maekawa, and D. Sakthi Kumar, Polymeric scaffold in tissue engineering application: A review, 2011.
4. R. m. Nerem, tissue engineering in the USA, medical and biological engineering and computing, 1992.
5. K.M. Kim and G.R.D. Evans, Tissue engineering: the future of steam cell, 2009.
6. Valts A, Tolly NS, et.al. Scaffolds and biomaterials for tissue engineering: a review of clinical applications, 2003.
7. Whitaker MJ, Quirk RA, Howdle SM, Shakesheff KM, Growth factor release from tissue engineering scaffolds, 2001.
8. Naughton GK, from lab bench to market: critical issues in tissue engineering, 2002.
9. B. P. Chan, K. W. Leong, Scaffolding in tissue engineering: general approaches and tissue specific conditions, 2018.
10. Vats A, Tolly NS, Polak JM, Buttery LD, Stem cells: sources and applications, 2015.
11. Gupta et al., Biomaterial and scaffold for tissue engineering, 2005.
12. Berger J, Reist M, Mayer JM et.al, Structure and interactions in cavallntly and ionically cross-linked chitosan hydrogels for biomedical applications, 2017.
13. Jacqueline M. Morais, Fotios Papadimitra kopoulos, and Diane J. Burgess, Biomaterials/Tissue Interactions: Possible Solutions to Overcome Foreign Body Response, 2016.
14. BN Brown, JE Valentin, AM Stewart-Akers, GP McCabe, SF Badylak, Macrophage phenotype and remodeling outcomes in response to biologic scaffolds with and without a cellular component, 2016.
15. Hutmacher DW et.al, Scaffolds in tissue engineering bone and cartilage, 2021.
16. Discher DE, Janmey P, Wang YL, Tissue cells feel and respond to the stiffness of their substrate, 2014.
17. [Edward A. Phelps](#), [Natalia Landázuri](#), [Peter M. Thulé](#), [W. Robert Taylor](#), and Andrés J. García, Bioartificial matrices for therapeutic vascularization, 2018.

18. I V Yannas, E Lee, D P Orgill, E M Skrabut, and G F Murphy, Synthesis and characterization of a model extracellular matrix that induces partial regeneration of adult mammalian skin, 2019.
19. Ciara M Murphy¹ and Fergal J O'Brien, Understanding the effect of mean pore size on cell activity in collagen-glycosaminoglycan scaffolds, 2015.
20. Park et al., Membrane useful as synthetic skin, US patent 4060081, 2008.
21. Cui et al., Design of an artificial skin I. Basic design principles, *Journal of Biomedical Materials Research*, vol. 14, no. 1, pp. 65–81, 2007.
22. S. Ramakrishna, J. Mayer, E. Wintermantel, and K.W. Leong, Biomedical applications of polymer-composite materials: a review, *Composites Science and Technology*, vol. 61, no. 9, pp. 1189–1224, 2001.
23. Zong et al. Electrospun three-dimensional hyaluronic acid nanofibrous scaffolds, *Biomaterials*, vol. 27, no. 20, pp. 3782–3792, 2006.
24. B. D. Boyan, C. H. Lohmann, J. Romero, and Z. Schwartz, Bone and cartilage tissue engineering, *Clinics in Plastic Surgery*, vol. 26, no. 4, pp. 629–645, 1999.
25. Lee et.al. Biodegradable polymers as biomaterials, *Progress in Polymer Science*, vol. 32, no. 8-9, pp. 762–798, 2003.
26. P. Gunatillake, R. Mayadunne, and R. Adhikari, Recent developments in biodegradable synthetic polymers, *Biotechnology Annual Review*, vol. 12, pp. 301–347, 2006.
27. I. V. Yannas, J. F. Burke, C. Huang, and P. L. Gordon, Suppression of in vivo degradability and of immunogenicity of collagen by reaction with glycosaminoglycans, *Polymer Preprints*, vol. 16, pp. 209–214, 1975.
28. P. B. Malafaya, T. C. Santos, M. van Griensven, and R. L. Reis, Morphology, mechanical characterization and in vivo neo-vascularization of chitosan particle aggregated scaffolds architectures, *Biomaterials*, vol. 29, no. 29, pp. 3914–3926, 2008.
29. J. Guan, K. L. Fujimoto, M. S. Sacks, and W. R. Wagner, Preparation and characterization of highly porous, biodegradable polyurethane scaffolds for soft tissue applications, *Biomaterials*, vol. 26, no. 18, pp. 3961–3971, 2005.
30. Thompson et al., scaffold for tissue regeneration: the need to engineer a tissue analogue, *Biomaterials*, vol. 28, no. 34, pp. 5093–5099, 2007.

Reiterative usage of bi-layered nanocrystalline carbon-doped TiO₂ and Ni particles for the photocatalytic water treatment

Martynas Lelis¹, Marius Urbonavicius¹, Sarunas Varnagiris¹, Simona Tuckute¹, Emilija Demikyte¹

¹ Lithuanian Energy Institute, Breslaujos st. 3, Kaunas, Lithuania, rastine@lei.lt

Abstract

Photocatalytic water treatment is considered as one of the most promising environmentally friendly technologies which could be used for the decontamination of both organic and inorganic pollutants. Up to now, in laboratory tests arguably the best photocatalytic treatment results (both under UV and visible light irradiation) were obtained using various modifications of nanocrystalline TiO₂ powder photocatalyst. But conventional fine nanocrystalline powders are inconvenient to handle and most often are hard to recover for reiterative usage. To overcome these limitations, current study was dedicated for the formation of microscopic photocatalytically active TiO₂ particles (powder) and their functionality enhancement by addition of ferromagnetic properties. It was expected that such particles will have sufficient response to the magnetic field which will be applied for the particle handling (stirring, collection, etc.). To realise the concept, ferromagnetic photocatalyst particles were produced in two steps. First, successive magnetron sputter deposition was used to form nanocrystalline Ni and carbon-doped TiO₂ layers on soluble salt grains. Second, salt grains were dissolved in water and bi-layered photocatalyst particles were washed-off. XRD, SEM and XPS techniques confirmed that obtained particles had metallic Ni layer on one side, and carbon-doped nanocrystalline TiO₂ on the other side. In photocatalytic dye bleaching tests fresh bi-layered photocatalyst particles showed moderate efficiency and in 3 h reduced methylene blue dye concentration by approximately 50 %. Powder response to the magnetic field was significant and after treatment approximately 95 % of initial powder were recovered for the reiterative use. Unfortunately, despite relatively high recovery rate, during ten consecutive photocatalytic treatment tests using the same powder set, dye bleaching efficiency eventually decreased by 60 %.

Keywords: TiO₂, photocatalysis, magnetic photocatalyst, magnetron sputtering, photo-catalytic bleaching.

1. Introduction

Photocatalytic water treatment is considered as one of the most promising environmentally friendly technologies which could be used for the decontamination of organic and inorganic pollutants [1]. Up to now, arguably the best photocatalytic treatment results (with both UV and visible light irradiation) were obtained using various modifications of nanocrystalline TiO₂ powder [2]. Unfortunately, fine photocatalyst powder are hard to handle and are not convenient for the reiterative use [3], [4].

Probably the most popular solution to this problem is to immobilise nanocrystalline photocatalyst powder/particles on macroscopic substrates [5]. Relatively large substrate size allows to manipulate photocatalysts by conventional methods. However, this approach is not perfect and comes with its own drawbacks. For example, most often reliable immobilisation of nanocrystalline powders requires relatively deep powder embedment into support, which translates into significantly reduced active area. Moreover, with macroscopic support elements it is more difficult to distribute photocatalyst material evenly throughout the whole volume of treated media.

One of the most appealing alternatives to powder immobilisation is to form magnetic photocatalyst particles and to handle them by the magnetic field. At first, this approach was realised by using wet methods to cover up magnetic cores (for example fine magnetite) with TiO₂ based photocatalyst shells [6]. But TiO₂ crystallisation typically requires calcination at 400-500 °C, which is harmful for the magnetic core. To overcome this limitation, various alternatives for the magnetic photocatalyst materials (both magnetic core and photocatalytic shell) and their synthesis methods have been suggested and provided positive results [7].

The application of the magnetron sputtering (MS) method for powder production is not typical and up to our knowledge it has never been used for the synthesis of magnetic photocatalyst. Nevertheless, magnetic powder synthesis by MS has already been demonstrated at [8], whereas its suitability for the formation of various heterostructures and photocatalysts is undisputable. Accordingly, in current study we explore the possibility to produce magnetic photocatalyst powder by MS technique. More specifically, successive MS deposition was used to form nanocrystalline Ni and carbon-doped TiO₂ (C-doped TiO₂) layers on soluble salt grains which were dissolved in water. The washed-off bi-layered photocatalyst particles (consisting of Ni layer on one side, and carbon-doped TiO₂ on the other side) were thoroughly studied to determine their structure as well as to estimate their photocatalytic activity and long-term stability.

2. Methodology

Synthesis of magnetic photocatalyst particles was realised following four step procedure: i) MS deposition of Ni on K₂SO₄ grains; ii) reactive MS deposition of C-doped TiO₂ on pre-coated salt grains; iii) dissolution of K₂SO₄ grains; and iv) washing-off and drying of final bi-layered powder product consisting of jointed C-doped TiO₂ and Ni layers. Ni layer was deposited by 76 mm diameter circular unbalanced magnetron (300W DC) in Ar gas atmosphere (0.6 Pa). Specific conditions of C-doped TiO₂ deposition (400 W pulsed DC, Ar:O₂ gas supply ratio 4:1, total pressure 0.6 Pa) were preselected by preceding experiments focusing on the obtainment of nearly black highly crystalline TiO₂ films similar to the ones reported at [9].

Washed-off bi-layered C-doped TiO₂ and Ni (further abbreviated as C-TiO₂+Ni) particles we characterised by XRD (Bruker D8), XPS (PHI Versaprobe 5000), SEM (Hitachi S-3400N) and EDS (Bruker Quad 5040) techniques. Magnetic photocatalyst powder stability and suitability for the repetitive treatment was estimated by cycled bleaching of Methylene Blue (MB) solution (10 ml, 10 mg/L, 22 °C) under UV light (Thorlabs M365LP1-C5, 23.5 mW/cm²). In total ten photocatalytic treatment cycles (3 hours per cycle) with one 50 mg set of C-TiO₂+Ni particles were performed. Prior to each treatment, dye solution with a test sample was magnetically stirred (700 rpm) in the dark for 30 min to establish a MB adsorption-desorption equilibrium. During the experiment, at every 30 minutes 0.5 ml samples were taken from the container and measured by UV-VIS spectrometer (Jasco V-650) to determine the remaining dye concentration. After measurement MB samples were returned to the container. Between cycles magnetic photocatalyst particles were collected by magnetic stirring bar and used MB solution was replaced by the fresh one. Photocatalytic activity of C-TiO₂+Ni powder (0.3 mg/ml) was also evaluated by photocatalytic treatment of *S. Typhimurium* bacteria suspension (15 ml, OD 0.0001, 22 °C, 7.4 pH, bacteria culture growth condition described at [10]) under UV and visible (Vis) light irradiation (2.5 h, UV – 30 mW/cm², Vis – 70 mW/cm²).

3. Results and Discussion

SEM images of the as-deposited C-TiO₂+Ni coatings (Fig. 1a) and corresponding washed-off powder particles (Fig. 1b) demonstrate that coatings well repeated the curvature of irregularly shaped K₂SO₄ grains. Accordingly, depending on the size of the particular support grains, the longitudinal size of the washed-off particles varied from few tenths up to few hundreds of micrometres. An average thickness of particle shells was 300-400 nm and well correlated with the total nominal thicknesses of Ni (150 nm) and C-TiO₂ (200 nm) layers (estimation based on corresponding deposition rates of Ni and C-TiO₂ on the flat substrates).

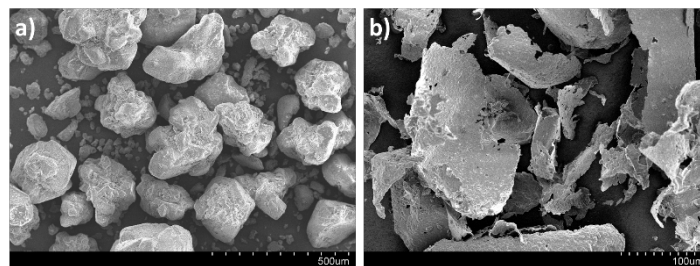


Fig. 1: SEM images of the as-deposited (a) and washed-off (b) bi-layered C-doped TiO₂ and Ni particles.

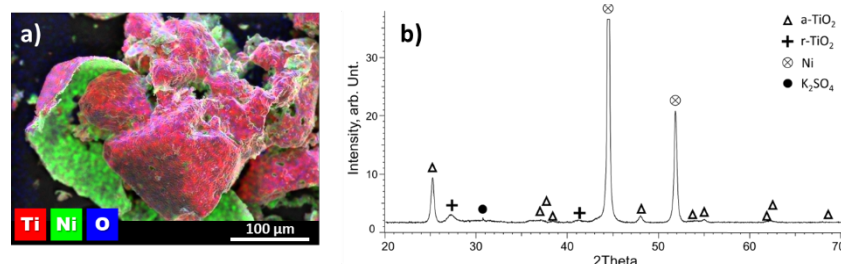


Fig. 2: EDS elemental mappings (a) and XRD pattern (b) of the washed-off C-TiO₂+Ni particles.

EDS elemental mapping of Ti, O and Ni (Fig. 2a) showed a clear composition difference between the two sides of the washed-off bi-layered shells. Similarly, XRD pattern of the powder (Fig. 2b) confirmed the presence of Ni and TiO₂ crystalline phases, and did not indicate any signs of nickel and titanium interdiffusion. To evaluate optical properties and band gap value of the synthesised powder C-TiO₂ photocatalyst, the same coatings were also deposited on flat borosilicate glass substrates. The obtained films were semi-transparent (20-40 %) over whole visible light spectrum and had dark brown-black shade (Fig. 3a). The measured band-gap value of C-TiO₂ (Fig. 3b) was lower than the corresponding value of conventional TiO₂ (≈ 3.2 eV) and followed the same trend as other carbon-doped TiO₂ films [11].

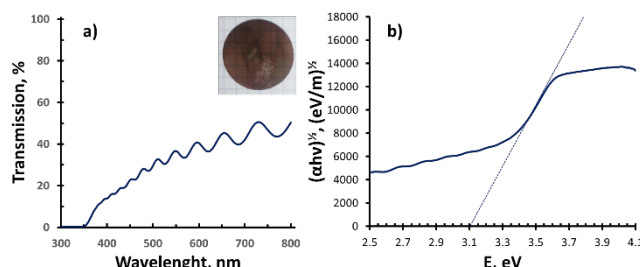


Fig. 3: Optical transmission (a) and Van't Hoff plot (b) of C-doped TiO₂ photocatalyst film.

In aqueous solutions magnetic photocatalyst particles readily reacted to the magnetic field. By optimising the size and strength of the magnetic stirring bar we were able to achieve the proper balance between the particle release when the stirring was turned on, and particle recollection on the magnetic stirring bar when the rotation was turned off. On average after each photocatalytic treatment cycle the ratio between the regained and initial powder mass was approximately 0.95, which is slightly better than the maximum regain of Bismuth Ferrites magnetic photocatalyst [12]. Fresh bi-layered C-TiO₂+Ni powder demonstrated significant photocatalytic activity and after 1 hour of UV and visible light supported treatment reduced *S. Typhimurium* bacteria viability by approximately 90 % and 45 %, respectively. For reference when the same treatment was repeated with P25 TiO₂ powder, bacteria viability reduction reached approximately 22 % and 3 % under UV and Vis light, respectively.

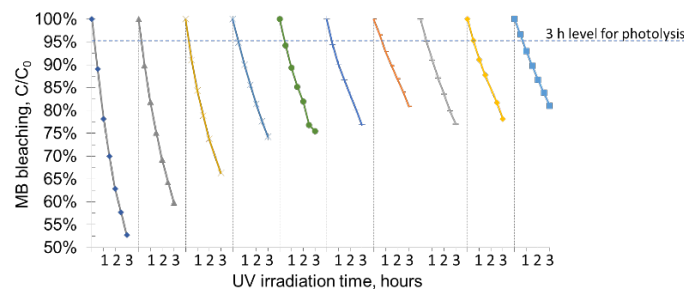


Fig. 4: C-TiO₂+Ni powder photocatalytic stability during repetitive bleaching of MB solution under UV light.

Magnetic photocatalyst powder stability tests provided mixed results (Fig. 4). After first 3h treatment cycle MB concentration was decreased by nearly 50 %. But by reapplying the same set of C-TiO₂+Ni powder for more cycles we observed that in just 4-5 consecutive cycles half of the initial photocatalytic treatment capacity was lost. Similar trend of activity reduction was reported at [13]. On the other hand, after the fifth cycle the rate of MB concentration reduction stabilised and remained at the same level for the next five cycles. Considering the observed stabilisation, we assume that the main cause of the performance deterioration is clogging of the smallest photocatalyst pores by reaction products.

4. Conclusion

Magnetron sputtering technique has been successfully applied for the synthesis of bi-layered C-TiO₂+Ni magnetic photocatalyst powder. Magnetised photocatalyst particles readily reacted to the external magnetic field and this feature allowed to regain approximately 95 % of used initial powder content after each photocatalytic treatment cycle. Fresh bi-layered carbon-doped TiO₂ and Ni powder have significant photocatalytic under both UV and visible light. However, during repetitive application half of the initial photocatalytic treatment capacity was lost in just 4-5 consecutive cycles. Active site clogging by reaction products was seen as the main cause of the performance deterioration.

Acknowledgements

This research is funded by the European Social Fund according to the activity ‘Improvement of researchers’ qualification by implementing world-class R&D projects’ of Measure No. 09.3.3-LMT-K-712, project “Investigation of the application of TiO₂ and ZnO for the visible light assisted photocatalytical disinfection of the biologically contaminated water” (09.3.3-LMT-K-712-01-0175). Authors are thankful for G. Laukaitis, K. Bockute, R. Uscila and M. Aikas for their valuable input in the conducted study.

References

1. J. J. Rueda-Marquez et al., “A critical review on application of photocatalysis for toxicity reduction of real wastewaters,” *J. Clean. Prod.*, vol. 258, 2020.
2. S. Higashimoto, “Titanium-Dioxide-Based Visible-Light-Sensitive Photocatalysis: Mechanistic Insight and Applications,” *Catalysts*, vol. 9, no. 2. 2019.
3. I. Dalponte Dallabona et al., “A new green floating photocatalyst with Brazilian bentonite into TiO₂/alginate beads for dye removal,” *Colloids Surfaces A Physicochem. Eng. Asp.*, vol. 627, p. 127159, 2021.
4. J. Song et al., “Visible-light-driven heterostructured g-C₃N₄/Bi-TiO₂ floating photocatalyst with enhanced charge carrier separation for photocatalytic inactivation of *Microcystis aeruginosa*,” *Front. Environ. Sci. Eng.*, vol. 15, no. 6, p. 129, 2021.
5. A. Y. Shan et al., “Immobilisation of titanium dioxide onto supporting materials in heterogeneous photocatalysis: A review,” *Appl. Catal. A Gen.*, vol. 389, no. 1, pp. 1–8, 2010.
6. S. Watson et al., “Synthesis of a novel magnetic photocatalyst by direct deposition of nanosized TiO₂ crystals onto a magnetic core,” *J. Photochem. Photobiol. A Chem.*, vol. 148, no. 1, pp. 303–313, 2002.

7. P. Singh et al., “Systematic review on applicability of magnetic iron oxides–integrated photocatalysts for degradation of organic pollutants in water,” *Mater. Today Chem.*, vol. 14, p. 100186, 2019.
8. S. Tučkutė et al., “A new method of nanocrystalline nickel powder formation by magnetron sputtering on the water-soluble substrates,” *Mater. Res. Express*, vol. 5, no. 1, 2018.
9. S. Varnagiris et al., “Black carbon-doped TiO₂ films: Synthesis, characterization and photocatalysis,” *J. Photochem. Photobiol. A Chem.*, vol. 382, 2019.
10. M. Urbonavicius et al., “Visible-Light-Driven Photocatalytic Inactivation of Bacteria, Bacteriophages, and Their Mixtures Using ZnO-Coated HDPE Beads as Floating Photocatalyst,” *Materials*, vol. 15, no. 4, 2022.
11. A. Piątkowska et al., “C-,N- and S-Doped TiO₂ Photocatalysts: A Review,” *Catalysts*, vol. 11, no. 1, 2021.
12. G.-Q. Tan et al., “Controllable Microwave Hydrothermal Synthesis of Bismuth Ferrites and Photocatalytic Characterization,” *J. Am. Ceram. Soc.*, vol. 95, no. 1, pp. 280–289, Jan. 2012.
13. R. A. da Silva et al., “Urea-assisted fabrication of Fe₃O₄@ZnO@Au composites for the catalytic photodegradation of Rhodamine-B,” *J. Sol-Gel Sci. Technol.*, vol. 86, no. 1, pp. 94–103, 2018.